Bologna University "Alma Mater Studiorum"

Physics department

PhD in Geophysics - XIX cycle

MULTITEMPORAL GEOMETRICAL ANALYSIS AND NUMERICAL SIMULATION OF LAVA FLOWS: THE CASE OF THE 2001 ETNA ERUPTION

FIS/06

PhD student:
Cristina Proietti

Tutors:
Prof. Maria Marsella

Dr. Mauro Coltelli

PhD Coordinator:
Prof. Michele Dragoni

PhD Supervisor:
Prof. Paolo Baldi

Introduction

Lava flows have rarely threatened or injured people, though they destroy everything lays along their path, farmed lands, forests or towns. It is therefore very important to study and model their emplacement. Computer simulation codes are becoming the more valuable tools for such a scope. As a matter of fact they can be adopted for better understanding the flow emplacement, for defining hazard maps of a volcano, as well as for forecasting the evolution of an ongoing eruption hazard maps are useful for map planning while the real-time simulation can be adopted for checking possible action aimed at risk mitigation.

The development of a reliable simulation code must be associated to a frequent updating of the topographic surface which is one of the factors influencing lava emplacement. Moreover frequent updates, which allows evaluating the emplaced lava volume and thus the effusion rate, must be carried out during an eruption.

The reliability of a simulation code must be verified, this is possible only by simulating an actual lava flow. This work is devoted to asses the reliability of two simulation codes aimed to real-time evaluation of lava flow emplacement. The main lava flow of the 2001 Etna eruption was selected as test case, and its 3D geometry as well as is temporal evolution were reconstructed from a topographic approach.

The work deals with three main topics: first it analyzes the existing simulation codes and the test cases they were applied, then it explain how the dataset was prepared, and finally it simulates the emplacement of the selected lava flow by means of two different codes, trying to define a methodology for assessing their reliability. Two chapters are also added to describe the emplacement of lava flows and to briefly present the historical lava flow of Mount Etna.

The literature simulation codes

A brief analysis of the literature simulation codes has been considered as the better starting point for the work, and as a source where finding suggestions and considerations.

Many simulation codes for lava flow emplacement have been developed starting from the 90's, they can be distinguished in two different categories: the probabilistic and the deterministic models.

Probabilistic models are based on the determination of the more probable path a lava flow will follow, taking into account only the volcano topography. Such models thus gives as output the maximum area to be invaded but not the flow geometry. For such a reason they are very useful for hazard map definition, also because they have very short computational time allowing a great number of simulation to be run. On the contrary they cannot be used for real-time application because they generally overestimated the covered area and they did not take into account the flow history, thus they are not able to reproduce an actual flow.

Deterministic models are based on the physic of the phenomenon, they can completely solve the equations or, as more generally happens, they apply more simple rules (i.e. a flow rate derived by the steady state solution of the Navier-Stokes equation or by the gaining of a hydrostatic equilibrium).

The second clue point derives from the analysis of the test cases utilized in the previous models. It is not possible to find examples accurately describing and simulating the temporal evolution of a lava flow emplacement. The reported analysis and comparisons were generally based on the final planimetry of the actual flow, sometimes derived by qualitative data. A quantitative analysis comparing the simulated and actual final areas was carried out by *Spataro et al.* [2004], which defined a fitness function to quantify this comparison.

The test case

The second clue point of the work was to select an ideal test case. Mount Etna was the ideal site to be utilized, as a matter of fact its frequent eruption allows to have an ample dataset where choose the best example. It gives a wide range of flow field shape, though all the eruptions can be grouped into two categories [*Hughes et al.*, 1990]:

- the type A, relatively long and narrow flow fields (simple);
- the type B, which are wide by comparison with their lengths (compound).

Type A flow fields are generally related to eruptions that had higher effusion rates, and shorter durations than those that produces type B flows.

A simple flow, that is the main flow of the 2001 Etna eruption, was selected as first test case, considering its shape and its emplacement evolution. As a matter of fact it is a single flow, and it was characterized by lengthening between 18 and 26 July and then, after a net decreasing of the effusion rate, it presented a regression of the active flow front that did not gave way to secondary flows, with the exception of a minor branch, fed by ephemeral vents during the last days of the eruption.

The simplicity of this flow makes it an ideal flow to be simulated, moreover many data were available. The composition of the 2001 lava was measured by *Taddeucci et al.*, [2004] moreover it was possible to define the pre- and post-eruption topographies, from which an accurate estimate of the flow volume was derived. Finally it was possible to reconstruct the flow evolution from a planimetric maps and an analysis of the flow thickness. The cumulated volumes and then the daily effusion rates were also derived from such analysis.

This work describes also the procedures applied to improve the matching between the pre- and post- eruption topography, as well as to evaluate the volume accuracy.

Simulation of the main 2001 Etna lava flow

Two codes were adopted for simulating the emplacement of the main 2001 Etna lava flow: the LavaSIM code [*Hidaka et al.*, 2005], developed by the National Research Institute for Earth Science and Disaster Prevention (Tsukuba-Japan), and the MAGFLOW code [*Vicari et al.*, 2006], developed by the TECNOLAB laboratory of Istituto Nazionale di Geofisica e Vulcanologia – Catania.

Both the codes are deterministic. LavaSIM is a three-dimensional computational fluid dynamics code based on the solution of the Navier-Stokes and the energy equations, thus it solves quite completely the physics of the phenomenon. MAGFLOW is a two-dimensional code based on the Cellular Automata approach which uses, as transition function, the flow rate evaluated from the steady state solution of the Navier-Stokes equation. MAGFLOW is more simple and rapid than LavasIM thus it is particular useful for real-time applications, whereas LavaSIM can give more insights into the lava flow emplacement.

The reliabilities of both the codes were evaluated by comparing the temporal evolution of the planimetry of simulated and actual flows. This comparison was carried

out by defining two variables: the percent length ratio, comparing simulated and actual lengths, and the fitness function, already utilized by *Barca et al.* [2004], for comparison between simulated and actual areas. By simultaneously considering these two variables it is possible to check both lava lengthening and spreading, since the fitness function alone resulted not sufficient. MAGFLOW allowed also to compare the final thickness distributions of actual and simulated flows.

1. The eruptive history of Mount Etna

Mt. Etna (Figure 1.1), located in the eastern part of the Sicily island (Italy) is the largest active volcano in Europe. Its frequent eruptions make it an ideal site for studies on the volcanological processes.

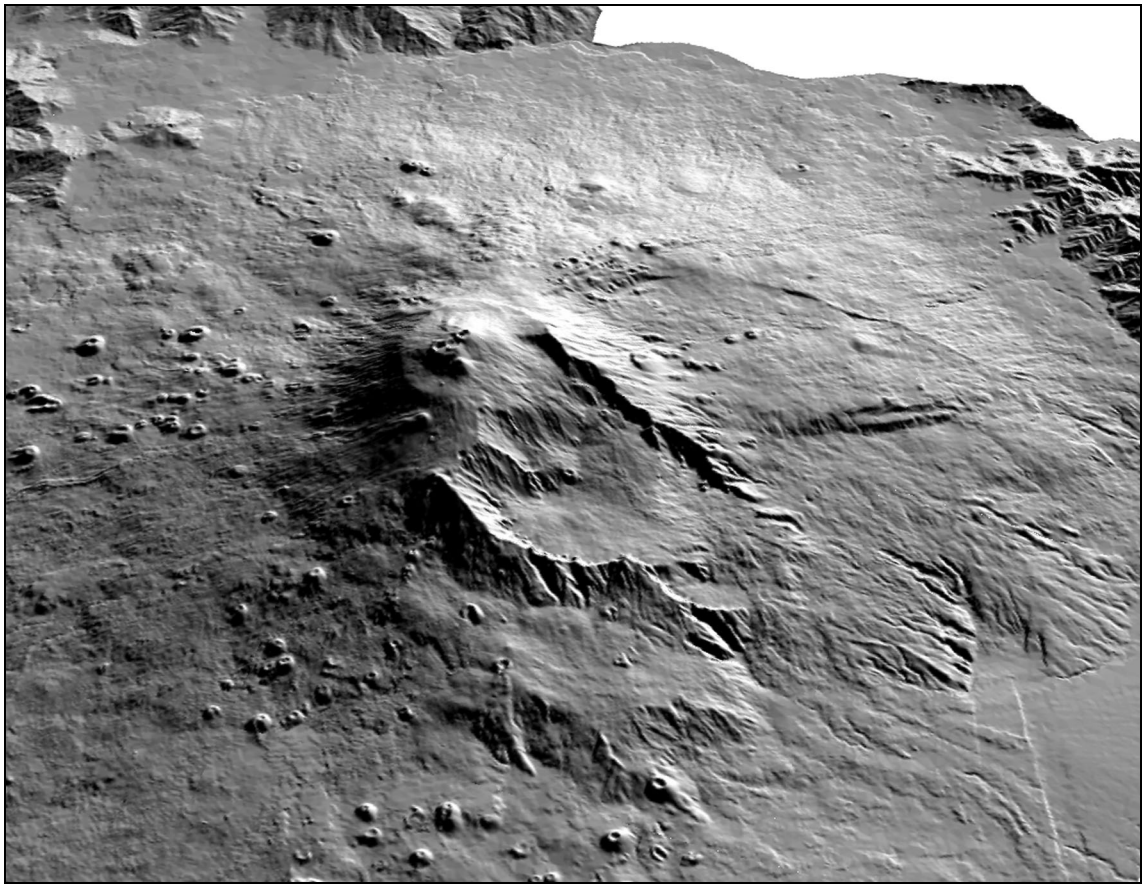

Figure 1.1: 3D view of the summit of Mount Etna

Documents on the Etna activity dates back to Greek and Roman civilizations while its history was summarized starting from the seventeenth and eighteenth centuries, though the records of flank eruptions can be considered complete and reliable only after the mid 17-th century. The 1669 lava flow eruption (Figure 1.2), which destroyed the town of Nicolosi as well as many other villages and covered the western part of Catania, changed the way of observing and describing the eruptive events toward a more modern conception, greatly improving the quality and completeness of information [*Branca and Del Carlo*, 2004].

The Etna summit craters (Figure 1.3) show a quasi-continuous activity, characterized by Strombolian eruptions and periodic lava fountaining episodes, often associated with lava flows [*Guest*, 1982; *Calvari et al.*, 2002; *Branca and Del Carlo*, 2005]. Etna is also interested by quite frequent flank events, from fissures which opened during an eruption, and then they are no more actives. Flank eruptions generally produce lava effusion associated with weak explosive activity.

Figure 1.2: Artist's depiction of the voluminous 1669 eruption showing the lava flow from Monti Rossi entering the city of Catania and reaching the sea, Anonymous, ca. 1687, after [*Boschi and Guidoboni*, 2001].

Branca and Del Carlo [2005] compiled a catalogue summarizing the date, duration, vent location, eruption type and description of the activity for all known Etna's eruptions since 1670. They considered both central activity and flank eruptions, and classified flank eruptions on the basis of the eruptive styles as:

- Class A: almost purely effusive, forming simple or compound lava flows; weak strombolian activity is often associated to the beginning of the eruption;
- Class B: effusive activity associated with long-lasting, ash plume-forming explosive (strombolian and lava fountaining) activity.

They observed that the frequency of volcanic events after the 1669 eruption was relatively low for about 60 years. Then, from the end of 1727 an increased eruptive activity was observed at the Central Crater, while the flank eruptions augmented from the 1763. Starting from 1880 the Central Crater showed a higher frequency of explosive activity (stombolian, lava fountaining and subplinian). Finally, from 1961 a significant increase of explosive activity at summit craters was also accompanied by a sharp increase in the number of the flank eruptions.

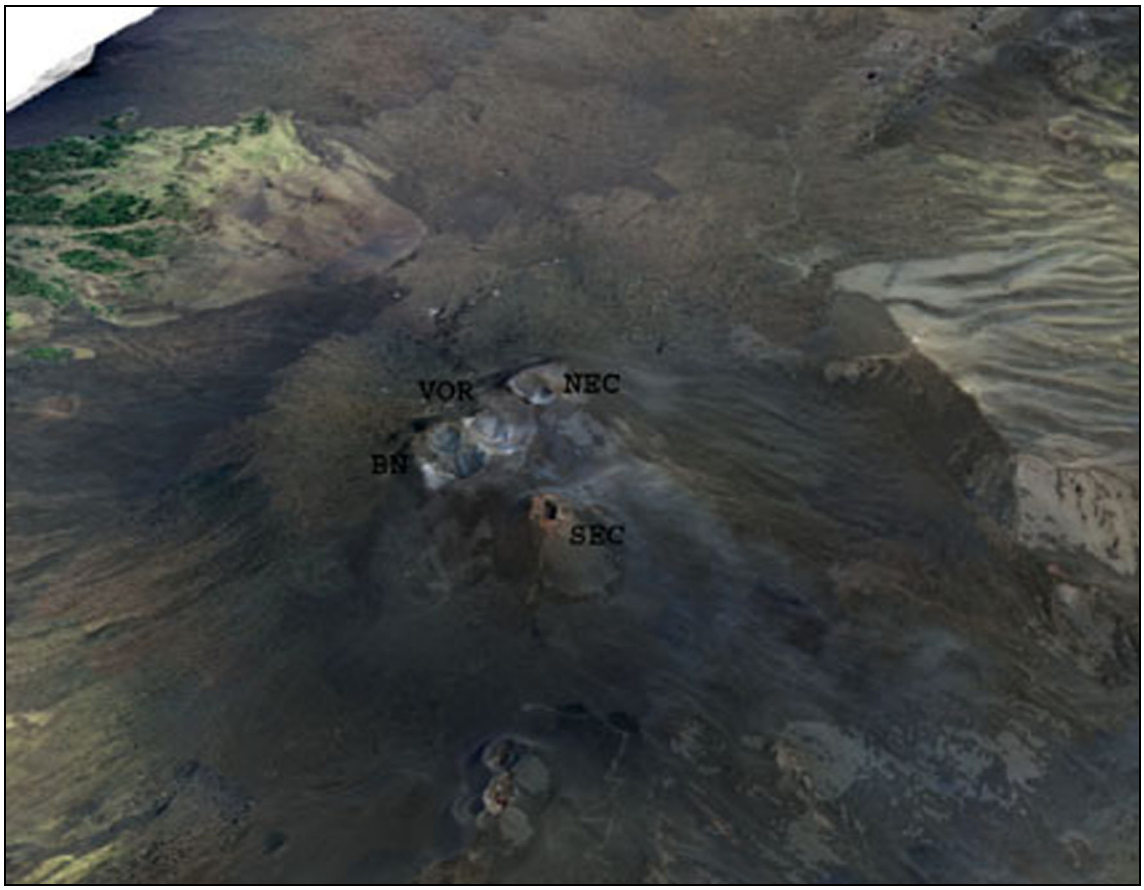

Figure 1.3: view of the Etna summit craters: Voragine (VOR), Bocca Nuova (BN), South East Crater (SEC) and North East Crater (NEC).

1.1 Analysis of Etna's historical (1670-2003) eruptive activity

In the interval between 1670 and 1726, central activity was infrequent, consisting only of lava emission in 1688 and some months of intense lava fountaining activity in 1694 at the summit. At that time, the summit consisted of a single crater named the Central Crater (CC). Concerning the flank eruptions, three Class A eruptions, not preceded by any central explosive activity, were recognized.

From 1727 to 1879, central activity was generally characterized by phases of strombolian activity and lava emissions at CC, lasting from a few months to three years, and separated by long periods of rest. In several cases, lava flows occurred contemporaneously with the strombolian activity, forming lava-flow fields in the summit areas. Three subplinian eruptions also occurred in the period, apparently within phases of strombolian activity. Only in some cases explosive activity at CC was followed by flank eruptions (e.g., 1792–1793 eruption). Fourteen Class A and three Class B (1763 La Montagnola, 1811 Mt Simone and 1852–1853 Mt Centenari) flank eruptions were recognized.

From 1880 until 1960, strombolian activity at CC became more frequent and lasted longer than previously, generally separated by a few year intervals of inactivity. Some important structural and morphologic changes occurred at the summit in the 20th century. In particular, the North East Crater (NEC) formed in 1911 as a pit on the north-eastern flank of the summit cone. Some short-lived lava effusions and associated strombolian activity (maximum 5 months long) occurred in 1918, 1923, 1955, 1956, and 1957. Lava fountain episodes showed a similar behavior as in the previous period; some occurred randomly, others before or at the onset of flank eruptions and generally were associated with periods of intense eruptive activity at the summit craters. Three subplinian eruptions occurred in the period. Twelve Class A and two Class B (1886 Mt Gemmellaro and 1892 Mts Silvestri) flank eruptions were recognized.

From 1961 to 2003, a rise in the frequency in the entire spectrum of central activity was observed, from weak intracrater strombolian to the subplinian episodes, as well as flank eruptions. During this period, the longest repose interval was between April 1993 and July 1995. Significant morphological changes took place in the summit area in this time interval. In June 1968, a pit crater, named Bocca Nuova (BN), formed on the west side of the CC. From this date on, the previous main vent (CC) began to be known as Voragine (VOR). Finally, in 1971 a new pit crater opened to the southeast of BN. Starting from 1978 this new crater, named South East Crater (SEC), became active. Concerning the highest-magnitude central events, six subplinian eruptions took place. As regards to the flank eruptions eighteen Class A and two Class B eruptions (2001 and 2002–2003) were recognized [*Branca and Del Carlo*, 2005].

1.2 Flank eruptions

Fifty-four flank eruptions were recorded by *Branca and Del Carlo* [2005] during the period from 1670 to 2003, 87% of which were classified as Class A and only 13% as Class B. The duration of the flank eruptions ranged from a few hours (13 h in 1942) to more than a year (473 days in 1991–1993).

The eruptive fissures of Class A eruptions are nearly equally distributed on the North, South and East flanks, whereas only four eruptions have affected the West flank. The majority of Class A eruptions vents are the NE, ENE and S Rift zones, which radiate from the summit. Another region containing a high-density of vents is the W Rift zone, which has been less active during the past three centuries, producing only four eruptions. The vents are mainly distributed between 1600 and 2800 m elevation, with a peak between 1600 and 1700 m. Only three eruptive events were produced by vents that opened below 1600 m elevation down to 1100 and 1300 m elevation (1809, 1928: the eruption that destroyed Mascali village, and 1981). The Class A eruptions are believed to represent the outpouring of magma that has lost volatiles throughout a multi-stage decompression during ascent within the plumbing system before reaching the surface [*Branca and Del Carlo*, 2005].

The eruptive fissures of Class B eruptions are restricted to the South and Eastern flanks. This kind of flank eruption, characterized by ash-plume-forming explosive activity, as during the 2001 and 2002–2003 events, is infrequent. In fact, in the 18th century, only one occurred in 1763 on the upper South flank. The high explosivity of Class B eruptions implies a much higher volatile content in the magma rising, with minimal pre-eruptive degassing, from the deeper part of the plumbing system. In some cases, the magma intrusion and ascent can derive directly from the deep portion of the feeding system, as occurred in 1763, 2001 and 2002–2003 [*Branca and Del Carlo*, 2005]. Two Class A eruptions were also produced in 2004-2005 and in 2006 on Valle del Bove.

Only flank eruptions may threat inhabited areas, being located far from the summit areas. Moreover the length of flows increases the lower the vent altitude, a decrease in altitude means a lesser degree of slope and therefore the flows tend to widen out rather than lengthen [*Romano and Sturiale*, 1982].

Between 1670 and 2006 Etna threatened inhabited areas four times: in 1928, when the lava, emitted from vents at 1200 m a.s.l., reached the village of Mascali; in 1971, when a lava narrowly missed the village of Fornazzo; in 1981, when a lava flow reached the outskirts of the village of Randazzo; and in 1991–1993, when a voluminous lava flow menaced the village of Zafferana [*Barberi et al.*, 1993]. Moreover it should be mentioned the 1669, 1983, 2001 and 2002-2003 eruptions. The 1669 lava field, whose lowest vent opened at 900m a.s.l. on the southern flank, caused extensive damage to the city of Catania and reached the sea. Finally the 1983 eruption was threatening the towns of Nicolosi and Belpasso, destroying forests and patches of agricultural land and burying numerous isolated buildings, whereas the 2001 and 2002-2003 eruption did not approach inhabited areas, though they threatened or damaged tourist facilities.

1.3 Human operations to limits damages from lava flows

Human operations were carried out during the 1983, 1991-1993, 2001 and 2002-2003 eruptions for limiting or avoiding damages from lava flows. Such operations, for slowing or deviating the flow advancing comprised building of earthen barriers, creation of artificial channel and blasting out of the flow margins for lava diversion, and obstruction of the main channel.

The first operation to control lava flows was carried out on Etna during the 1669 eruption, when the citizens built up earthen walls to protect Catania. These were 18 m high and initially contained and deviated the lava, but were finally overflowed (not destroyed) and a large part of the city was destroyed [*Barberi and Carapezza*, 2004].

The 1983 eruption, emplaced on the South flank between 28 March and 6 August, was fed from a 750 m long fissure, extending from 3000 m down to 2250 m a.s.l., though the main effusion occurred from boccas between 2320 and 2265 m a.s.l. The low effusion rate resulted in the emplacement of a compound lava flow field of bifurcating and overlapping flows. The total effused volume was about 80-100 X 10^6 m^3, giving on 131 days an average effusion rate of 7-9 m^3/s, while the maximum flow length was approximately 7.5 km [*Guest et al.*, 1987].

The operations (Figure 1.4) on the 1983 lava flow was aimed to deviate the flow path in an artificial channel, excavated parallel to the natural one. Earthen barrier were also built to guide the path of the diverted lava by impeding lateral expansion in built-up or

farmed areas. Explosive were utilized to create an opening in the solid levee of the lava channel in correspondence with the artificial channel. A number of difficulties prevented placing charges in the deepest part of the lava channel, thus a modest diversion was created and it lasted only a couple of days. As a matter of fact the little slope of the artificial and the exposition of fresh lava to the atmosphere facilitated lava cooling and the consequent obstruction of the artificial channel. However, the dumping of a large amount of big solid fragments produced by the explosion into the lava channel plugged a tunnel located just downhill from the point of operation was plugged, thus forcing nearly all the lava to overflow out of the tunnel [*Barberi et al.*, 1993].

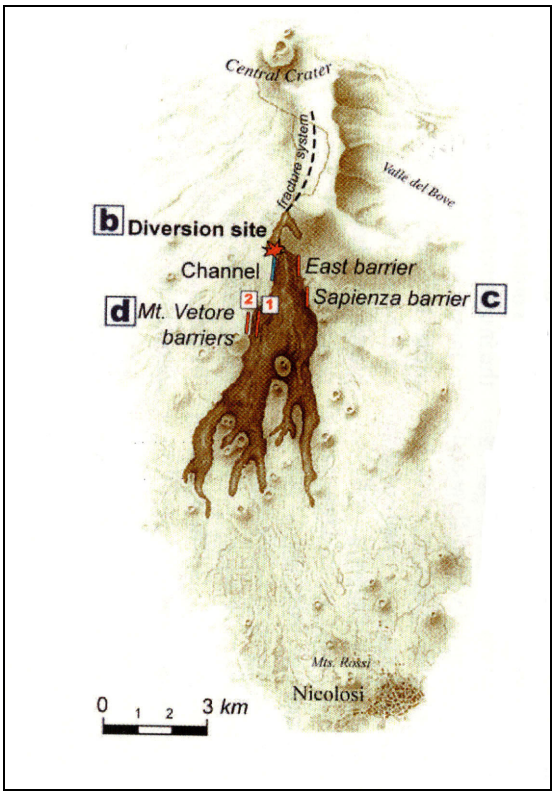

Figure 1.4: operations on the 1983 Etna eruption [after *Barberi and Carapezza*, 2004].

The 1991-1993 eruption formed a 7.6 km^2 lava flow field on Valle del Bove, and a volume of 235 X 10^6 m^3 was emplaced on 473 days (from 4 December 1991 until 31 March 1993), giving an eruption rate of about 5.8 m^3/s [*Calvari et al.*, 1994]. The lava flow was rapidly approaching Zafferana, 8 km far from the vent, and by mid April 1992 the front was 800 m town [*Barberi et al.*, 1993].

A computer simulation based on the identification of the steepest path was run, showing that Zafferana was on the probable flow path [*Dobran and Macedonio*, 1992].

The 1992 operations (Figure 1.5) for protecting Zafferana, included the building of four lava-containment earth barriers, several attempts at plugging a tunnel by concrete blocks, steel hedgehogs and large fragments of solid lava obtained by blasting the channel levee, and finally, the total diversion of the lava flow from a skylight near the vent into an artificial channel, by blasting the separation wall between the two channels and obstructing lava tunnel by dumping into it big boulders by mechanical means. The earth barriers, oriented orthogonally to the direction of the lava flow, slowed the front propagation though they were not able to stop it, overflows over passed the furthest front, also a few days before the flow diversion near the vent. The retreated of the active fronts and the closing of the ephemeral vents took place only a few days after the diversion [*Barberi et al.*, 1993].

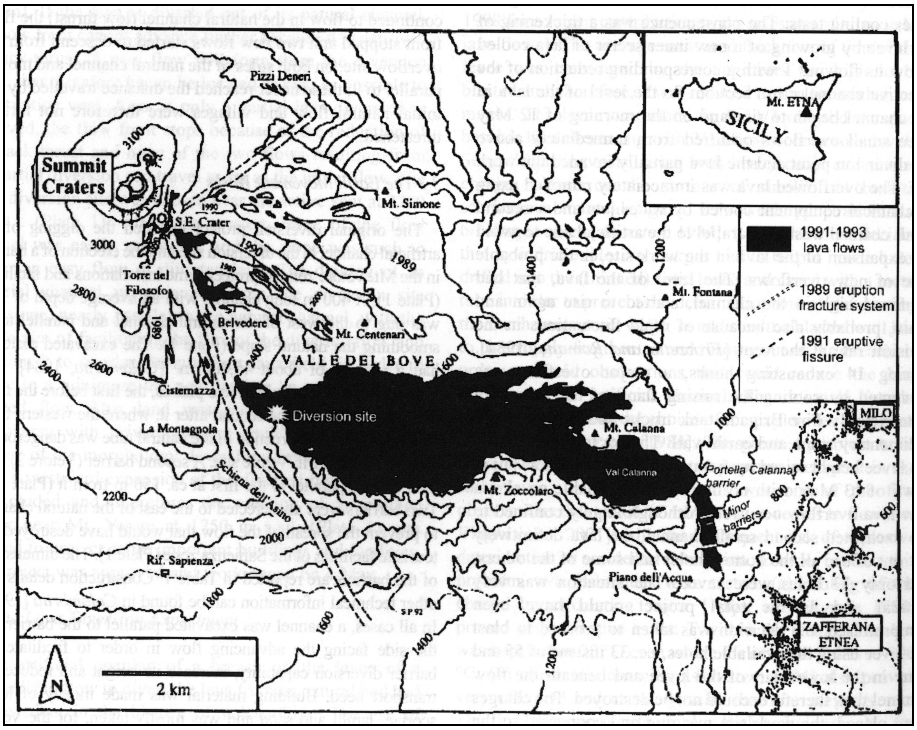

Figure 1.5: operations on the 1991-93 Etna eruption [after *Barberi and Carapezza*, 2004].

The 2001 eruption involved the South flank, where it generated seven lava flows (for a more complete description see chapter 4). The lava flows emitted from the 2700, 2550 m and 2100 a.s.l. vents (named UFS2, LFS2 and LFS1, respectively in figure 4.2) were threatening the tourist facilities of Rifugio Sapienza (see figure 4.2 for location) and of Mts. Silvestri (threatened only by the LFS1 flow). Thirteen earth barriers (Figure 1.6) were built to protect the Rifugio Sapienza and Mts. Silvestri facilities. Four barriers

were constructed laterally to UFS1 flow to slow or prevent its expansion of the on the tourist area and three were successively buried by the lava from the LFS2 flow. The remaining nine were built uphill of the Sapienza zone to prevent destruction by the lava descending, firstly (since 20 July), by the UFS2 vent and, then (since 25 July), from the LFS2 vent. The barriers worked well, initially delaying the advance of the flow and then diverting it toward SE, away from the facilities to be protected. Because of it low effusion rate, the UFS2 flow did not reach the Sapienza area. The five initial barriers were almost totally buried by lava flow from the LFS2 flow. Then four barriers were erected to divert the new flow far from the Sapienza area, though the lava flow was still approaching it. The decreasing of the effusion rate prevented the Rifugio Sapienza to be destroyed. Finally, water jets were used to cool the lateral margin of the lava flow. [*Barberi and Carapezza*, 2004].

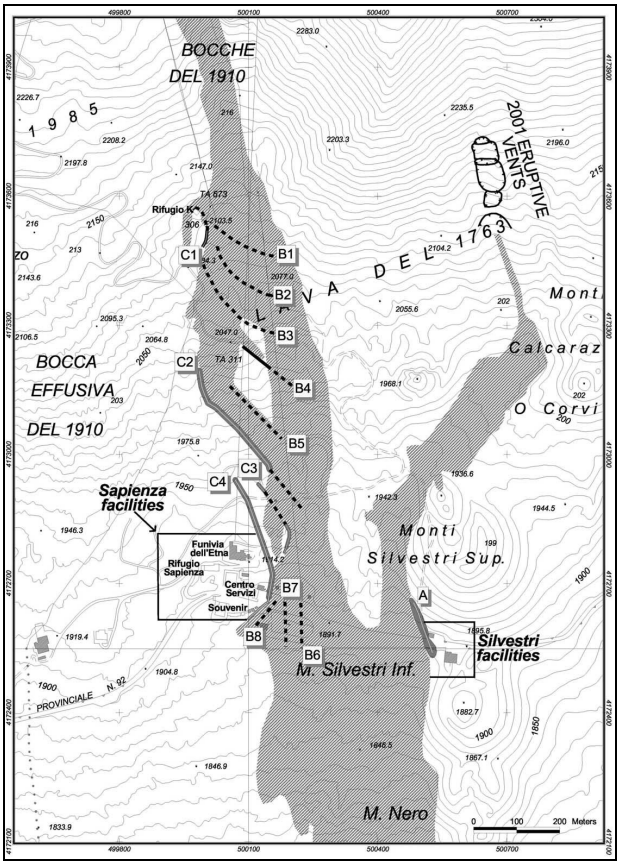

Figure 1.6: earth barriers built on the 2001 Etna lava flows to protect Rifugio Sapienza tourist facilities [after *Barberi et al.*, 2003].

A simulation of the eruptive scenario [*Barca et al.*, 2004] showed that the towns of Nicolosi and, subordinately, Belpasso could have been reached by the lava emitted from

the UFS1 vent. An operation plan was established which included: (i) the building of lateral earthen barriers, to drive the flow toward existing large depressions, and orthogonal barriers, to increase the retaining capacity of the depressions; (ii) the diversion of the flow from its natural channel, as in 1992; and (iii) the evacuation of the villages. Because of the decrease in the effusion rate recorded since the last days of July, the plan did not need to be put into operation [*Barberi and Carapezza*, 2004].

The 2002-2003 eruption produced two distinct lava flows, one on the North-Eastern flank (between 27 October and 7 November 2002) which destroyed the tourist facilities of Piano Provenzana and one on the South flank (between 28 October 2002 and 28 January 2003) which threatened again the Rifugio Sapienza area.

The described eruptions demonstrated that human operations can be useful to reduce damages from a lava flow, nevertheless they must be carefully planned. Simulations of the path the lava will follow after the operations can be very valuable for predicting the related rewards and disadvantages: the deviated flow could cause greater damages that the natural one. The construction of earth barriers or the creation of an artificial channel can be easily modeled by modifying the pre-eruption topography to be used as input parameter of the simulation. However the reliability of a simulation code, to be used for such hazard management, must be verified by simulating actual lava flows, as will be shown in this work.

2. The lava flow emplacement

Lava has the tendency to enclose itself within a carapace cooler and stronger than its interior, thus a lava flow can be treated as continuously deforming cores beneath colder layers which fail by rupture.

The emplacement of lava flows on a volcano is controlled by many factors, including the effusion rate (i.e. the lava discharge rate from a single vent), the slope of the ground, the preexisting topography, the viscosity and yield strength of the lava and surface solidification [*Walker*, 1973; *Hulme*, 1974]. Using field observation, it is difficult to determine the individual effects of these various factors, because they typically change as a function of position and time throughout an eruption.

A lava flow is generally characterized by an early channel formation and downstream flow thickening. Even when a flow is unconfined topographically, widening rapidly slows along its upper and middle reaches. Static lateral margins, or levees, develop and confines motion to a central channel which may later roof-over as a tube. As a result, flows soon develop two distinct zones [*Kilburn and Lopes*, 1991; *Kilburn and Guest*, 1993]: a feeder zone (channel or tube), the fixed margin of which are older than the lava flowing between them, and a frontal zone, lacking clear marginal structures, were most flow widening becomes concentrated. In particular its snout spread outward and forward as a poorly structured sheet [*Kilburn*, 1996]. Fronts tend to slow, widen and thicken during emplacement, while channels become narrower because of inward levees growth. Lava accumulates within the channel and may led to overflows, intrusion or breaching of the flow margins by channel lava.

The distal part of a lava flow can be divided into two intergradational zones (Figure 2.1): the rear frontal zone (RFZ) and the snout frontal zone (SFZ) [*Kilburn and Lopes*, 1991]. Lava entering the snout spreads out radially, inhibiting the formation of a channel structure and is deposited at the sides and front of the flow, fixing its initial width and extending its basal layer. Further upstream, the RFZ grades into the channel (CZ). The cannel zone is where most of a flow's longitudinal deceleration is inferred to occur; combined with an increase in rheological resistance away from the vent, such deceleration results in a downstream increase of the flow depth.

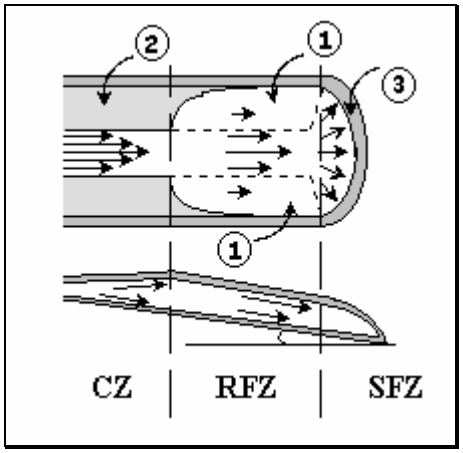

Figure 2.1: frontal zones of a lava flow. CZ: channel zone, RFZ: rear frontal zone, SFZ snout frontal zone. The arrows show qualitative velocity profile. Circled numbers represent: (1) incipient levees, (2) mature levees, (3) lava crust [after *Kilburn and Lopes*, 1991].

Soon after effusion begins, lava advance is concentrated along a few preferred directions, influenced by local slope and topography. Along each flow, solidification slows the rate of spreading and advance. Lava arrives at the front more quickly than the front can carry material downslope, thus the flow thickens and, if accumulation is too rapid, the flow margins can be disrupted and core lava escapes to feed a new flow. The flow field locally lengthens, widens or thickens depending on whether the lava emerges from the distal margins, lateral flanks or the top surface of the existing flow [*Kilburn and Lopes*, 1991]. New flows may also form as an existing stream bifurcates about topographic highs, cooling and topography thus encourage flow field to evolve as a collection of tributary streams.

Long lasting eruptions generally evolves from an early lengthening (of the initial main flow) to widening (by the lateral propagation of new flows) and, finally, to thickening (by flow superposition or by the uplift of the flow surface as lava accumulates beneath). On the contrary short eruptions generally form a single flow, characterized by an early stage of relatively rapid lengthening, lasting until the supply rate to the front is able to overcome frontal resistance, this first stage is then followed by an intermediate phase of deceleration and finally by a much slower advance. Supply to the front may end because the eruption finishes or because local changes along a flow divert lava in new directions. Once supply has been cut, flow advance may continue at a decreasing rate as channel lava drains into the front. Such lava flows are defined as

volume-limited [*Guest et al.*, 1987]. Otherwise a flow may continue to be fed even though its front has come to a halt. Lava accumulates in the channel, causing its thickening, and eventually may results in overflows, intrusions or breaching of the flow margins. Such flows are defined as *cooling-limited* [*Guest et al.*, 1987]. The main flow of the 2001 Etna eruption, whose evolution will be further described (chapter 4), is an example of cooling-limited lava flow.

2.1 Surface effects

The emplacement of a lava flow results from the combination of different effects related to the flowing of a cooling fluid, thought it is mostly controlled by frontal advancement.

Surface effects add to the rheology in controlling flow morphology and dynamics: the Binghamian behavior implies that lava can have a not smooth surface [*Dragoni*, 1993]. Moreover the development of a solid crust, as soon as lava leaves the vent, gives to the lava surface a tensile strength important in the evolution of a lava flow. The tensile strength of chilled lava cannot be responsible for the formation of flow levees [*Hulme*, 1974]. However in mature flow the cooling produces marked rheological gradients in the flow margins, the tensile strength of which may become sufficient to stop the flow front [*Wadge*, 1978]. Finally the lava flow can cause the erosion by melting of the substrate. As lava advances, it loses heat to the ground developing a basal thermal boundary layer. Since the ground material is commonly made by solidified lava, it has a solidus temperature lower than the temperature of flowing lava. If a flow remains active for a long enough period, it may be able to melts is own bed, thus the flow thickness will result greater than that of the flow margins [*Dragoni*, 1993].

2.2 Lava as a Bingham fluid

Lava flows construct their own levees and may come to rest on a steep slope. For such a reason lava can not be described as a Newtonian fluid but its rheology is approximately that of a Bingham liquid, whose shear strain is zero until a yield value σ_y is reached, then, above σ_y, it is a linear function of the stress. A consequence of the yield stress is that, when a Bingham liquid flows in a channel subject to a pressure gradient, the zone of shearing is limited to the periphery of the channel, while the central zone (the plug) moves as a rigid body at uniform velocity. Regions with shear stress lower than the

yield value can also exist in contact with the ground, such regions where the lava will not move are located along the sides of a flow, leading to the formation of stationary levees.

The typical behavior of a lava flow can be grossly reproduced by two dimensional models of Bingham fluids flowing down a constant slope, which are simplifications of the actual flow conditions. They consider steady, laminar flows, so that transient phenomena, caused by rapid changes in model parameters, cannot be described. These models only represent the flow well behind the front, where levees can be taken as fixed, since they are cooler and have a higher yield stress than fresh lava flowing between them. Processes at the front, including levee formation, the change in shape of the flow and the choice of the flow path, are not taken into account. The results of analytical models can serve as a guide for more elaborate, numerical flow models [*Dragoni*, 1993].

Dragoni et al. [1986] modeled the flow of an isothermal, incompressible Bingham liquid, having a fixed thickness H along an inclined plane, solving the Navier-Stokes equation in the steady-state laminar-flow case. They considered two models, one representing low aspect ratio flows (aspect ratio is the ratio of flow height to flow width) and the second representing flow on a cylindrical channel with semi-circular cross-section. The equation they obtained for the flow rate q in the low aspect ratio case is:

$$q = \frac{\rho \sigma_y H_c^2}{3\eta}\left[(\frac{H}{H_c})^3 - \frac{3}{2}(\frac{H}{H_c})^2 + \frac{1}{2}\right] \qquad (2.1)$$

were ρ and η are the lava density and viscosity whereas H and H_c are the flow and plug thicknesses. This solution was then utilized as transition function of simulation codes based on the cellular automata approach [*Ishihara et al.*, 1989; *Miyamoto and Sasaki*, 1997; *Vicari et al.*, 2006]. The author also evaluated the flow thickness, for a fixed flow rate, at low values of the yield stress, when the flow is essentially in the Newtonian regime. Flow height and velocity were studied in the channel zone as function of the model parameters (yield stress, flow rate density, ground slope and temperature). Binghamian lava resulted to have much greater flow heights and much lower velocity than those Newtonian lava with same characteristics would have. Moreover flow rate change resulted to have no influence on flow heights but only on flow velocity. Finally the simultaneous strong temperature-dependence of viscosity and yield strength resulted

to produce marked effects on flow height and velocity, following even a slight temperature change; along a downslope flow, flow height increases very rapidly in the Bingham regime, while flow velocity drops to very low values.

Dragoni [1993] considered the steady flow of an incompressible Bingham liquid in three cases: the isothermal; non-isothermal with constant temperature in any given flow section and temperature decrease in the downstream direction; non-isothermal with temperature variations along the flow and with dept. He started from the equation of motion for an incompressible Newtonian fluid:

$$\rho\left(\frac{\partial v_i}{\partial t}+v_j\frac{\partial v_j}{\partial x_j}\right)=-\frac{\partial p}{\partial x_i}+\frac{\partial}{\partial x_j}\left[\eta\left(\frac{\partial v_i}{\partial x_j}+\frac{\partial v_j}{\partial x_i}\right)\right]+\rho g_i \tag{2.2}$$

were ρ is the density, ν is the viscosity, v_i is the velocity, p is the pressure and g_i is the acceleration due to gravity (summation over repeated indices i and j is assumed). Boundary conditions are $v_x = 0$ at $z = 0$ and vanishing shear traction and $p = p_0$ (with p_0 atmospheric pressure) at the free surface of the flow ($z = h$). The same equation can be applied to a Bingham fluid, by imposing the extra-condition that there is no shear deformation if $\sigma < \sigma_y$ (σ_y yield strength), to derive the velocity in the downflow direction (x):

$$v_x=\begin{cases}(1/2\eta)\rho g(\sin\alpha)z(2h-z)-2\sigma_y z & 0 \le z \le h - h_p \\ (1/2\eta)\rho g(\sin\alpha)h^2\left[1-\left(\sigma_y/\sigma_b\right)\right]^2 & h - h_p \le z \le h\end{cases} \tag{2.3}$$

were $\sigma_b = \rho g h \sin\alpha$ and $h_p = \sigma_y /(\rho g \sin\alpha)$ is the plug thickness (α ground slope).

When dealing with downflow temperature variations, *Dragoni* [1993] introduced also the heat equation:

$$c_p q\frac{dT}{dx}+E\Sigma T^4=0 \tag{2.4}$$

were c_p is the specific heat, q is the mass flow per unit width, E is the surface emissivity and Σ is the Stefan constant. He then derived the steady-state solution of the motion equation by assuming a downslope variation in flow parameters. Viscosity and yield strength resulted to increase by orders of magnitude along the flow. The model also showed that higher effusion rates lead to slower cooling, which resulted in slower increase of viscosity and yield strength, thus producing greater flow lengths. The flow

also presented a remarkable increase in flow thickening at some distance from the vent, corresponding to a strong deceleration in the lava motion and indicating that the flow has entered in the Bingham regime, whereas at higher temperature it still was in the Newtonian regime.

2.3 Front behavior

The advance of a lava flow is mainly governed by its frontal zone. The front propagation can not be considered as two-dimensional because it is not delimited by lateral fixed margins, but it is an unconfined area were most of the flow spreading happens.

A flow section can be distinguished, according to deformation criteria in crust that is the flow units which deforms by failure, and an underlying core which deforms by continuous flow [*Kilburn*, 1996]. Two distinct regimes of flow emplacement can be defined: *core-dominated* and *crustal-dominated* [*Kilburn*, 1993]. *Core-dominated* emplacement occurs when the rate of mechanical energy supply is fast enough for widespread surface autobrecciation, giving a persistent crustal failure. Open channels form on slope and fronts advance as single units at rates limited by core resistance. *Crustal-dominated* emplacement occurs at lower rates of mechanical energy supply, giving way to less widespread surface disruption. Tube systems may develop and the fronts advance by local puncturing of the crust, their mean velocity being limited by the rate of crust disruption. All lavas tend, throughout their emplacement, from early core-dominated regimes to later crustal-dominated.

Front advance can be considered as a balancing between the pull from the core and the restraining pull exerted by the crust on the core. A flow front attempts to minimize its rates of mechanical energy dissipation under the imposed condition of emplacement. In the front, momentum is transferred from core to crust as the core loses mass in being transformed into crust, and the core is slowed while pulling the crust forward. By adopting a constant bulk density, mass conservation in the front can be described trough conservation of the frontal volume. Momentum conservation requires that the bulk forces on the front satisfy the condition [*Kilburn*, 1996]:

(force due to momentum being carried into the front by newly arriving lava) +

+ (net surface and body forces acting on front) =

= (bulk rate of change of frontal momentum)

The first and third terms of the previous equation are equivalent, then the front motion is promoted by a balancing of the surface and body forces acting on the front. This implies that the difference between the driving forces, due to the weight of the lava and to the pressure induced by the slope of the frontal surface, and the resisting forces, due to the core rheology and to restrain from the crust, must be zero. The net force balance through the front can be written as:

$$F_{Dco} = F_{Rco} + F' \tag{2.5}$$

$$F_{Dcr} = F_{Rcr} - F' \tag{2.6}$$

were F_D and F_R denote the average driving and resisting forces, F' is the rate of momentum transferred into the crust from the core, while *co* and *cr* refer to core and crust, respectively.

Persistent disruption of new crust (core regime) is assured if the imposed deforming forces increase as quickly as the cooling-induced tensile resistance of the crust, thus downstream crustal stretching is assumed to control the rate of autobrecciation. The driving forces are the weight of connected crust (F_w) formed by cooling in Δt, a pull from the core (F_{pl}) and bending forces around the snout (i.e. the furthest zone of the flow front), whereas crustal resistance is the restraining force [*Kilburn*, 1996]. Equation 2.6 thus gives:

$$\frac{dF'}{dt} = \frac{dF_w}{dt} + \frac{dF_{pl}}{dt} = \frac{dF_{Rcr}}{dt} \tag{2.7}$$

and thus

$$\frac{dF_{pl}}{dF_{Rcr}} + \frac{dF_w}{dF_{Rcr}} = 1 \tag{2.8}$$

were

$$F_w \approx \rho_{cr} g V_{cr} \sin\beta \tag{2.9}$$

$$F_{pl} \approx K \rho_{cr} g \Delta V \sin\beta \tag{2.10}$$

$$F_{Rcr} \approx (\varepsilon S / x) V_{cr} \tag{2.11}$$

were the symbol ≈ indicate that the bulk forces are compared using order-of-magnitude estimates; ρ_{cr} is mean crustal density, β is the ground slope angle, V_{cr} and ΔV are the volumes of new connected crust being formed and new lava entering the core, K is the fraction of the core's new downstream momentum used to pull the crust $(0 \le K \le 1)$, S is the crust tensile strength, and ε and x are the crustal extension and amount of stretching before failure. The product εS represents the mechanical energy per unit volume required to break the crust.

Since the core is volumetrically much larger than the crust and because the crust is persistently brecciating, *Kilburn* [1996] assumed that core resistance dominates crustal restraint, thus equation 2.5 reduces to:

$$F_{Dco} = F_{Rco} \tag{2.12}$$

that, by separating the downstream (x) and cross-stream (y) components becomes:

$$F_{Dxg} + F_{Dxp} = F_{Rx} \tag{2.13}$$

$$F_{Dyp} = F_{Ry} \tag{2.14}$$

were g and p indicate the weight and pressure components driving motions. The magnitude of the driving forces is [*Kilburn*, 1996]:

$$\mathrm{F_{Dxg}} = (\rho g \sin\beta)V \tag{2.15}$$

$$\mathrm{F_{Dxp}} = [(1/2)\,\rho g\,(H/L)\cos\beta]V \tag{2.16}$$

$$\mathrm{F_{Dyp}} = [(1/2)\rho g \alpha^2 (H/W)]V \tag{2.17}$$

were ρ is mean frontal density, V, H, L and W are volume, mean cross-sectional thickness, length and width of the front, and $\alpha = H_m/H$, with H_m maximum cross-sectional thickness.

Core motion is driven by pressure gradients due to the front's sloping surface and by the weight component of the front parallel to the ground. For a front unconstrained by topography, the pressure forces favor radial spreading, while the gravitational forces promote motion downslope. Since flows are elongate downslope, the gravitational force must be greater than the radial pressure force, that is:

$$\mathrm{F_{Dxg}}/\mathrm{F_{Dxp}} \approx 2(L/H)\tan\beta \ge 1 \text{ and} \tag{2.18}$$

$$\mathrm{F_{Dxg}}/\mathrm{F_{Dyp}} \approx \left(2/\alpha^2\right)(W/H)\sin\beta \ge 1 \tag{2.19}$$

which yield a condition on the shape of the rear front zone [*Kilburn*, 1996]:

$$H/W \leq \left(2/\alpha^2\right)\sin\beta \tag{2.20}$$

For the core to widen, it must spreads quickly enough to prevent lateral crustal restrain from becoming significant, that is the rate of crustal deformation (due to core widening) must exceed the rate of crustal strengthening (due to chilling). This implies that the widening time t_w should be comparable to the timescale of crustal healing t_h. The minimum value of t_h is based on the time for a surface to cool below its solidus and it is estimated at ~30 s, whereas the maximum time for widening is that needed for the snout to pass a fixed position, about 1000 s from Etna aa lavas [*Kilburn*, 1993]. When this condition is satisfied the core widens to an equilibrium profile that is approximately parabolic [*Kilburn and Lopes*, 1991].

2.4 The lava flow cooling

A flow loses heat to its surroundings during advance. Cooling thermal boundary layers grow around the flow periphery at a rate limited by conduction and, because lava is a poor conductor, the boundary layers are normally much thinner than the total flow thickness during emplacement. Since lavas are commonly crystallizing upon eruption, flow interiors may also solidify as the boundary layers grow. During solidification, small variations in temperature have a dramatic effect on how lava deforms. Above the liquidus, lava behaves as a Newtonian fluid, below the solidus it can be considered elastic, while at intermediate temperatures, it has been modeled as a Newtonian, pseudoplastic, Bingham plastic or ductile material [*Shaw et al.*, 1968; *Pinkerton and Sparks*, 1978; *Pinkerton and Stivenson*, 1992].

Crustal growth begins as soon as lava is exposed at the surface. Thermal energy is lost, reducing the surface temperature of the lava and increasing the thickness of the cooled layer. The surface temperature drops at a rate controlled by radiation to the atmosphere and it is, initially, the dominant response to heat loss. After a critical chilling time, the rate of surface temperature decrease becomes small and chilled-layer thickening, controlled by conduction through the lava, becomes the more important response. During chilling, the surface temperature drops below the lava solidus and the tensile strength of the crust may approach its maximum value [Kilburn, 1993]. Because of crustal rupture, long-term flow cooling through the surface depends on conduction

across cool, unbroken crust and on radiation from hotter, newly exposed surfaces [*Crisp and Baloga*, 1990].

The temperature gradient along a lava flow is usually small: once the crust has formed, the heat loss is minimal due to the insulating effect of the crust itself. Further heat is also generated by viscous dissipation in the flow, but it is concentrate along the flow base. Most heat loss occurs in the frontal zone where lava becomes directly exposed to the air and flows over a cool surface [*Dragoni*, 1993].

Cooling is the main factor that limits the downslope flow of a lava [*Wadge*, 1978], but solidification of lava is a slow process. Among the various processes of heat loss, conduction to the atmosphere is negligible [*Dragoni*, 1993]. Convection in the atmosphere is responsible for some heat loss, but numerical estimates indicate that its contribution is much smaller than that due to black body radiation [*Murase and McBirney*, 1970]. As to the effect of conduction to the ground it has been shown [*Hulme*, 1982] that flow lengths are generally much less than the distances at which this contribution to the cooling can significantly affect the flow. Heat loss by radiation is therefore the dominant cooling process.

Neri [1998] modeled cooling of diffusion-dominated lava flows (i.e. flows for which conductive-diffusive contributions largely overcomes the convective terms). He took into account heat transfer with the atmosphere (radiation, natural and forced convection), as well as conduction and heat generation due to crystallization within the lava. He considered a two layer flow top composed by a solidified crust and an underlying thermal mushy layer, and described their formation in time and the behavior of the temperature distribution inside the lava. At time t=0 the lava surface starts to exchange heat by radiation and convection with the surrounding atmosphere, supposed at constant temperature. Cooling thus starts and proceeds by conduction toward the lava interior while heat is released inside the lava due to crystallization. The cooling is associated with the growth of a superficial mushy region, and with the propagation of an isothermal plane delimiting the portion of magma not affected by cooling. A crust develops and continues to growth soon after the surface reaches the solidus temperature. At the same time the heat flux at the upper surface decreases due to the decreasing surface temperature. The model also tried to evaluate the influence of surface roughness by considering a flow surface having V-groove or rectangular-groove cavities. Surface

cavities resulted to increase the lava emissivity and thus the heat loss by radiation, having a greater influence on lower emissivity values. They resulted to have a great influence also on natural convection, with heat transfer coefficients of up to three to four times greater than the values typical of a flat surface. Finally the model evaluated the influence of surface roughness on the forced convection. However it did not consider the same cavity geometries but referred to a previous model for a generic roughness which stated that the heat transfer coefficient is proportional to the wind speed and is independent from the surface temperature.

Another cooling model for aa lava flows was defined by *Patrick et al.* [2004], its results were compared with actual data from Okmok volcano (Alaska). The authors considered radiation and convection from the surface as well as conduction to the ground for evaluating the heat transportation from the flow to its surroundings, whereas they took into account only conduction, when evaluating the heat transportation inside the lava flow.

2.4.1 Interaction at the lava surface: radiation and convection

Heat transfer between the lava and the atmosphere takes two forms: thermal radiation is emitted from the flow, while convection is triggered by any buoyancy instability or wind present in the warm air immediately above the flow surface.

The radiative heat flux (q_r) from the lava flow into the atmosphere is expressed by the Stefan-Boltzmann equation:

$$q_r = \sigma\varepsilon\left(T_l^4 - T_s^4\right) \tag{2.21}$$

were σ is Stefan- Boltzmann constant (5.67051 X 10^{-8} W m^{-2} K^{-4}), ε is emissivity of the lava surface and T_l and T_s represent the temperatures of the lava and the atmosphere respectively [*Patrick et al.*, 2004].

When dealing with convection two different contributions from free or forced convection have to be considered. Convection that is fueled by buoyancy only is considered ‘‘natural’’ or ‘‘free’’ convection, whereas forced convection is promoted by wind speed.

Heat loss due to natural convection follows Newton’s law of cooling:

$$q_c = h_c\left(T_l - T_s\right) \tag{2.22}$$

were q_c is the convective heat flux, h_c is the heat transfer coefficient, T_l and T_s are lava and air temperatures, respectively. The natural convective heat transfer coefficient is highly dependent upon surface morphology, especially roughness which can be modeled by triangular corrugations with opening angle ψ [*Patrick et al.*, 2004].

The heat transfer coefficient, both for natural and forced convection, is related to the Nusselt number (*Nu*) by the thermal conductivity of the air (*k*) and the characteristic length factor (*H*):

$$h_c = \frac{Nuk}{H} \tag{2.23}$$

The Nusselt Number definitions are different for natural or forced convection and, when dealing with natural convection it is also necessary do distinguish laminar from turbulent flows.

In the free convection, the transition from laminar to turbulent regimes is given by a critical Rayleigh number:

$$Ra_c = [15.8 - 14\sin(\psi/2)]\cdot 10^5 \tag{2.24}$$

The Rayleigh number is generally defined as:

$$Ra_L = \frac{g\beta(T_l - T_s)H^3}{\nu\alpha} \tag{2.25}$$

were β is the thermal expansion coefficient, $\nu = \mu/\rho$ is the dynamic viscosity and $\alpha = \kappa/\rho c$ is the thermal diffusivity with μ, ρ and c viscosity, density and specific heat, respectively. The six parameters defined above are referred to the air.

Before defining the Nusselt number, it is also necessary to introduce a parameter m, depending only on the opening angle of the cavity:

$$m = 0.148\sin(\psi/2) + 0.187 \tag{2.26}$$

The Nusselt number has different definitions for laminar or turbulent regimes. When the flow is in a laminar regime, that is if $1.8\cdot 10^4 < Ra_L < Ra_C$, the Nusselt number is defined as:

$$Nu = \left[\frac{0.46}{\sin(\psi/2)} - 0.32\right] Ra_L^m \tag{2.27}$$

When the flow is in a turbulent regime, that is if $Ra_C < Ra_L < 1.4 \cdot 10^7$, the Nusselt number is:

$$Nu = \left[0.09 + \frac{0.054}{\sin(\psi/2)} \right] Ra_L^m \tag{2.28}$$

Neri [1998] considered a surface roughness on the order of centimeters obtaining Ra_c between 10^4 and 10^5, and thus a flow in a laminar regime. Under these conditions it is possible to express the convective heat coefficient as:

$$h_c = \lambda (T_l - T_s)^{\delta} \tag{2.29}$$

which, by adopting the appropriate values of the air physical properties, results for a smooth surface as:

$$h_c = 1.0 (T_l - T_s)^{0.33} \tag{2.30}$$

giving values of about 8-10 W/m^{2}K during the whole cooling processes.

Otherwise, for a laminar flow on a corrugated surface, the heat transfer coefficient depends on the characteristic lengths and on the opening angles of the V-groove cavity. By considering characteristic lengths of the order of few centimeters and ψ of 90° and 30°, equation 2.29 becomes, respectively:

$$h_c = 3.5 (T_l - T_s)^{0.29} \tag{2.31}$$

$$h_c = 10.0 (T_l - T_s)^{0.22} \tag{2.32}$$

When dealing with forced convection the Nusselt number should be defined as a function of the Reynolds (*Re*), Stanton (*St*) and Prandtl (*Pr*) numbers.

$$Nu = St \cdot \mathrm{Re} \cdot \mathrm{Pr} \tag{2.33}$$

The Reynolds number relates viscous and inertial forces and determines the transition from laminar to turbulent flow:

$$\mathrm{Re} = \frac{wx}{\nu} \tag{2.34}$$

were w is the air velocity and x is the length scale of the phenomenon.

The Stanton number can be found using the average skin friction coefficient (c_f) assuming a flat surface at constant temperature:

$$St = (c_f / 2) \, \mathrm{Pr}^{-2/3} \tag{2.35}$$

$$c_f = (1.89 + 1.62\log(X/k_s)) - 2.5 \quad (2.36)$$

were X is the characteristic length of the plane and k_s is the typical roughness dimension. Finally the Prandtl number, representing the relation between the velocity and temperature distribution (ratio between kynematic viscosity and thermal diffusivity), is defined as:

$$\mathrm{Pr} = \frac{\nu}{k} = 0.71 \quad (2.37)$$

for air in the range of temperature relevant for the cooling of a lava flow.

Neri [1998] quantified the forced convection from a flat or rough surface, obtaining values of 20 W/m^{2}K and 60 W/m^{2}K. *Patrick and al.* [2004] only assumed a range of plausible h_{fc} values (50-100 W/m^{2}K) owing to the difficulties to constrain the convection parameters. They also stated that *Neri* [1998] model can be applied if the wind speed is equal or greater than 5 m/s, otherwise the convection is to be modeled as natural only.

2.4.2 Heat transfer within the flow: conduction and latent heat of crystallization

Heat transfer within the flow itself, between the flow and underlying ground, and through the ground was modeled by *Patrick et al.* [2004] using conduction only. They stated that for aa lavas convection should, at least theoretically, be occurring within the flow, though the flow cooling calculated using interior convection with conduction gave results very similar to those obtained from conduction only. The conductive heat loss for unit area was calculated by the Fourier's equation:

$$q_k = k(\Delta T/\Delta x) \quad (2.38)$$

were k is the thermal conductivity of the lava and ΔT is the temperature gradient over the distance Δx. *Patrick et al.* [2004] considered lava thermal conductivity as a linear function of the temperature (from [*Murase and McBirney*, 1973]), defined as:

$$k = \begin{cases} -0.0007T + 1.9222 & \text{for T} > 1394 \text{ K} \\ 0.0025T - 2.3844 & \text{for T} < 1394 \text{ K} \end{cases} \quad (2.39)$$

though they stated that there are conflicting data on the relationship between thermal conductivity of igneous rocks versus temperature, with some results indicating that the

value increases with increasing temperature and some indicating the reverse. Finally they also noted that vesiculation, by creating porous spaces within the flow, have a great effect on bulk thermal conductivity of the lava. *Neri* [1998] showed that high vesicularity results in significant decreases in surface temperature and in a slower propagation of the cooling from the top toward the interior of the lava flow.

It should also be noted that a heat source is present inside the lava flow: latent heat is released when lava crystallizes. *Neri* [1998] showed that latent heat strongly limits the thickness of the crust and of the mushy layer and it also contributes to reducing the transmission of the cooling from the top toward the interior of the lava flow.

2.5 Main parameters of a lava flow

Realistic two and three-dimensional models of lava flows require, as input data, accurate measurements of the rheological, thermal and related physical properties of the margin and isothermal interior at different stage in the development of a flow. Moreover they need an accurate reconstruction of the pre-emplacement topography, as well as of the effusion rate trend during emplacement. Such models are essential in hazard assessment and for forecasting the evolution of an ongoing eruption.

While some important properties of lava flows can be measured in the laboratory (e.g. thermal conductivity, coefficient of thermal expansion and electrical conductivity) other measurements must be made in the field. There are significant differences between, for example, measurements of the rheological properties of lavas in the laboratory and similar measurements in the field. These differences are due, partly to differences in volatile contents and partly to the changes which lava undergo during reheating episodes [*Pinkerton*, 1993].

2.5.1 Rheological properties

Rheology is the study of deformation and flow properties of bodies under an applied stress. The rheological properties of lava are of major importance in determining the dynamics of lava flows. Lava can construct is own levees and came to a stop when the supply of fresh lava to the front is removed. Flow fronts are often high and steep, although unconfined by topographic features. *Hulme* [1974] has argued that solidification can limit the motion of a flow front to a certain distance from the effusion

vent, thus limiting the length of the flow, but cannot prevent either lateral or downhill movement at any other point along the flow. Therefore the observed behavior of lava flows must be a consequence of the rheological properties of lava at the high temperatures at which effusion takes place.

From a thermodynamic point of view, lava is a multiphase system, made of solid, liquid and gaseous components. The transition from liquid to solid lava occurs between the liquidus and solidus temperature. Liquidus is the temperature at which fusion is completed during heating, whereas solidus is the temperature at which solidification is completed during cooling. Laboratory experiments showed that, at super-liquidus temperatures, common igneous melts behave as Newtonian fluid. Below their liquidus lavas are instead non-Newtonian. The main reasons for this change are the presence of dispersed crystal and gas bubbles, as well as some polymerization in the silicate melt [*Dragoni*, 1993].

Lavas below the liquidus temperature are generally treated as Bingham fluids, thus it is necessary to evaluate their plastic viscosities and yield strengths, unfortunately only a few measurements of these quantities are available and they show a wide variation. This variation can be related to the strongly dependence of rheological parameters on several factors, including silica and water content, temperature, crystallinity, vesicularity and polymerization [*Dragoni*, 1993]. In situ instrumental measurements of the yield strength for basalts on Mt. Etna have given values of 400-6000 Pas [*Pinkerton and Sparks*, 1978].

2.5.2 Density

The lava density depends on composition and temperature, it decreases with increasing silica content and increasing temperature. Density changes with temperature are within 10% and may not be noticeable when compared with the effects of bubbles and cracks in lava flows, for which it is not possible to predict their volume fraction [*Hidaka et al.*, 2005]. Density values of 2600-2700 Kg/m^3 can be assigned to Etna lavas [*Murase and McBirney*, 1973].

2.5.3 Viscosity

Lava viscosity is greatly influenced by chemical composition and water content, moreover it increase with decreasing temperature. However the viscosity dependence on lava composition was seldom takes into account when modeling a lava flow emplacement [*Harris and Rowland*, 2001; *Vicari et al.*, 2006; *Hidaka et al.*, 2005].
Shaw [1972], *Goto et al.* [1997] and *Giordano and Dingwell* [2003b] related lava viscosity to its composition whereas *Giordano and Dingwell* [2003a] derived a parametric law for Etna lavas, with viscosity depending only on water content and temperature. A comparison between different viscosity models, applied to the main lava flow of the 2001 Etna eruption, is presented in figure 5.2.

2.5.4 Thermal properties

Lava cooling is one of the mechanisms that mainly influence the flow emplacement, therefore it is a crucial point to accurately evaluate the lava thermal parameters, which are specific heat, emissivity and heat transfer coefficients (for conduction and convection). Literature values of the thermal parameters are reported in Table 2.1.

Property	Nominal values
Eruption temperature	1350÷1400 K
Liquidus temperature	1473 K
Solidus temperature	1223 K
Surface emissivity	0.6÷0.9
Thermal conductivity*	1.3 J/(m s K)
Specific heat capacity	1150 J/ (kg K)
Thermal diffusivity	4.2 X 10^{-8} J/(m s K^4)

Table 2.1: thermal properties of basaltic lavas [*Murase and McBirney*, 1973; *Kilburn*, 1993; *Neri*, 1998] *thermal conductivity for approximately 10-15% vesicularity.

2.5.5 Topographic surveys of flow development and flow volume computations

Monitoring the flow evolution has a great importance both for risk management and for understanding and modeling the eruptive processes. As a matter of fact a multitemporal reconstruction of the geometry of a lava flow permits to estimate the emplaced volumes and then to derive the effusion rate trend [*Coltelli et al.*, 2007], being one of the main factors governing the flow emplacement. The flow evolution can also be adopted as checking data for numerical models, simulating the lava flow emplacement [*Vicari et al.*, 2006; *Proietti et al.*, 2006].

Lava flow volume can be derived indirectly from observed or extrapolated geometrical parameters, or directly by subtracting pre- and post-eruption surfaces. The former method, also known as the planimetric approach [*Stevens et al.*, 1999] requires measurements of the flow area, using remote sensing techniques or field data, and mean lava thickness from field surveys. The accuracy of this method strongly depends on the quality of the mapping and on the uncertainties of the thickness measurements. The availability of field-measured 3D points across the entire flow is necessary to obtain reliable results [*Calvari et al.*, 1994; *Stevens et al.*, 1997]. The latter method, known as the topographic approach [*Stevens et al.*, 1999], requires a 3D reconstruction of the topographic surfaces (i.e. DEM generation) before and after the eruption. DEMs can be directly extracted from remote sensing data [*Rowland et al.*, 1999; *Rowland et al.*, 2003] or derived from pre-existing vector maps [*Stevens et al.*, 1999; *Coltelli et al.*, 2007]. The topographic approach can provide more detailed data whose accuracy can be easily assessed.

A number remote of remote sensing techniques are now available for observing the evolution of an eruption in safety [*Baldi et al.*, 2002] and collecting quantitative data useful for monitoring the morphological changes on the volcano surface. In order to monitor a specific eruption parameter (volume and area of the lava field, effusion rates, lava temperature, etc.) the observing system should be selected by considering its temporal and spatial resolution and the achievable accuracy of the measured parameters.

Regarding the geometrical parameters, most of the available satellite-borne systems provide data which, after being georeferenced and rectified, can be used for mapping 2D (planimetric) features, such as lava flow field limits. In this case, estimates of erupted lava volume may be obtained if thickness measurements are available from external data sources. If 3D coordinates of ground points can be measured, it is possible to directly estimate the lava volumes emplaced over a known time period. This can be achieved by reconstructing the surface topography through a Digital Elevation Model (DEM), for example by using SAR interferometry (InSAR) [*Franceschetti and Lanari*, 1999] techniques or processing stereopairs acquired by medium to high resolution sensors [*Curlander and McDonough*, 1991; *Ridley et al.*, 1997]

Limiting factors for the use of satellite data are not only the generally low spatial resolution (with the exception of the recently available high resolution commercial

satellites) but also the constraints stemming from a pre-defined acquisition schedules. Satellite overpasses may, for example, coincide with cloudy periods or may miss short-lived activity altogether.

A more flexible and accurate alternative to the satellite-based methods for DEM generation over large areas is aerial data collection using Light Detection and Ranging (LIDAR) systems [*Fouler*, 2001] and photogrammetric cameras [e.g. *Baldi et al.*, 2002]. Both of these methods permit the acquisition of a large number of 3D points and generation of high-resolution DEMs (space grid density down to few points per square meters). The aerial surveys can be repeated, if logistical and weather conditions are favorable, many times during an eruption and thus these methods are appropriate for monitoring the spatial evolution of lava flows [e.g. *Baldi et al.*, 2005; *Honda and Nagai*, 2002]. Recently, the application of LIDAR systems is increasing [e.g. *Mouginis-Mark and Garbiel*, 2006] due to their capability of acquiring dense 3D point networks which permit accurate representation of terrain features, with less processing time than the photogrammetric technique.

A summary of the main characteristics of the available techniques to directly extract medium to high spatial resolution DEMs is reported in Table 2.2.

	Ground resolution	**Elevation Accuracy**	**Limitations**	**Advantages**
Satellite InSAR	10-20 m	5-10 m	geometrical and radiometric constraints	all-day/weather acquisition
Satellite stereopairs	1-10 m	1-10 m	fixed time schedule day-light acquisition	DEM and orthophoto over large areas
Aerial Photogrammetry	1 m to few meters	1m to few meter	day-light/weather dependent acquisition	flexible schedule
Airborne LIDAR	1 m to few meters	1m to 1-2 m	weather dependent acquisition	Partial penetration under vegetation
Helicopter Photogrammetry/LIDAR	1 m to few meters	1 m to few meters	limited area coverage weather dependent acquisition	flexible schedule

Table 2.2: Main characteristics of the techniques used for direct extraction of 3D points useful for DEM generation.

2.5.6 Effusion rates

Before describing how it is possible to estimate the quantity of lava discharged from one or more vents, it is necessary to give some definitions. Effusion rate is commonly used in volcanology to indicate the instantaneous volumetric flux at which lava is erupted from a source vent or fissure. This is usually referred to an entire eruption which can have multiple vents. The term "effusion rate" is used below (paragraph 4.5.3) to indicate lava discharge rate from a single vent instead of other more specific but not frequently used terms, such as "volumetric flow rate" [*Rowland and Walker*, 1990]. Moreover, the term "daily effusion rate" is utilized to define the average effusion rate during an observation period, obtained by dividing the emitted volume by the corresponding time interval.

A few models [*Wadge*, 1981; *Harris et al.*, 2000] discuss the effusion rate trends observed at different volcanoes. *Wadge*, [1981] observed that many basaltic eruptions begin with a high initial rate of magma discharge which drops slowly to lower value towards the end of the eruption. He defined a brief initial period of 'waxing flow' when the effusion rate rapidly increases toward a peak value, followed by a longer period of 'waning flow', i.e a slow exponential decrease of the lava emission. He partly addressed the 'waxing flow' to magmatic expansion and the 'waning flow' to the release of elastic strain energy from stored magma and the sub-volcanic reservoir. A good example of such an effusion rate trend is that evaluated for the 2001 Etna main lava flow (Figure 4.9). *Harris et al.* [2000] discussed effusion rate trend from fissure-fed eruptions of Etna and Krafla and summit-fed eruptions of Etna. The authors distinguished two different trends: Type I and II. Type I trends, already described by *Wadge*, [1981], have effusion rates that rise rapidly to an initial peak, before declining more slowly, resulting in an exponential decrease in eruption rate. Such behavior was showed only by fissure eruptions, and was explained as the draining of a shallow dyke and/or chambers thus the tapping of an enclosed, pressurized system. Type II trends, identified as typical of persistent Etnean summit eruptions plus one persistent effusive eruption at Stromboli (1985–1986), are characterized by steady effusion rate. They were explained as persistent and steady leakage of a portion or all of the magma supply.

Three different approaches can be adopted to estimate the quantity of lava discharged from one or more vents: a volumetric, a field-based and a thermal approach.

The volumetric approach is based on the estimation of the lava volume emplaced during a known time period. Volumes can be evaluated both from the planimetric or topographic approaches described above, then the daily effusion rate can be derived by dividing the evaluated volumes by the time span. The estimated daily effusion rate can be referred to one or more vents depending on the possibility to discriminate the flows emitted from every single vent. The accuracy and the limits of such measurements depend on that of the volumes. Example of such approach can be found in *Harris and Neri* [2002] and in *Coltelli et al.* [2007].

In the field-based approach the effusion rate is evaluated by in situ measurements of lava velocity (v) and channel width (w) and depth (d). Such measurements must be carried out close to the eruptive vent or, at least along the main channel, otherwise measurements of local effusion rates would be obtained. By considering a Newtonian fluid in an emispherical tube the effusion rate is given as:

$$Q = 0.67 V_{\max} A \tag{2.40}$$

were V_{max} is the maximum flow surface velocity and A is the area of the flow section [*Calvari et al*., 2002] or more simply [*Frazzetta and Romano*, 1984: *Guest et al.*, 1987; *Calvari et al.*, 1994] as:

$$Q = wdv \tag{2.41}$$

Flow thickness is generally estimated from levee heights, though the measurement of channel depths after drainage gives best results. Channel dimension are difficult to obtain with certainty: depth may not be the same as levee height [*Pinkerton and Sparks*, 1976] and width may vary with depth [*Guest at al.*, 1987], especially if thermal and mechanical erosion are occurring. Flow velocity is easily to measure at the flow centre, but variations in the down and cross flow directions, as well as vertically within the channel, result in uncertainty. *Calvari et al.* [2002] stated that the error related to the depth of drained channels is less than 10%, whereas the maximum error on thickness is 30%. They also estimated a maximum error of 10% on channel width and 20% on flow surface velocities. Such values resulted in a cumulative error on the effusion rate of 37%.

In the thermal approach, effusion rate are derived from the radiance measured both from satellite infrared sensors or hand-held thermal camera. Such values are not limited to a single vent but they are referred to the whole lava field. A limiting factor of the satellite based data is the pre-fixed time schedule, which can give a not sufficient temporal detail to define variations in effusion rate. Moreover cloud coverage makes not possible to utilize satellite images, decreasing the number of available data. A useful solution is that of combining thermal data from several satellite-borne radiometer, though they have a different spatial resolution. Low spatial resolution satellite may result not very useful when dealing with little lava flows.

An example of the thermal approach can be found in *Harris et al.* [2000], which combined thermal data from: the Advanced Very High Resolution Radiometer (AVHRR), Along-Track Scanning Radiometer (ATSR) and Thematic Mapper (TM) for evaluating the effusion rate of the 1991-93 Etna eruption (different Etna and Krafla eruptions were also taken into account, though the 1991-93 is the only example of data from all the three satellites).

Effusion rate (E_r) was evaluated following *Harris et al.* [1998] as:

$$E_r = \frac{Q_{tot}}{\rho\left(C_p \Delta T + c_L \Delta \Phi\right)} \tag{2.42}$$

were Q_{tot} is the total thermal flux from the whole flow, that is the sum of heat loss by radiation and convection from the flow surface, plus conduction through the base. The three components of Q_{tot} can be evaluated only after estimating the area affected by lava (A_{lava}) and effective temperature of the lava surface (T_e). Effective temperature allows to take into account the presence of both crust and incandescent lava inside a single pixel and it is defined as:

$$T_e = \left[p T_h^4 + (1-p) T_c^4\right]^{0.25} \tag{2.43}$$

with T_h and T_c being the crack and crust temperature at an active flow, and p the flow portion occupied by cracks.

If a reasonable range is assumed for T_e, the unique unknown quantity is A_{lava}, which can be evaluated from the measured radiance, for example on the AVHRR channel 4, as [*Harris et al.*, 2002]:

$$A_{lava} = \frac{L(T_4,\lambda) - L(T_b,\lambda)}{L(T_{lava},\lambda) - L(T_b,\lambda)} P_{area} \tag{2.44}$$

where L is the spectral radiance emitted at wavelength λ by a blackbody at temperature T, T_4 is the atmospherically, non linearity and emissivity corrected pixel integrate temperature in channel 4, T_b is the temperature of ambient surfaces surrounding the flow (estimated from the radiance of adjacent lava-free pixels) and P_{area} is the pixel area. A great limitation of this application is the necessity to give a range of the effective temperature, thus resulting in a range of effusion rates. This assumption is not so immediate, as a matter of fact the effective temperature may be very different from that measured on the field. Moreover this approach allows to take into account only two thermal components: heat lost from the crust and from the hotter cracks. However a third component, from the ground, must be considered when dealing with very wide pixels, as those of AVHRR (area equal to 1 Km^2).

A three component approach was proposed by *Harris et al.* [1997] utilizing radiances measured on bands 3 and 4 of AVHRR. The two radiances are:

$$R_{iS} = p_h L_i(T_h) + p_c L_i(T_c) + (1 - p_h - p_c) L_i(T_b) \quad i=3,4 \tag{2.45}$$

where T_h, T_c and T_b are the temperatures of the molten lava, chilled crust and lava-free ground occupying a portion p_h, p_c and $(1\text{-}p_h\text{-}p_c)$ of the pixel, respectively. These two equations contain five unknown quantities: p_h, p_c, T_h, T_c and T_b thus it is necessary to fix at least three of these parameters. *Harris et al.* [1997] assumed T_h, estimated T_b from the radiance of adjacent lava-free pixels and gave a range for T_c because field and satellite data showed that crust temperature has a great variability. The availability of two radiance measurements, i.e. from channels 3 and 4, allowed to estimate p_h and p_c. However channel 3 is often saturated thus the two components model must be applied.

Harris et al. [2000] in order to define an effusion rate trend, combined satellite and ground based data which showed a good agreement. Moreover they noted that AVHRR effusion rates were smaller than those of the ATSR. This resulted from the differing sensitivity of the two instruments, ATSR data can give thermal information for high temperature crust and cracks in an active lava flow, but the AVHRR can only give thermal information for the crusts. *Harris et al.* [2000] demonstrated that non consideration of the crack thermal component in the calculation of effective surface

temperature may result in an underestimate of effusion rate by 24±13%. They also stated that some of the observed differences can be addressed to short term variation of effusion rate.

3. Quantitative approaches to model the behavior of lava flows

Different approaches have been developed for describing the evolution of a lava flow and its characteristic dimensions. The first is a mathematical approach devoted to solve the fluid-dynamic of the phenomenon, by considering lava as a Binghamian or Newtonian flow, generally without considering the thermal evolution of a lava flow [*Dragoni et al.*, 1986 and 2005; *Dragoni*, 1993; *Tallarico and Dragoni*, 1999 and 2000; *Macedonio and Longo*, 1999]. The second approach starts by monitoring the flow bulk characteristics, identifies behavior patterns empirically, and uses these patterns to deduce controls on lava emplacement. It is ideally suited to field observation, but has a weaker theoretical foundation though it allows to forecast flow dimensions (e.g. the maximum length) from easily measured variables [*Walker*, 1973; *Pieri and Baloga*, 1986; *Kilburn and Lopes*, 1991; *Kilburn et al.*, 1995]. A third approach consists on the use of analogue experiments to derive flow characteristics. *Kerr et al.* [2006], for example, combined a scaling theory and laboratory experiments to model the flow, on an inclined plane, of a lava with no internal yield strength, then derived the flow width as a function of all the flow variables. Finally the flow emplacement can be modeled by means of simulation codes.

3.1 Mathematical models

The Bingham rheology was adopted [*Tallarico and Dragoni*, 2000] for solving the flow on an inclined rectangular channel. In particular the vorticity and velocity field were evaluated along a transversal cross section of the flow to derive the plug shape. It also appeared that the presence of the plug causes a remarkable decrease in the flow rate in comparison with a Newtonian flow with the same characteristics.

The Bingham rheology was also considered, together with the Newtonian, for evaluating the shape of a lava front [*Dragoni et al.*, 2005]. The authors assumed that the

flow front is moving at constant velocity on a sloping plane, moreover the problem was reduced to two dimensions by assuming an infinite extent perpendicularly to the flow direction. The forces producing the flow advance are the gravity force and the pressure gradient due to the curvature of the flow surface. The authors derived and compared expressions for the longitudinal velocity and the flow thickness of both the considered rheology. Flow thickness was also studied as a function of the lava viscosity while the maximum flow thickness was evaluated as a function of front velocity. Finally, velocity fields were evaluated along the front. The model showed that the shape of the flow fronts depends on rheology: Bingham flows presented a steeper profile than the Newtonian ones. It also demonstrated that, at constant front velocity, higher viscosities gave thicker flow, and thus steeper fronts. The model also took into account the debris accumulation in front of the flow, which resulted in the decreasing of the front slope, moreover the extent of the debris body resulted to increase with increasing ground slope.

The Newtonian rheology was instead adopted by *Macedonio and Longo* [1999] to evaluate how a diversion, due to the creation of an artificial channel, will influence the lava flow. The Newtonian rheology greatly simplified the solution of the mass and momentum balance equations in a 2D geometry representing both the natural and the artificial channel, connected to the first by a gap in the channel margins. The authors investigated the influence of the width of the gap and the slope of the artificial channel, while keeping constant the width of the two channels and the slope of the natural channel. It resulted that the efficiency of the diversion can be increased by enlarging the gap width, and greatly by augmenting the slope of the artificial channel.

Finally *Tallarico and Dragoni* [1999] adopted the Newtonian rheology to model a viscous flow in a rectangular channel down a constant slope, considered as a good approximation to a near-vent Etna flow. They calculated, from an analytical steady-state solution of the Navier-Stokes equation, the surface velocity and the flow rate as a function of flow thickness for different widths. They also took into account the drag on the flow from the non-moving levees, showing their important role in determining effusion rate from the lava flow surface velocity.

3.2 Numerical model for lava flow simulation

Computer simulation is becoming one of the most utilized methods for modeling the emplacement of a lava flow. The existing codes can be generally discriminated in deterministic or probabilistic models [*Costa and Macedonio,* 2005a]. Deterministic models are based on the physical equations describing the phenomenon (mass conservation, momentum and energy balance), while modeling the magma rheological properties, or they can adopt more simple rules. Probabilistic models are based on the statistical evaluation of the most probable path a lava flow will follow. Table 3.1 and Table 3.2 distinguish the existing simulation codes into deterministic or probabilistic models, summarize their main properties, as well as their input and output parameters and the test cases they were applied.

3.2.1 Deterministic models

Three-dimensional physical model

Actually LavaSIM [*Hidaka et al.*, 2005] is the unique simulation code able to solve the physical equations governing the lava motion and cooling. It is based on the 3D solution of the Navier-Stokes and the energy conservation equations, taking into account the lava cooling by radiation, conduction and convection. It account for three-dimensional convection, spreading and solidification, temperature-viscosity dependence of magma, and the existence of a minimum spreading thickness, related to the lava Binghamian behavior. Nevertheless its capability to solve 3D physical equations highly increases the computation time. A fully description of this simulation code will be presented in chapter 5.

Two-dimensional cellular automata models

Cellular automata represents one of the mostly utilized approach for simulating a lava flow emplacement. Cellular automata are based on a division of space into cells and they are generally adopted to describe systems evolving only on the base of local interactions of their constituent parts. The state of each cell specifies the characteristic of the corresponding portion of space; each cell evolves, at constant time intervals, depending on the states of the adjacent cells and according to a specific transition function [*Crisci et al.,* 2003]. Among the simulation codes based on cellular automata it

is possible to enumerate MAGFLOW, SCIARA, Miyamoto and Sasaki and Ishihara's models.

The MAGFLOW model [*Del Negro et al.,* 2007; *Vicari et al.*, 2006] evaluates the lava flow between adjacent cells by means of the steady state solution of the Navier-Stokes equation for a Bingham fluid flowing on a inclined plane [*Dragoni et al.*, 1986]. It is also able to model the flow on a shallow slope by taking into account the pressure gradient due to a not constant flow thickness. Lava cooling is modeled by considering the radiation from flow surface and the heat exchange due to lava mixture between cells, while the applied rheological model takes into account the temperature dependence of the lava viscosity and yield strength. A fully description of this simulation code will be presented in chapter 6.

A 3D model based on CA was developed by *Crisci et al.* [1986] *and Barca et al.* [1987] for simulating the lava flow emplacement. This code was then simplified to a 2D code by *Barca et al.* [1988] and it evolved in the SCIARA code [*Barca et al.*, 1993; *Crisci et al.*, 2003 and 2004]. The SCIARA model partitions the surface into square or hexagonal cells, one or more cells are set as vents and the lava is supplied, according to an effusion rate trend defined in the input data. The state of every cell, defined by a finite automaton *fa*, specifies its physical conditions (altitude, lava thickness, temperature, flow towards adjacent cells,…) at every time interval and it evolves according to a transition function which minimizes the difference in height among the central cell, containing a certain quantity of lava, and its four or six adjacent cells. In this way it is possible to evaluate the lava outflows, which depends on the hydrostatic pressure gradients across the cells. At the same time cell temperature is updated by taking into account the heat exchange due to lava flow and the thermal energy radiated from the cell surface. SCIARA defines an 'adherence parameters', depending on lava temperature by means of an inverse exponential relation, adopted to model the lava rheological resistance and representing the thickness of lava that cannot flow out of a cell. The model is also able to account for the topography variation related to lava solidification. Output data are the 2D distribution of lava thickness and temperature at times defined in the input. A further evolution of the SCIARA model was developed by *Spataro et al.* [2004], by introducing a genetic algorithm applied to evaluate the best values of the input parameters to be used in the simulation.

The *Ishihara et al.* [1989] model subdivides the surface in square mesh and it considers the lava as a Bingham fluid supplied, during each time interval, to a vent cell according to a constant or variable extrusion rate. The lava can be distributed from the vent to the adjacent cells when its thickness is higher than a critical value and the lava flow is evaluated from the steady state solution of the Navier-Stokes equation on an inclined plane [*Dragoni et al.*, 1986]. At the same time the temperature variation is evaluated by considering the mixture of lavas with different temperatures and the heat loss by radiation from the flow surface. Moreover empirical relationship, relating viscosity and yield strength to temperature, are taken into account. The more relevant problem of the code is that the flow between cells depends only on the difference of their elevation but does not take into account the lava thickness variations. This assumption makes not possible the flow on a flat or little inclined plane.

The *Miyamoto and Sasaki* [1997] model can be considered as an improvement of the *Ishihara et al.* [1989] model. As a matter of fact it considers again the steady state solution of the Navier-Stokes equation for a Bingham flow on a inclined plane [*Dragoni et al.*, 1986] though it makes possible the flow for very small slope angle by introducing the pressure gradient due to the change of lava thickness. It also introduce a method for solving the mesh dependence of the cellular automata method, i.e. the dependence of flow length depends on the relative direction of flow and meshes. To overcome the problem they distinguished the adjacent cells in type A and B: A are the cells disposed along the diagonal direction with respect to the central cell whereas B are the cells parallel to the main directions of the central cell, a different probability was related to type A and B cells.

Two-dimensional model based on the shallow water equation

A different approach for simulating the lava flow emplacement was proposed by *Costa and Macedonio* [2005b]. They presented a 2D model based on the shallow water equations, obtained by integrating mass, momentum, and energy equation over the depth of fluid from the bottom up to the free surface. This approach is valid in the limit $H_*^2 / L_*^2 << 1$, where H_* is the undisturbed fluid height and L_* is the characteristic wave length scale in the flow direction. The momentum equation takes into account the gravity and the friction contribution to lava motion, while the energy equation includes

the radiative, the convective and the conductive heat losses as well as the viscous heating. The model considers also an exponential relation between viscosity and temperature and it defines the friction coefficient as a function of viscosity and temperature (exponentially decreasing with temperature). Output of the model are a 2D distribution of lava temperature, thickness and velocity.

Two-dimensional implicit description of the front behavior

The FLOWFRONT model [*Wadge et al.*, 1994] is a 2D description of the front behavior. As a matter of fact it simulates only the front of a lava flow, assuming implicitly the arrival of the lava to the front. At every iteration the cells in the front distributes the lava, exceeding a critical volume (corresponding to a critical thickness, h_{crit}), to their eight neighbors. A minimum thickness (h_{min}), being allowed to flow on that slope, is also defined to reproduce the lava Binghamian behavior and determines the volume of lava which remains in the cell at the end of an iteration. Critical and minimum volumes are inputted for a given slope angle (ϕ), and then evaluated as inverse functions of a generic slope. The lava exceeding the critical volume is distributed among the cells only on the base of their elevation differences, then proportionally to their slope relative to the central cell. Once a cell has successfully distributed all its excess lava, it becomes inactive during next iterations. The simulation result is the 2D distribution of lava thickness. A great limitation of FLOWFRONT is that it considers only the lava motion but it does not takes into account different phenomena governing the flow emplacement, such as lava cooling and crystallization, as well as the dependence of rheological parameters on temperature; though it permits variations of effusion rate and yield strength. Another problem arises when trying to reproduce the temporal evolution of the lava front. As a matter of fact an iteration is not a fixed time interval, thus it is not easy to establish a temporal correspondence between simulated and real flows. Moreover the parameter *incrvol* does not correspond directly to the effusion rate but it is generally selected for supplying approximately enough lava to the front to advance it by one cell length at each iteration.

One-dimensional self-adaptive numerical model

FLOWGO [*Harris and Rowland*, 2001] is a kynematic thermo-rheological model for Binghamian lava flowing in a channel. It simulates a control volumes, advancing along the channel, while cooling, crystallizing and changing its temperature- and crystallinity-dependent rheological factors (viscosity and yield strength). The control volume continues to advance until its velocity drops to zero or the lava core temperature reaches the solidus. The code starts with some given initial conditions at the vent (width, depth and temperature) determining the starting velocity, then the flow depth is hold constant and the mass is conserved whereas channel width and flow velocity vary consequently. Down-flow lava temperature variation is determined by the interplay of heat loss (by radiation, rain falling on the lava surface, forced or free convection and conduction) and heat gained (latent heat of crystallization and viscous dissipation). Output data are the maximum distance that the control volume can extend. The model presents a mean of analyzing lava flow thermo-rheological relationships, identifying important factors in determining how far a channel-fed flow can extend, and assessing lava flow hazard. Although this code adopts a detailed heat budget and an accurate description of lava rheology, its has the great limit to be a one-dimensional code.

Maximum slope probabilistic models

Most of the existing probabilistic models determine the flow path by evaluating the maximum slope direction of the elements forming the volcano topography. Such models do not take into account lava physical properties and rheology, as well as the phenomena governing the lava flow emplacement and cooling. Moreover it is not possible to specify the effusion rate nor to consider the emplacement time. They simply show the most probable paths a flow, emitted from a specified vent, will follow without considering the topography variations due to lava deposit during the eruption. The output of such models is thus a probability of invasion, evaluated as the ratio between the number of paths crossing a given point and the total number of simulated paths. Moreover the use of the topography as the unique parameter determining a flow path and the neglecting of the other phenomena involved in a flow emplacement implies that the obtained probabilities defines a maximum area to be invaded. For these reasons maximum slope models are very useful for the definition of hazard maps and land use

planning, on the contrary they are of little help during crisis management because they do not permit to define the emplacement history and to forecast the flow evolution.

In the *Dobran and Macedonio* [1992] model the lava is assumed to propagate along triangles. The maximum slope direction is utilized to evaluate the probability of transition from a triangle to another by dividing the upslope side of the triangle into two segments. The probabilities of transition towards the two downslope triangles are then evaluated from these segments and compared with a randomly generated number to select the direction to be followed. In this way a different path is generated at every run from the same source vent. The code makes no possible the motion from a lower to a higher triangle whereas it can account for the presence of topographic barriers and the lava thickness by considering an offset between the two elevations. As a matter of fact the flow is allowed only when the elevation of the starting triangle plus the offset is higher than that of one of the two destinations triangles. This model is expected to work well with high terrain slope and to give worse results in flat areas moreover it cannot fill basins because the paths have not thickness, thus a path entering a basin will randomly propagate and spread until it touches the basin walls and stop.

Felpeto et al. [2001] model assumes that the topography plays the major role on determining the path that a lava flow will follow. The flow path is determined by evaluating the probability of transition from a central cell to one of its eight neighbors. This probability is related to the elevation differences between the central cell and its neighbors while taking into account the thickness of the lava in the central cell. A Monte Carlo algorithm (randomly generating a number n_{rnd} between 0 and 1) is used to select the cell were the flow will propagate. The sums of the probabilities toward the cells 0-i^{th} and 0-i^{th}-1 are evaluated (i being comprised between 1 and 8). The path will propagate towards cell i^{th} if n_{rnd} is included between the two sums. The selection rule is not satisfied when the path enters a sink, that is a cell with elevation lower than its eight neighbors, then the path should stop. To avoid the path to stop in a sink, the selection rule was extended, in such a cases, to the sixteen cells surrounding the original eight ones.

The DOWNFLOW model [*Favalli et al.*, 2005], defines a single maximum slope path by evaluating the steepest gradient leaving the vent. Stochastic perturbations are then introduced, by randomly adding a given value ($\pm\Delta h$) at each grid point, to evaluate

a different path. The range of the perturbation (2Δh) is an external input parameter corresponding to the greater of two values, the vertical accuracy of the topography or the characteristic thickness of the lava flow. No stop conditions are normally applied to limit path propagation, implying that the evaluated area is generally overestimated.

The ELFM model [*Damiani et al.*, 2006] is an improvement of the *Felpeto et al.* [2001] approach. As a matter of fact the evaluation of the probability of transition between the cells is the same; though in *Damiani et al.* [2006] the value to be added to the central cell, for simulating lava thickness, is not constant as in *Felpeto et al.* [2001]. Moreover *Damiani et al.* [2006] define a dynamic DEM to avoid the backward propagation of lava flow path: at each step, when the flow propagates from the current cell c to the selected destination cell i, the height h_c is increased of the corrective factor δ, representing the lava thickness. The computation of the paths terminates when: the height of the current cell is lower that that of the sixteen surrounding cells, a maximum number of cell have been computed or when the prosecution of the paths is physically impeded (for example, the path has reached the map border).

3.3 Test cases of simulation codes

3.3.1 Deterministic models

The reliability of the deterministic models was assessed by simulating actual lava flows, generally by means of a qualitative comparison between simulated and observed lava distributions.

The main lava flow emitted on 2001 by Mt. Etna was selected as test case for the validation of the LavaSIM code, the obtained results will be fully described in chapter 5. The LavaSIM code was previously applied to simulate two of the 1986 Izu-Oshima lava flows, one flowing on a gentle slope within the caldera (LBIII) and the on a steep slope down the valley line (LCI) [*Hidaka et al.*, 2005]. These two flows were previously simulated by *Ishihara et al.* [1989], as described below.

The comparison between simulated and observed lava flows was limited to the final flow geometries. The simulation by LavaSIM of the two Izu-Oshima flows gave good results both on the steep and in the gentle slope. However it should be noted that the two flows had very short durations (1 and 5 hours for the LCI and LBIII respectively)

which resulted in low lava volumes (0.16 and 2.3 millions of cubic meters respectively). The low volumes to be distributed probably helped the good fitness between simulated and observed lava flows. In the steep slope the low emitted volume and the short duration implied that flow emplacement was governed only by lengthening without a subsequent phase of thickening. As a matter of fact flow lengthening continued also when the vent was no more fed (i.e. after 1 hour, whereas the simulation lasted 10 hours). As regard to the emplacement on the gentle slope it was mostly dominated by lava spreading until 5 hours, then the vent was no more fed and flow thickening, related to lava cooling, became the dominant mechanism.

The Etna 2001 main flow represents a second example of simulation by LavaSIM on a steep slope (chapter 5). A quite good fitness was obtained, for some of the carried out tests, when the flow emplacement was mostly controlled by flow lengthening, i.e. at the 18 and 19 July (emitted volumes of 0.37 and 1.7 millions of cubic meters respectively). These two examples suggest that LavaSIM is able to reproduce the flow emplacement on a steep slope when it is dominated by flow lengthening but some problems can arise when the real lava flow slows down and lava thickening becomes the prevalent emplacement mechanism (as observed on the Etna flow after the 19 July). This topic will be thoroughly investigated in chapter 5.

The main 2001 Etna lava flow was also adopted for the validation of the MAGFLOW model [*Vicari et al.*, 2006]. The obtained results, showing a quite good reproduction of the actual flow evolution, will be presented in chapter 6. The same code was previously applied to simulate the early phase of the 2004-2005 Etna eruption on Valle del Bove [*Del Negro et al.,* 2007]. This simulation was utilized to check the influence of rheological properties on lava flow morphology and to select the best viscosity-temperature law to be implemented in the code. The simulations were based on syn-eruptive data and the presented results were only qualitatively compared with the observed flow geometry. Probably the simulation of an ongoing eruption made not available high quality geometrical data, such as those utilized for the 2001 eruption (chapter 4). The authors stated that the geometrical comparison between simulated and real flows can be considered satisfactory given also that it was a real-time test and thus its reliability was strongly correlated to that of the collected data.

The SCIARA model was applied to simulate the 1669, 1986-87, 1991-93 and 2001 Etna lava flows [*Barca et al.*, 1993; *Crisci et al.*, 2003 and 2004]; its improved version [*Spataro et al.*, 2004] was utilized to simulate the 2002-03 NE Etna lava flow.

The 1986-87 eruption represents one of the first applications of SCIARA to simulate an Etna lava flow. The eruption was selected because many information on the chronology of flow field emplacement and on vent locations were available, though the variations of discharge rate were not well constrained. The simulation results were qualitatively compared with the actual lava flow showing that the simulation reproduced quite well the lateral limits of the lava flow, though it was composed by single narrow channels whereas the actual flow was a complex flow field. This behavior was probably due to the CA tendency to distribute the lava along the main axis of the cells.

The first 39 days of the 1991-93 eruption were simulated [*Crisci et al.*, 2004] by utilizing effusion rates daily evaluated during the eruption, extrapolated values were adopted when data were missing. Two different simulations were carried out, one using the first SCIARA version (square cells) and the other by the second SCIARA version (hexagonal cells). The last simulation gave best results, more evident on the steepest slope, and permitted to avoid the privileged lava distribution along the main axis of the cells, characteristic of the CA approach. The authors gave only a qualitative comparison between the real and the simulated flow emplacement. They attribute the main discordances to the imprecision of the input data and to the altitude errors of the topographic surface, which were higher than the lava thickness of the eruption beginning. The hexagonal cell version was also utilized during the 2001 Etna eruption to simulate probable evolutions of the lava flow from 2100 m [*Crisci et al.*, 2004]. The actual and simulated flows they obtained are compared in This application did not represent a test to check the reliability of the code but a way to evaluate the hazard posed by an ongoing eruption. Simulations were carried out every days to reproduce the actual flow extension, then many different scenarios were developed by considering different flow rates for the next days. When simulations showed that lava flows threatened inhabited areas, morphology alterations were introduced to reproduce possible operations to deviate the lava flow. The authors stated that vent positions were the only certain data, whereas flow rate were considered approximated, highlighting the problem of the accuracy of syn-eruptive measurements. The simulation of the 1669 Etna

eruption [*Crisci et al.*, 2003] was aimed to evaluate the hazard connected to an eruptive crisis similar to that event, rather than to calibrate the code by comparison with an actual flow. As a matter of fact the 1669 eruption was one of the historical flow which threatened the town of Catania. The position of the eruptive vent, as well as the total emitted volume (1 km^3), were inferred from the eruption description. Since the eruptive history was unknown, a large number of simulations with different eruptive histories were run, allowing to statistically evaluate the hazard in the studied area.

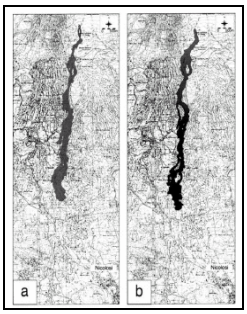

Figure 3.1: actual and simulated extent of the 2001 Etna lava flow from 2100 m a. s. l. after 10 days from the eruption beginning [after *Crisci et al.*, 2004]

The 2002-03 Etna lava flow on the NE flank was adopted as test case to check the introduction in the SCIARA code of a genetic algorithm for calibrating the parameters to be used in the simulations [*Spataro et al.*, 2004]. The selection of the best result was based on a fitness function evaluated as the ratio between the intersection and the union of simulated and observed areas. This function resulted a quite good way to evaluate the correspondence between the simulated and observed areas. However its application to the LavaSIM and MAGFLOW results of the simulation of the 2001 Etna main lava flow (chapters 5 and 6) will demonstrate that it is not sufficient, thus it should be evaluated together with a parameter describing the linear correspondence between simulated and observed flows. The SCIARA simulation evaluated the parameters to be assumed for a specific case and did not test the same parameters on a different flow. A series of actual lava flows with different characteristic should be simulated to evaluate a range of parameters to be adopted for forecasting purposes.

The *Ishihara et al.* [1989] model was applied to simulate three Japanese lava flows differing for their chemical properties: the 1983 Miyakejima, the three 1986 Izu-Oshima and the 1914 Sakurajima lava flows. The result analysis was generally based on the quantitative comparison between simulated and observed final areas and a qualitative

thickness comparison. The description of the emplacement of the Miyakejima flow permitted also to compare the temporal evolution of its real (three measurements) and simulated lengths. The first checkpoint showed a good agreement, then the simulated flow moved faster than the real one. As regard to the Sakurajima flow, the descriptions and photographs of its emplacement allowed to compare also the temporal evolution of its real and simulated lengths and areas. The Miyakejima test showed a good fit between simulated and observed final areas and thickness. The Izu-Oshima tests showed a good fit between simulated and observed final areas and thickness for two lava flows, worse results were obtained for the third flow (LBI) probably owing to the formation, during the eruption, of a scoria cone not included in the simulation. Finally, the Sakurajima test showed an higher overestimated area, with respect to the Miyakejima and the two Izu-Oshima tests. The authors stated that the main discrepancies observed on all the simulations were probably due to imprecision of the topographic data (poor resolution, not updated or with data missing in some zones). They also enunciated some limits of the presented simulation code: the topographic surface is not updated, during the simulation, to take into account its modification owing to lava solidification; the code does not evaluate lava cooling from the sides and thus it underestimates the cooling from the flow margins resulting in a more spread flow; finally the mixture between solidified and liquidus lava is allowed making no possible to simulate intermittently fed lava flows.

It should also be noted that all the carried out tests, but the Sakurajima flow, had very short duration (less than 1 day) resulting in very simple emplacement mechanism, mostly controlled by the terrain morphology. The Sakurajima flow showed the worst correspondence between simulated and real covered area, moreover the best results were obtained for the flows on steep slope. This behavior could have been favored by the topography, perhaps the flows took place in a narrow valley or more probably the obtained path was related to the mesh dependence of the CA, that is the tendency to preferentially distribute the lava along the main cell directions. This implies that the flow length depends on the relative directions of flow and the mesh as showed by *Miyamoto and Sasaki* [1997].

The *Miyamoto and Sasaki* [1997] model was applied to simulate a Bingham flow on a flat plane and the 1983 Miyakejima lava flow, already simulated by *Ishihara et al.*

[1989]. The flow on the flat plane was compared with an analytical theory developed by *Hulme* [1974] without considering viscosity and yield strength variation along the flow and it confirmed the validity of the model for 2D flows. Then the code was applied to simulate the 1983 Miyakejima flow, whose pre-eruption topography, physical lava properties and flow emplacement history were available. The authors gave only a qualitative comparison between the simulated and real flows observing a similar morphology with some discrepancies, mostly around the vent, attributed to the estimation of the effusion rate or to a not correct vent location.

The *Costa and Macedonio* [2005b] model was applied to simulate the 1991-93 Etna eruption between the 3rd and 10th January 1992. The physical parameters to be applied, as well as the average flow rate were derived from literature. The authors reported the simulated lava thickness at the 3rd and 4th January and stated that the model was able to reproduce semi quantitatively the behavior of the real lava flow and the order of magnitude of thickness, temperature and the time of front propagation. Nevertheless no data are shown to support such assertions.

The FLOWFRONT model [*Wadge et al.*, 1994] was deterministically applied to simulate the 1988-1989 Lonquimay eruption. Good planimetric data on the advance of the flow, together with volume estimates were available for the first few weeks of flow permitting to estimate the corresponding average thicknesses. The simulation space was constituted by a 25 X 25 m DEM, interpolated from a topographic map. Average terrain slope and average flow thickness were utilized for setting ϕ and h_{crit} values. *Wadge et al.* [1994] performed a quantitative comparison between simulated and observed flow by evaluating the flow lengths and areas at different simulation stages. They stated that planimetric fit, as measured by overlaying, is poorer than that obtained by distance flowed or area covered, i.e. the ratio between simulated and actual areas. Moreover specific places can be identified where model and reality depart, though the fit between the simulated and real lava flows after 21 days was judged reasonable.

One of the main problem of such a code is that it strongly depends on the parameter choice, and the appropriate range of parameters can be determined from field data only by trial and error. This limits the possibility to use FLOWFRONT for real-time application.

The FLOWGO model [*Harris and Rowland*, 2001] was applied and calibrated by simulating three channel fed 'a'ā flows: the 1984 Mauna Loa flow, the May 1997 Pu´ Ō´ō' flow and the October 1998 Etna flow. FLOWGO does not simulate the emplacement of a lava flow but it only computes the down-flow variations of some quantity characterizing a lava flow (viscosity, yield strength, channel width, lava velocity and heat loss and gain). The three test cases were utilized to calibrate the input parameters to be inserted in the computational model and to check the obtained results. They simulated two different datasets, obtained by a combination of input parameters. In such a way two heat-loss end members were taken into account representing a rapid and a slow lava cooling. The two test cases gave the upper and lower bounds of the expected error.

3.3.2 Maximum slope probabilistic models

Maximum slope models give as a result a map defining the probability of invasion (ratio between number of paths crossing a given point and total number of paths) but not the flow geometry. They were generally applied to define hazard maps or sometimes they were tested by reproducing recent lava flows. The test validations were based only on qualitative comparisons between the area corresponding to the maximum probability and the observed flow spreading. No data exist to carry out a more deep comparison owing to the characteristic of the simulation results.

The *Dobran and Macedonio* [1992] model was applied to simulate the first phase of the 1991-93 Etna lava flow, also by introducing a barrier at Portella Calanna and by taking into account the opening of an ephemeral vent in Valle del Bove. The available topography was no more useful to represent the simulation surface after April 1992, when the lava flow had covered much of the Valle del Bove and Val Calanna. Though the lava flow mapping (areas and average thicknesses) permitted to modify the pre-eruption topography for taking into account the modifications induced by the lava flow. New simulations, from vents corresponding to observed ephemeral vents or lava tunnel obstruction were then carried out to update the probability of invasion during the ongoing eruption. The code was also used to evaluate results from human operation, such as a lava diversion by obstructing a tunnel high in Valle del Bove, and demonstrated that it will result in a threat for towns which otherwise would not be

reached. The code was also applied to evaluate the more probable paths of the 2001 Etna lava flow from 2100 m a.s.l. by carrying out 10000 run from the same vent position (Figure 3.2).

The *Felpeto et al.* [2001] model was applied to define a hazard map for Lanzarote Island. The simulations were performed on the whole Island starting from vents located in a strip (25 x 3 km) where the emission centers of historical eruptions are concentrated. The simulations has been performed twice: the first one by assigning the same probability of being emission centers to all the cells in the strip; the second by considering a probability decreasing from the main axis outwards.

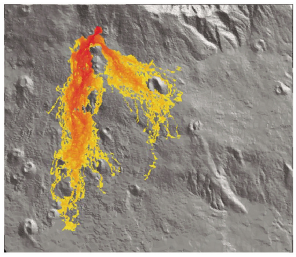

Figure 3.2: simulation, by the Dobran and Macedonio code, of the maximum probable paths from the 2100 m a.s.l. vent of the 2001 Etna eruption. Probability decreases from red to yellow [after *Costa and Macedonio*, 2005].

The DOWNFLOW model [*Favalli et al.*, 2005] was applied to reproduce two Etna lava flow: the 2001 flow from the 2100 m a.s.l. vent (LFS1 in figure 4.2) (Figure 3.3) and the 1991-93 eruption. The probabilities of invasion from the corresponding vents were evaluated by varying the number of runs and the perturbations (Δh) to be applied to the terrain elevation. The 2001 flow spreading was strictly controlled by the morphology (quite steep slope), this could have helped the good fitting considering that the simulated path follows the maximum slope. Nevertheless the simulated flow was much longer than the real flow when stop conditions to limit the path propagation, were not applied. More comparable lengths were obtained when limiting the propagation by a maximum path length, corresponding to the mean length of Endean lava flows from 2100 m a.s.l. [*Guest et al.*, 1982]. The 1991-93 test showed that the simulations seemed to reproduce the temporal flow emplacement when increasing the run number. As a matter of fact the spreading of an actual flow increases with time whereas that of the simulated flow increased with the run number because the flow was allowed to propagate also along the less probable paths. An increased path number also generated

new regions characterized by a lower probability of invasion which can be related to the last areas to be inundated in a real eruption. As a matter of fact the carried out simulations showed that the probability of invasion was related to the time of invasion of the real lava flow.

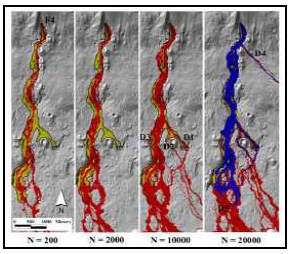

Figure 3.3: application of the DOWNFLOW code for simulating the main 2001 Etna lava flow, the yellow area is the lava field, red areas corresponds to different numbers N of runs, blue areas are the flow path when stop conditions are applied [after *Favalli et al.*, 2005].

Damiani et al., (2006) observed that low values of the probability of invasion are generally obtained even in cells covered by the real lava flow given that the frequency of lava paths overrunning the same point is low, especially for flow on a gentle slope. This makes difficult to establish a threshold for the probability to be meaningful. The authors then decided to compare the historical and simulated coverage and they imposed, as matching criterion, that the simulated lava flow must cover the historical extent. They selected the 1792, 1971 and 1991-93 Etna lava flows as test cases. The simulations were carried out by the ELFM model on a 10 m DEM referring to 1986. The fitting was obtained after more trials for evaluating the best values to be assigned to the maximum flow thickness and length (maxH and maxL respectively), the iteration number (N) and the function defining the variation of lava flow thickness (F). Different values of maxH and maxL were obtained for the three lava flows suggesting that a long tuning on a wide database will be necessary to determine reference parameters before applying the code for hazard mapping or forecasting purposes. Moreover a wide dataset could potentially provide a wide range for the four input parameters. The three simulations covered the areas invaded by the corresponding historical flows; best results were obtained for the 1991-93 lava flow also because the utilized topography referred to 1986 thus it was different from the pre-eruption surface of the 1792 and 1971 flows.

3.3.3 Probabilistic application of the FLOWFRONT model

The FLOWFRONT model [*Wadge et al.*, 1994], already described in its deterministic application (paragraph 3.1.4), was also utilized to define a hazard map for Mount Etna. The probabilistic approach was based on the assumption that future eruptions will have the same behavior as in the studied period (1763-1989).

The description of the front behavior is the same as in the deterministic application though the input parameters are randomly derived, by a Monte Carlo approach, based on observation of the historical (1763-1989) lava flows from flank eruptions (vent altitude below 2600 m). The areal density of vents for the selected data set was used to derive the probability of occurrence of a future vent, also distinguishing between vent producing type A (narrow, simple) and type B (complex, broad) flow fields. These probabilities permitted, by a Monte Carlo selection, to provide the vent coordinates (vent number previously fixed) to be used for different simulations. The historical eruption closest to the proposed vent was then utilized to define the input parameters (minimum and critical thicknesses for flow, slope angle corresponding to the critical thickness and volume of lava supplied at each iteration) to be used for the simulation from that vent. A series of trials to match the observed spatial distribution of observed flows were then performed to create a library of parameter settings corresponding to reasonable fits for each of the historical flows. The performing of 380 gave a probabilistic map (Figure 3.4) of the potential lava flow inundation on the flanks of Etna, showing that the areas having higher hazard are to the east, south and west of the summit.

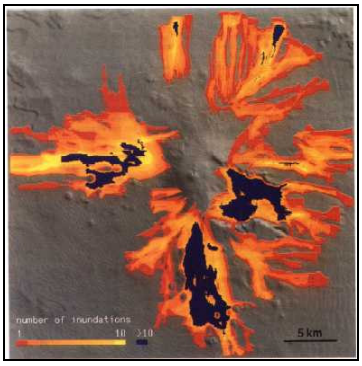

Figure 3.4: probabilistic map of the potential lava flow inundation on the flanks of Etna, colors from red to yellow show the number of times (1-10) an area has been inundated by lava, blue areas are those of greatest hazard where more than ten simulations have flowed [after *Wadge et al.*, 1994].

Deterministic models					
Simulation code	**Type**	**Input parameters**	**Output parameters**	**Test cases**	**Bibliography**
LavaSIM	3D computational fluid dynamics	Pre-eruption surface (DEM) Effusion rate trend Vent position Chemical and physical lava properties	2D lava thickness 3D lava velocity 3D lava temperature 3D cell state (liquid or solid)	1986 Izu-Oshima lava flows 2001 Etna lava flow from 2100 m a.s.l.	Hidaka et al. [2005] Proietti et al. [2007]
MAGFLOW	2D cellular automata	Pre-eruption surface (DEM) Effusion rate trend Vent position Physical lava properties	2D lava thickness 2D lava temperature	2001 and 2004 Etna lava flows	Del Negro et al.,[2007] Vicari et al. [2006]
SCIARA	2D cellular automata	Pre-eruption elevation (square or hexagonal cells) Effusion rate trend vent position Eruption, solidification and intermediate temperatures and adherence values Cooling parameter	2D lava thickness 2D lava temperature	1669, 1986-87, 1991-93, 2001 and 2002-03 NE Etna lava flows	Barca et al. [1993] Crisci et al. [2003; 2004] Spataro et al. [2004]
Ishihara	2D cellular automata	Pre-eruption surface (DEM) Vent position and extrusion rate Physical lava properties	2D lava thickness	1983 Miyakejima lava flow 1986 Izu-Oshima lava flows 1914 Sakurajima lava flows	Ishihara et al. [1989]
Miyamoto and Sasaki	2D cellular automata	Pre-eruption surface (DEM) Vent position and eruption rate Physical lava properties	2D lava thickness	Analytical solution of a Bingham flow on a flat plane 1983 Miyakejima lava flow	Miyamoto and Sasaki [1997]
Costa and Macedonio	2D model based on the shallow water equation	Pre-eruption surface (DEM) Vent position and eruption rate Physical lava properties	2D lava thickness 2D lava temperature	Initial phase of the 1991-93 Etna eruption	Costa and Macedonio [2005b]
FLOWFRONT	2D implicit description of the front behavior	Pre-eruption surface (DEM) Minimum thickness for flow Critical thickness for flow and corresponding slope angle Volume of lava supplied at each iteration	Flow thickness	Lonquimay 1988-1989 eruption	Wadge et al. [1994]
FLOWGO	1D self-adaptive numerical model	At-vent channel width and depth Underlying slope	Down-flow crustal, thermal and rheological parameters Final channel length	1984 Mauna Loa flow 16 May 1997 Pu´ Õ´ō' flow October 1998 Etna flow	Harris and Rowland [2001]

Table 3.1: main characteristics of the deterministic models for simulating the lava flow emplacement

Probabilistic models					
Simulation code	**Type**	**Input parameters**	**Output**	**Test cases**	**Bibliography**
Dobran and Macedonio	Probabilistic maximum slope model	TIN of the pre-eruption surface Vent position	Probability of the lava flow paths	1991-93 Etna eruption	Dobran and Macedonio [1992]
Felpeto et al.	Probabilistic maximum slope model (Monte Carlo simulation)	Probability of the emission centre Pre-eruption surface (DEM)	Probability of each point to be invaded	Lanzarote Island	Felpeto et al. [2001]
DOWNFLOW	Steepest paths over stochastic perturbation of the topography	Pre-eruption surface (DEM) Vent position Entity of perturbation	Percentage of lava flow paths overrunning every cell	1991-93, 2001 and September 2004 Etna lava flows	Favalli et al. [2005]
ELFM	Probabilistic maximum slope model (Monte Carlo simulation)	Pre-eruption surface (DEM) Emission point Maximum number of the cells in a given path Maximum height of the lava flow Function defining lava height variation	Percentage of lava flow paths overrunning every cell	1792, 1971 and 1991-93 Etna lava flows	Damiani et al. [2006]
FLOWFRONT	Monte Carlo simulation	Pre-eruption surface (DEM) Stochastically derived: • minimum thickness for flow to take place • critical thickness (hcrit) for flow to take place • slope angle corresponding to hcrit • volume of lava supplied at each iteration	Hazard map	Etna flank eruption (vent below 2600 m a.s.l.)	Wadge et al. [1994]

Table 3.2: main characteristics of the probabilistic models for simulating the lava flow emplacement

4. The 2001 Etna eruption and its main lava flow

4.1 The eruption narrative

The narrative of the 2001 eruption is hereby reported with the support of six maps (Figure 4.1) which track the complex temporal evolution of the flow field. The six maps are drawn from digital aerial images that were rectified to post-eruption 1:10,000 aerial orthophotos (Figure 4.2) of the Provincia Regionale di Catania (PRC). These aerial images were then georeferenced for outlining the lava flow margins.

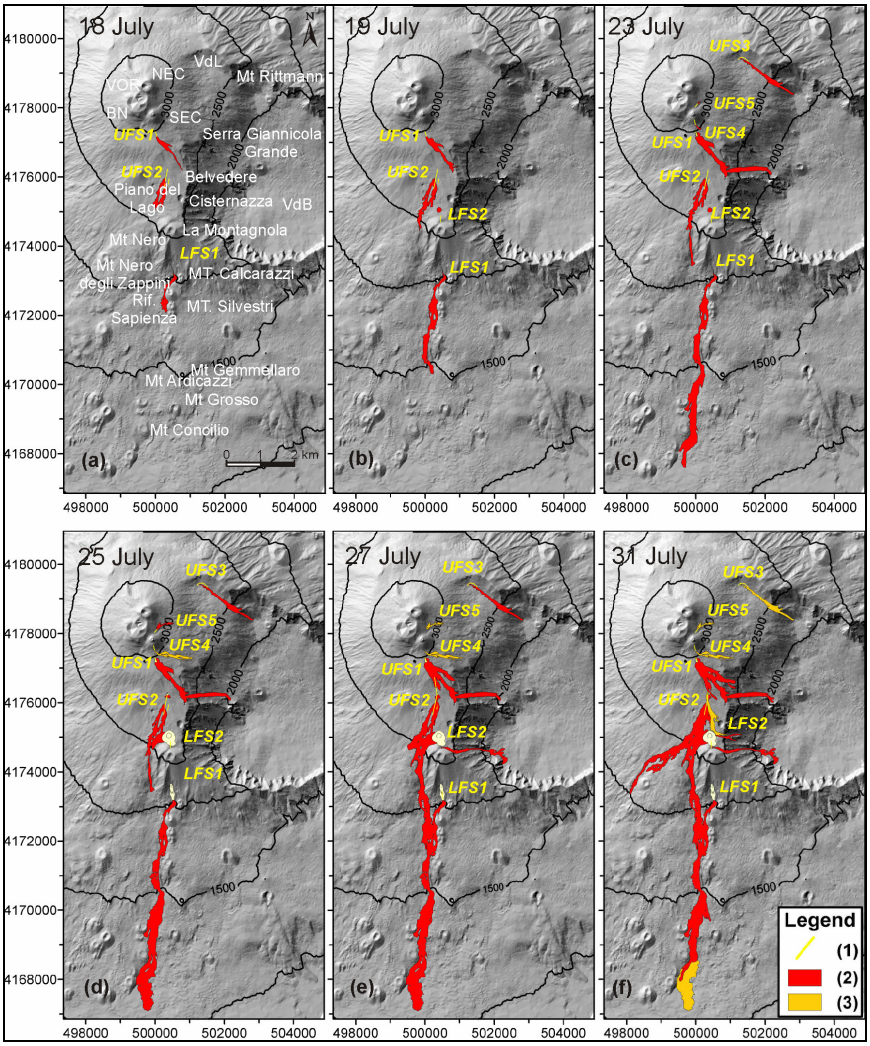

Figure 4.1: Flow field temporal evolution on 18, 19, 23, 25, 27 and 31 July traced on a shaded relief representation of the 1999 DEM. Eruptive fissures (1) are shown in yellow, active (2) and inactive (3) flows are shown in red and orange respectively. Contour lines are drawn every 500 m between 1500 and 3000 m a.s.l.

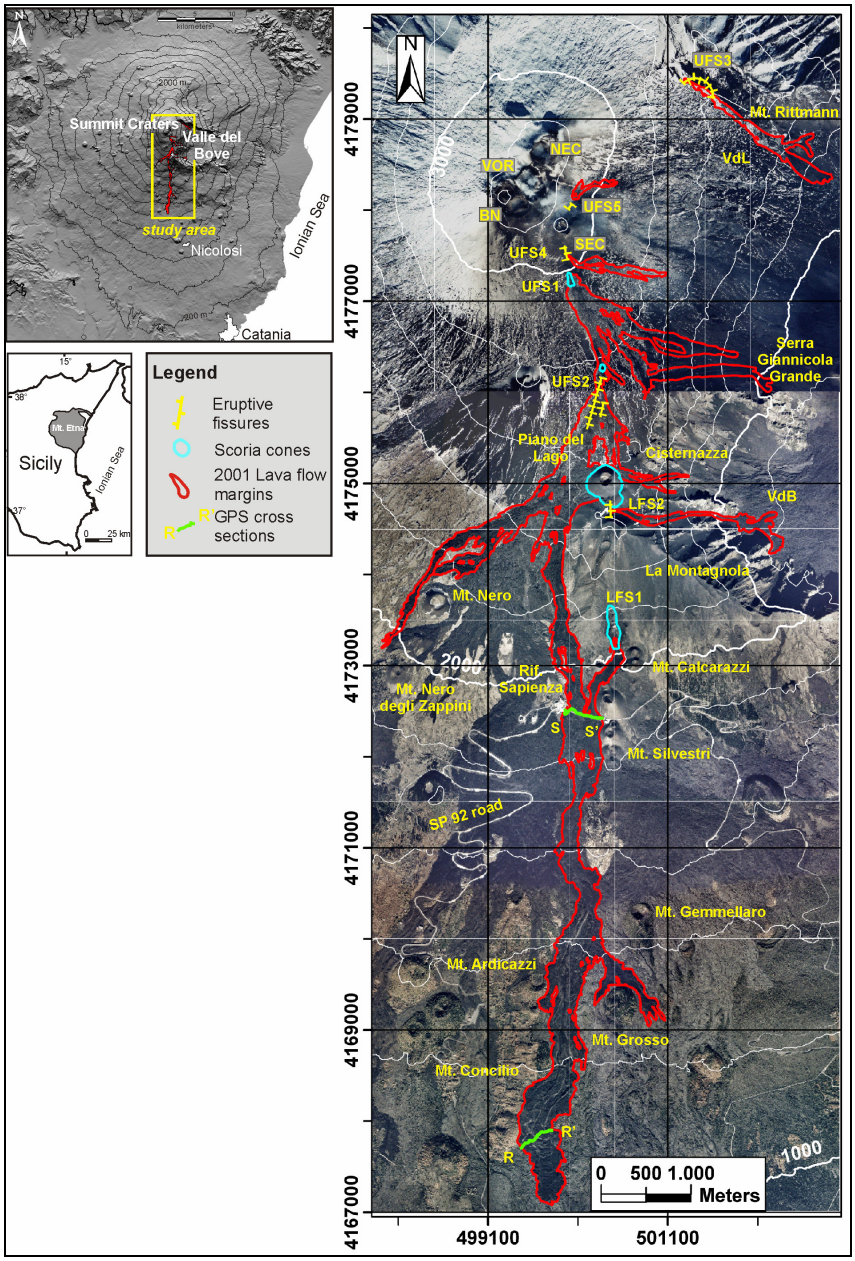

Figure 4.2: Post-eruption orthophotos obtained from the 2001 photogrammetric surveys showing relevant topographic features, lava flows limits (red), eruptive fissures (yellow), scoria cones (light blue) and GPS cross sections (green). The Upper Fissure System (UFS) consists of five fissures: UFS1: 2950 m a.s.l.; UFS2: 2780-2640 m a.s.l.; UFS3: 2600 m a.s.l.; UFS4: 3050 m a.s.l.; UFS5: 3050 m a.s.l. The Lower Fissure System (LFS) consists of two fissures: LFS1: 2100 m a.s.l.; LFS2: 2550 m a.s.l. The summit craters are: Voragine (VOR), Bocca Nuova (BN), Southeast Crater (SEC) and Northeast Crater (NEC). VdB=Valle del Bove and VDL=Valle del Leone. Contour lines are drawn every 200 m between 1000 and 3200 m a.s.l. Insets on the left locate Mt. Etna in the eastern part of Sicily and the study area on the volcano edifice.

During the first three days of the eruption, activity evolved rapidly. The eruption began on 17 July with the almost simultaneous opening of several eruptive fissures on the south and northeast flanks of the volcano, extending between the summit and 2100 m a.s.l. (Figure 4.2). On the basis of structural data and the geochemical composition of the lavas [*Calvari et al.*, 2001; *Corsaro et al.*, 2006], the fissures were subdivided into two main groups each belonging to different eruptive systems (Figure 4.2). The Upper Fissure System (UFS) included those fissures that opened a) at the foot of the South-East Crater (UFS1) and on the flanks of the South-East cone (UFS4 and UFS5); b) on the southern flank between 2780 and 2640 m a.s.l. (UFS2); and c) in Valle del Leone, on the northern flank (UFS3). The Lower Fissure System (LFS), the most hazardous due to its location in relation to human settlements, opened on the southern flank at 2550 m a.s.l. (LFS2) and 2100 m a.s.l. (LFS1).

4.1.1 Activity during 17-18 July (Figure 4.1a)

The eruption began around 7:00 on 17 July, when the eruptive fissure UFS1 opened at the base of the South-East Crater, feeding a lava flow that moved SE. Late in the evening two new fissures (together called UFS2) opened at about 2700 m a.s.l., producing lava flows that spread across the Piano del Lago. A few hours later, at 02:20 on 18 July, the LFS1 fissure opened between 2100 and 2150 m a.s.l., close to Mt. Calcarazzi. The most active effusive vent of the 2001 eruption became established at the lower end of this fissure, emitting a lava flow that extended around Mt. Silvestri and rapidly reached the SP92 road. At the same time, intense phreatomagmatic activity began at the higher portion of the LFS1 fissure and lasted three days.

4.1.2 Activity on 19 July (Figure 4.1b)

While the UFS1 lava flow continued to propagate toward the Belvedere area, the UFS2 flows moved southward and reached 2400 m a.s.l., close to La Montagnola. Late in the afternoon, two pit-craters (LFS2) opened in the Piano del Lago area at 2550 m a.s.l., where an increasing phreatomagmatic ash emission began [*Taddeucci et al.*, 2002; *Scollo et al.*, 2006]. At this time, the main flow from the LFS1 vent had extended below 1450 m a.s.l.

4.1.3 Activity during 20-23 July (Figure 4.1c)

Early on 20 July, the eruptive fissure UFS3 opened at 2600 m a.s.l. in Valle del Leone, feeding a new lava flow. On 23 July one of the flows fed by the UFS2 fissures continued to move approaching the Rifugio Sapienza. A lava flow extended from the UFS1 fissure toward the Valle del Bove. In addition two new short fissures opened on the southern (UFS4) and northern flanks (UFS5) of the South-East Crater. Both fed flows at modest effusion rates. The lava flow fed by LFS1 had extended to 1048 m a.s.l. by the early afternoon of 23 July.

4.1.4 Activity during 24-25 July (Figure 4.1d)

Between 24 and 25 July, most of the flows emitted from the UFS had reached their maximum lengths. At UFS2, continuous overflows covered the upper portions of the previously emplaced lava flow field above 2400 m a.s.l. On 24 July, powerful Strombolian activity gradually built a scoria cone at 2550 m a.s.l. (UFS2). Weak lava effusion characterized activity at UFS5 on 25 July. The UFS3 lava flow in Valle del Leone reached 2100 m a.s.l., partially covering Mt. Rittmann, and the effusive activity at UFS4 ceased. The lava flow originating at the LFS1 vent attained its lowest elevation of 1040 m a.s.l., while a few overflows piled up on the proximal area of the flow field.

4.1.5 Activity during 26-27 July (Figure 4.1e)

At the LFS2 fissure, on 26 July, new lava flows began to issue from the SW base of the cone that had developed on this fissure segment, reaching the SP92 road during the evening and connecting with the LFS1 lava field at 1840 m a.s.l. On 27 July a lava flow emerged from a new vent located at the southern tip of the LFS2 fissure and extended eastward into the Valle del Bove. Explosive activity also built a scoria cone around the higher portion of the LFS1 fissure. At the same time, a marked decrease in the effusion rate caused the most advanced lava front to stop and the emplacement of new flows that overlapped the older flows down to 1400 m a.s.l. On 27 July, a new lava flow extended SSE from UFS1 toward the old Cisternazza pit. At the same time the effusive activity at UFS2 shifted down to 2640 m a.s.l. and ceased at the UFS5 fissure.

4.1.6 Activity during 28-31 July (Figure 4.1f)

By 28 July, the UFS2 lava flow had extended 2 km SW to reach Mt. Nero. Two new lava flows originated from LFS2. The first extended from the NE base of the scoria cone for a short distance eastward. The second extended south-westward from the NW base of the scoria cone. The flow from the southern tip of the LFS2 fissure was still being fed, but its front appeared immobile. The most advanced front of the LFS2 western lava flow reached 1700 m a.s.l. on 29 July and stopped. Likewise, the effusive activity at UFS3 completely ceased on 30 July, at which point the front of the UFS1 flow directed toward the Belvedere appeared motionless. Lava flows fed by LFS1 had active fronts that extended from 1180 m a.s.l. on 28 July to 1060 m a.s.l. on 30 July. At that point a lateral eastern branch developed at 1490 m a.s.l. (close to Mt. Gemellaro) which moved toward Mt. Grosso. A new overflow began from the SW base of the 2550 m scoria cone (LFS2), again threatening Rifugio Sapienza on 31 July.

4.1.7 Activity during 1-9 August

The eruption began to wane following 1 August. The LFS1 lava flow became tube-contained down-slope of 1700-1600 m a.s.l. for a distance of about 500 m, before emerging and flowing to 1080 m a.s.l. Several ephemeral vents formed and emitted lava flows that were less than one hundred meters long. On 2 August two ephemeral vents, located west of Mt. Gemellaro at 1470 and 1460 m a.s.l., produced lava flows that moved toward Mt. Grosso and south-westward, respectively. While the main flow reached 1200 m a.s.l. on 7 August, the lava flow moving eastward toward Mt. Grosso stagnated at about 1240 m a.s.l. The lava flow extending from the LFS2 scoria cone suffered a marked decrease in activity on 1 August and stopped on 2 August. Also the explosive activity at this cone became drastically reduced, being replaced by minor ash emission that entirely ended on 6 August. The front of the UFS1 flow directed toward the Belvedere was moving slowly on 1 August and stopped on 2 August. The flows from UFS2 continued to propagate very slowly toward Mt. Nero, but their fronts stopped on 7 August. However, several overflows remained active until 9 August. Finally, on 8 August the Strombolian activity at the top of the LFS1 fissure ceased and active overflows remained confined above 1900 m a.s.l. The eruption ended during the late evening of 9 August and its final flow field is delimited in Figure 4.2.

4.2 Morphological features of the lava flow field

The lava flow field of the 2001 eruption was mapped using a series of color 1:10,000 scale PRC (Provincia Regionale di Catania) orthophotos acquired on 3 December 2001 (Figure 4.2). The color orthophotos allowed detailed mapping of the lava flow field and description of its main morphological features. In this way it was possible to distinguish the 2001 lava flows from the adjacent fresh lavas (i.e. those of the 2000, 1999, 1989, 1985 and 1983 eruptions) and to reconstruct the 2001 flow field boundaries with a high accuracy. The only limitation of the orthophotos was snow cover towards the volcano summit. In particular, the reconstructions of the lava flows emplaced in the summit area, i.e. above 2600-2800 m a.s.l., were generally characterized by a planimetric error of up to 10 m as a consequence of the poor orthophoto quality and snow cover. Below 2600-2800 m a.s.l., however, the 2001 lava flows were clearly distinguishable and could be mapped with a planimetric error of less than 5 m.

The final flow field produced during the 2001 eruption was the result of lava flow emplacement related to seven fissure systems. The LFS1, LFS2-west, UFS1 and UFS2 vents fed compound lava flow fields. Conversely the LFS2-east, UFS3, UFS4 and UFS5 vents generated simple lava flows [terminology of *Walker*, 1971].

The long-lasting (23 days) effusive activity at the LFS1 vent (UTM-WGS84 coordinates 500506, 4173306) produced a narrow lava flow 6.4 km long, with a maximum width of 545 m, that reached 1040 m a.s.l. (Figure 4.2). This lava flow field was characterized by aa morphology and a large axial lava channel, up to 90 m wide, developed between the vent and about 1700 m a.s.l. The lava flow field down to 1700 m a.s.l. was characterized by the superimposition of several flow units that were mainly related to overflows from the main lava channel. Between 1460 and 1080 m a.s.l. the main lava channel was divided into several secondary channels, with maximum widths of about 100 m. These formed during the uphill regression of the lava flows that began on 26 July. The frontal portion of the lava flow field was produced by the superposition of the lava flow units that drained from the 1460-1080 m lava channels. A secondary branch that developed between 1400 m and 1250 m a.s.l., surrounding Mt. Grosso, was formed by the juxtaposition of several lava flow units between 30 July and 6 August.

The LFS2 fissure comprised four effusive vents located at the base of the large scoria cone built by the strombolian activity, as well as at the southern tip of the fissure. The western vents in this system fed prolonged effusive activity that lasted 15 days and generated a lava flow field that was 3.3 km long, had a maximum width of 265 m and reached 1720 m a.s.l., where it partially overlapped the LFS1 lava flow. This narrow lava field was built by the superposition of several lava flow units that filled a gully on the west slope of La Montagnola down to Rifugio Sapienza. The flow units were supplied from lava channels extending from 2500 m a.s.l., near the vent, to 1900 m a.s.l. In general they showed aa morphology and well developed flow fronts down to a break in slope at 1900 m a.s.l.

The UFS1 vent, located at the south base of South-East Crater, formed a fan-shaped lava flow field that was 2.7 km long and 430 m wide (Figure 4.2). It was active for 14 days and had aa morphology. The lava flow field was the result of the juxtaposition of several single flow units that extended eastward down the western wall of the Valle del Bove and southward (UFS1-LB) towards the LFS2 scoria cone, partially overlapping the UFS2 lava flow. Other flow units piled up in the central portion of the lava field close to the vent.

The 750 m-long UFS2 (2780-2640 m a.s.l.) fissure comprised a small spatter cone at its upper tip and was characterized by lava emission from different points. In 23 days of activity, it formed a lava flow field that was 4.1 km long, 360 m wide, and which reached 1890 m a.s.l., with the flow front reaching a point close to Mt. Nero degli Zappini (Figure 4.2). The lava flows had aa morphology with channels related to the emplacement of single flow units that piled up in the central portion of the flow field. The lateral and frontal portions were characterized by single lava flow units that partially overlapped the flow field from the LFS2 west-vents.

Simple lava flows were emitted from vents that were active for less than 10 days. In particular, the LFS2 east-vents generated two distinct lava flows, 0.78 and 2 km long, respectively, and both less than 150 m wide, that developed along the western wall of the Valle del Bove. The second one, emitted on the southern tip of the fissure, reached the Valle del Bove floor at about 1785 m a.s.l. (Figure 4.2). The UFS3 fissure formed an arc that followed the morphology of the Valle del Leone wall (Figure 4.2). Two emission points established along this fissure generated a narrow lava flow that was 2

km long, had a maximum width of 170 m and which reached 2070 m a.s.l. in Valle del Bove. This flow had aa morphology with a small axial lava channel. The UFS4 vent, located on the SE flank of South-East Crater, formed a lava flow with aa morphology that was 1.1 km long, less than 150 m wide and which extended to 2670 m a.s.l. The UFS5 vent, on the NE flank of South-East Crater, generated a 0.54 km-long lava flow with aa morphology (Figure 4.2).

4.3 Syn- and post-eruption field data collection

During the 2001 eruption, daily surveys were carried out to map the propagation of ground surface fractures and eruptive fissures as well as the evolution of the lava flows. The collected data were plotted onto the 1:10,000 vector map issued in 1999 by the PRC. This allowed to produce preliminary estimates of the daily areas covered by lava flows and to evaluate the rate of advance of the flow fronts.

The lava flows were mapped using digital photos acquired during helicopter over-flights and hand-held GPS measurements collected during ground surveys along the active flow margins and fronts. At each GPS check-point the lava flow thickness was measured using a laser rangefinder with one meter accuracy.

In addition, seven estimates (on July 18, 20, 22, 24, August 1, 4, 8) of the effusion rate were carried out close to the LFS1 vent by measuring the main channel width (w) along with the depth of the molten lava inside the channel (d) and a flow surface velocity (v). Effusion rate Er was estimated from the relation Er = wdv as described by *Frazzetta and Romano* [1984], *Guest et al.* [1987] and *Calvari et al.* [1994]. The measurements were all performed in an area of flat morphology, immediately below the vent, that did not show significant changes during the eruption. The depth of the lava channel was evaluated from the pre- and post-eruption topography. The lava channel depth was considered constant, except for possible thermo-mechanical erosion effects on the lava channel floor, that were assumed limited because of the flat substrate. The maximum flow surface velocity was determined by measuring the time taken by a marker at the centre of the flow to travel between two selected natural targets. The distance between the two targets, the channel width and the depth of the molten lava in the main channel were measured with the laser rangefinder. Several marker speeds were

taken during these experiments to obtain a stable average value. Effusion rates between 30 m^3/s towards the beginning of the eruption and 1 m^3/s at the end were obtained.

During September 2001, one month after the eruption ended, a survey was completed around the margins of the entire lava flow field to measure the final thickness of the flows. As part of this survey, the average thicknesses were obtained for every flow. These were used to calculate the volume of those lava flow field portions, located above 2700 m a.s.l., where the DEM data are not reliable and/or updated.

Finally, for the lava flow field generated by the LFS1 vent, two flow-transverse sections were carried out using a kinematic GPS receiver (Trimble 4700 Geodetic Surveyor). This allowed to measure the local thickness of lava flows with decimeter precision and to obtain the shape and size of lava channels. The first section (S-S' in Figure 4.2) was located in the upper portion of the lava flow field at 1890 m a.s.l. close to Rifugio Sapienza, about 800 m below the vent, where it crossed the main lava channel. The second section (R-R' in Figure 4.2) was located at 1065 m a.s.l., close to Mt. Rinazzi, about 50 m upslope from the lava front in an area with a nearly flat morphology, characterized by the accumulation of lava flows extending from the main lava channel.

4.4 Topographic analysis

The volume and morphology of the flows forming the 2001 lava field were extracted using both topographic and planimetric approaches as described below.

4.4.1 Data collection

The 1999 vector map of the PRC was chosen to characterize the pre-emplacement topography because it was based on an aerial survey performed on 9 November 1998. The post-eruption map of PRC was obtained from an aerial survey performed on 3 December 2001. The two vector contour maps were derived from photogrammetric surveys, whose original data were not available. The map scales are 1:10,000 for the 1999 and 1:2000 for the 2001. The maps contain spot height data and contour lines with intervals of 10 and 2 m for 1999 and 2001, respectively. Contour lines every 10 m were selected from both contour maps in order to provide consistent data for DEM extraction. Both maps, originally referred to the national projection system (GAUSS-BOAGA-

Datum Roma40), were converted into the UTM-WGS84 coordinate system by applying the necessary transformation.

The 1999 map covers the whole province of Catania, subdivided in 7.5 x 5.5 km tiles, whereas the 2001 is limited to the eruption area and has an irregular shape (Figure 4.3). Their comparison revealed a geometric inconsistency both in the planimetric and vertical components, probably due to an inaccurate photogrammetric processing of the 2001 map. A procedure for improving the matching with the 1999 map was thus applied to the 2001 map before DEM extraction, as described in section 4.3.

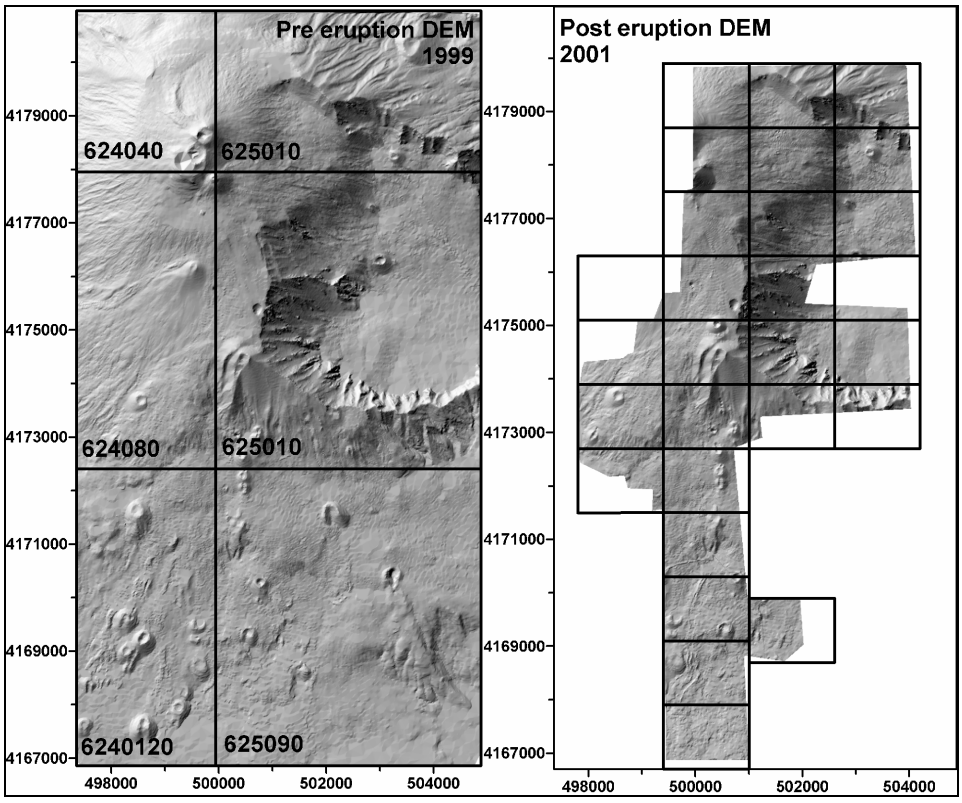

Figure 4.3: Shaded relief images of the 1999 (left) and 2001 (right) DEMs and tiles that comprise the corresponding cartographies.

4.4.2 DEM extraction

The TIN (Triangular Irregular Network) method, based on Delaunay triangulation [*Lee and Schachter*, 1980], was utilized to interpolate elevation data. The TIN method partitions a surface into a set of contiguous, non-overlapping triangles. A height value is recorded for each triangle node. A mask delimiting the 2001 map area was drawn and

the TIN method was applied across this mask to avoid triangulation in areas with no height data.

The DEMs interpolated from the TIN were used to reconstruct the 1999 and 2001 topography in a grid format, which is more appropriate for conducting spatial analysis, such as volume estimation. The DEM grid size was set to 10 m which was considered appropriate given the data spacing and the minimum flow widths, i.e. about 50 m for the main channels and 20 m for the front fingers.

4.4.3 Improvement co-registration of the DEMs by means of residual analysis

A detailed comparison of the two DEMs was carried out on the whole map area in order to evaluate the method accuracy and check their co-registration. Elevation residuals outside the lava flow margin (terrain residuals) were used to assess horizontal and vertical mis-alignments between the two DEMs. Figure 4.4 shows the elevation differences on the whole map area and the histograms represent the distribution of the terrain residuals. Terrain residuals in the upper portion of the map are not useful for assessing the method accuracy due to the presence of lava flows emplaced between 1999 and 2001, thus the following analysis is limited only to the rectangular area delimited on Figure 4.4a.

The terrain residuals in Figure 4.4a show the presence of horizontal misalignments and vertical shifts that were particularly severe at the southern edge of the map. The residuals are bimodally distributed, showing a first peak around zero and another between -15 and -10 m (Figure 4.4d). In order to improve the matching in the southern portion (rectangular box in Figure 4.4b), the 1999 and 2001 maps were superimposed, tile by tile and corresponding points were used to estimate the rotation and translation parameters and the vertical shift (about -10 m) to be applied to the 2001 map. The extracted 2001 DEM was compared to the 1999 DEM, resulting in the residual map of Figure 4.4b which shows a symmetric distribution of the terrain residuals (Figure 4.4e) having a mean value of -1.01 m and a standard deviation of 4.15 m. Unfortunately, such uncertainties have the same magnitude as the expected lava thickness, thus additional improvements were applied before computing lava volumes.

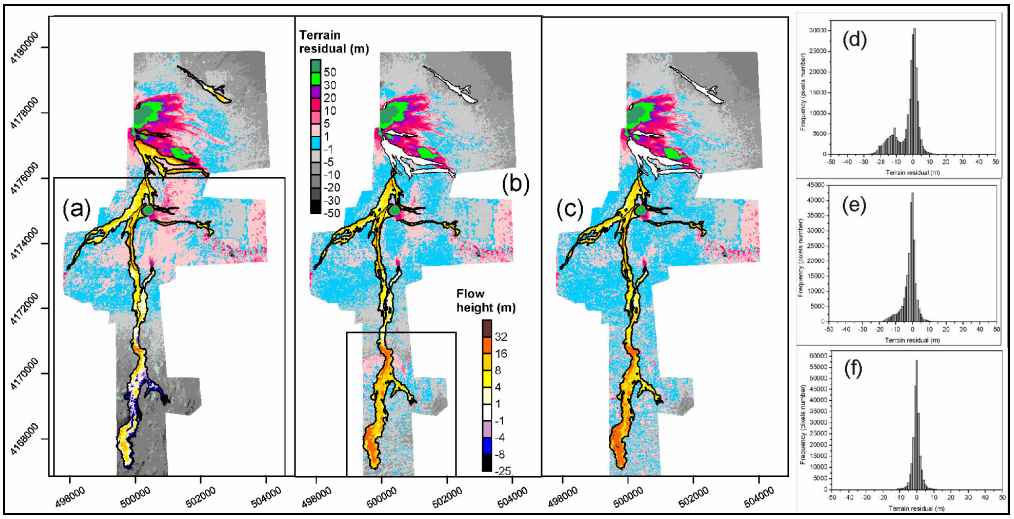

Figure 4.4: Elevation residual analyses. (a) First evaluation between the 2001 and 1999 DEMs. The black box limits the selected area for residual distribution study. (b) Second evaluation after rotation, translation and height correction of the 2001 DEM. The black box limits the area where the 2001 cartography was modified. (c) Final evaluation, between the 2001 DEM, after masks application, and the 1999 DEM. Terrain residual and flow height color scales are the same for the three evaluation steps. White flows are those for which the planimetric volume evaluation was carried out. Histograms on right show terrain residual distributions (class interval 1 m): d) first evaluation: e) second evaluation; f) final evaluation.

The procedure consisted of i) definition of masks with homogeneous terrain residuals, ii) evaluation of average terrain residuals inside every mask and iii) subtraction of the residual mean values from the 2001 DEM. The 2001 DEM was again compared with the 1999 DEM, resulting in the residual map of Figure 4.4c which shows a symmetric distribution of the terrain residual (Figure 4.4f) with a mean value of 0.25 m and a standard deviation of 2.69 m. This result is in accordance with the expected elevation accuracy (about 2 m) of a 1:10,000 scale map.

To estimate DEM quality using external data, two GPS cross sections (SS' and RR' in Figure 4.2) were compared with the corresponding sections extracted from the 2001 DEM. The GPS- and DEM-derived cross sections show good agreement, although some small-scale height variations did not appear on the DEM-derived profiles (Figure 4.5). The estimated differences between the two datasets had a mean of -0.99 m with a standard deviation of 1.86 m for the SS' profile, and a mean of -0.64 m and a standard deviation of 2.09 m for the RR' profile.

Unfortunately, the estimated accuracies, although in good agreement with that obtained from terrain residual distribution, could not be applied to the whole dataset because they were only valid for the LFS1 flow. Thus the terrain residual standard deviation of 2.69 m was adopted to represent the vertical accuracy of our lava thickness calculations.

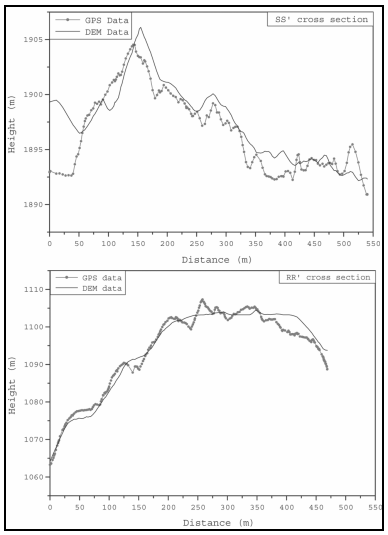

Figure 4.5: Comparison between the GPS and DEM derived cross sections located near Rifugio Sapienza (SS') and Mt. Rinazzi (RR'). See Figure 4.2 for locations.

4.4.4 Lava flows volume evaluation

Lava flow volumes were calculated by subtracting the 1999 and 2001 DEMs in regions where the two datasets were considered reliable and updated. DEMs are not updated in the area covered by the lava emitted after the survey date and before the 2001 eruption. DEMs are reliable where the terrain residuals, evaluated after the improvement in DEMs co-registration, are characterized by a sufficient accuracy (i.e. comparable with the standard deviation of 2.69 m). On the contrary, the volumes of flows covering regions where the quality of the DEMs provided to be not acceptable or where the DEMs are not updated were obtained by multiplying flow area by the corresponding average lava thickness. The equations used to estimate the volumes and the relative standard deviations are given in Appendix A.

The DEM subtraction technique could only be applied to flows located below 2700 m a.s.l., i.e. those emitted from the LFS1 and LFS2 vents, the lower branch of that emitted from the UFS1 vent and the upper branch of that emitted from the UFS2 vent (respectively UFS1-LB and UFS2-UB in Table 4.1). Analysis of the UFS1-LB flow was

complicated by the fact that it partially overlapped the UFS2-UB, similarly the front of the LFS2 flow partially overlapped the LFS1 flow. Because the overlapped areas were very small, the errors due to not considering the UFS2-UB volume lying under the UFS1-LB and the LFS1 volume lying under the LFS2 flow were considered negligible.

Lava flow	Cut area (10^6 m^2)	Unchanged area (10^6 m^2)	Fill area (10^6 m^2)	Total area (10^6 m^2)	Total volume (10^6 m^3)	St. dev. of tot. vol. (10^6 m^3)	Relative error
LFS1	0.02 0.92 %	<0.01 0.10 %	1.93 98.98%	1.95	21.40	0.37	1.7%
LFS2*	0.01 1.43%	<0.01 0.02%	0.90 98.55%	0.91	6.39	0.16	2.5%
UFS1-LB	<0.01 0.68 %	<0.01 0.07 %	0.14 99.25%	0.15	0.82	0.05	6.1%
UFS2-UB	<0.01 0.78 %	0.01 0.39 %	0.76 98.83%	0.77	4.71	0.12	2.6%

Table 4.1: Lava flow volumes and areas evaluated by comparing the 1999 and 2001 DEMs, both the effective and percent values are reported for the areas. LFS2* includes the volume of the UFS2 lower branch (UFS2-LB in Table 4.3)

Volume estimation by DEM subtraction (Table 4.1) was carried out using a mass balance analysis, included in a GIS toolset, and permitted evaluation of surface loss (cut) and gain (fill). In order to restrict the volume computation to the flow field area, the lava flow field limits, mapped on the 2001 orthophotos, were used to mask the 2001 DEM and dagala (Sicilian name for areas not covered by lava within the flow borders) limits were also taken into account. The areas with zero or negative elevation change within the lava flow field limits were not considered in the volume estimation. The elevation changes in these areas most probably were within the DEM uncertainty of 2.69 m, or the flow limits were not correctly defined. However, their contributions represent less than 2% of the total flow areas (Table 4.1), so that their exclusion has a negligible impact on the volume estimations.

The volumes of the other lava flows cannot be estimated from the DEM subtraction. Lava flows erupted from the fissures that opened on the South-East Crater cone (UFS5 and UFS4) and from the UFS1 vent (excluding its lower branch UFS1-LB), overlap lava emitted between late 1998 and 2001. The Valle del Leone lava flow (UFS3) lays within an erroneously georeferenced part of the 2001 map. Volumes for these flows (Table 4.2) were thus estimated by means of the planimetric approach, that is by

multiplying the corresponding areas by their average thicknesses, obtained from levée heights measured after the end of the eruption. Moreover the lower branch of the UFS2 flow (UFS2-LB in Table 4.2) is partially covered by lava emitted from the LFS2 vent. Its volume was evaluated by multiplying its area, reconstructed from the aerial photos, by its thickness, estimated from cross sections extracted outside and inside the overlapping area.

Lava flow	Area (10^6 m^2)	Average thickness (m)	Volume (10^6 m^3)	St. dev. of vol. (10^6 m^3)	Relative Error
UFS1-UB	0.70	7.0	4.87	1.18	24.2%
UFS2-LB	0.19	6.0	1.14	0.35	30.7%
UFS3	0.22	7.0	1.53	0.51	33.3%
UFS4	0.09	2.9	0.26	0.13	50.0% *
UFS5	0.03	3.3	0.10	0.07	70.0% *

Table 4.2: Average thicknesses, areas and volumes (evaluated by means of the planimetric approach) of the UFS1 upper branch, UFS2 lower branch and of the UFS3, UFS4 and UFS5 flows. * These large relative errors are due to areas and thicknesses values being of the same magnitude of their associated uncertainties.

Table 4.3 reports the total volumes obtained for the seven flows composing the 2001 lava field by combining the results of Table 4.1 and Table 4.2. The volume of the whole lava field was estimated to be 40.1 x 10^6 m^3; about 53% of this volume (21.4 x 10^6 m^3) was emitted from the LFS1 vent.

Lava flow	Area (10^6 m^2)	Average thickness (m)	Volume (10^6 m^3)	St. dev. of vol. (10^6 m^3)	Relative error
LFS1	1.95	11.0	21.40	0.37	1.7%
LFS2	0.91	5.8	5.25	0.15	2.8%
UFS1	0.85	6.7	5.69	0.97	17.1%
UFS2	0.96	6.1	5.85	0.12	2.0%
UFS3	0.22	7.0	1.53	0.51	33.2%
UFS4	0.09	2.9	0.26	0.13	
UFS5	0.03	3.3	0.10	0.07	
Total	**5.01**	**8.0**	**40.08**		

Table 4.3: Average thicknesses, areas and volumes of the seven composite flows forming the 2001 lava field. LFS2 volume is the difference between LFS2* and UFS2-LB; UFS1 volume is the sum of UFS1-LB and UFS1-UB; UFS2 volume is the sum of UFS2-UB and UFS2-LB.

4.5 Reconstruction of the temporal evolution of the LFS1 lava flow

Helicopter surveys were carried out almost every day during the 2001 eruption to collect digital photos. These allowed to reconstruct the lava flow evolution in plan view and by integrating field data, to estimate partial and cumulative volumes. The attempt to

perform a daily reconstruction of the lava flow evolution is unfortunately limited to the lava flow emitted from the LFS1 vent because the field mapping performed during the eruption was not detailed enough (in space and in time) to extend it to the whole lava flow field.

4.5.1 Daily map preparation

Daily maps were drawn on the basis of the photo availability, quality and usefulness (in Table 4.4 "not useful" means that no significant modifications of the lava flow had occurred since the previous mapping). To check the mapping accuracy, a retroactive procedure was carried out whereby every map was cross-checked. This involved starting with the final map (9 August) obtained from the orthophotos, checking the previous map against it and moving backwards in time through the sequence to the first map, corresponding to the flow of 18 July.

Day	Vector Map	Helicopter Photo
17/07/01	No lava flow	Yes
18/07/01	Yes	Yes
19/07/01	Yes	Yes
20/07/01	Yes	Yes
21/07/01	No	No flight
22/07/01	Yes	Yes
23/07/01	Not useful	Photos shot too far
24/07/01	No	Photos not utilizable
25/07/01	Not useful	Yes
26/07/01	Yes	Yes
27/07/01	Not useful	Yes
28/07/01	Yes	Yes
29/07/01	Not useful	Flow front photos not utilizable
30/07/01	Yes	Yes
31/07/01	Not useful	Yes
01/08/01	Not useful	Yes
02/08/01	Yes	Yes
03/08/01	Not useful	Yes
04/08/01	Yes	Yes
05/08/01	Not useful	Yes
06/08/01	Yes	Yes
07/08/01	Yes	Yes
08/08/01	No	Flow front photos not available
09/08/01	Yes	Yes

Table 4.4: List of the vector maps and helicopter photo sets available for the LFS1 lava flow.

The daily map reconstruction permitted to mark off active areas inside the lava flow after 26 July, when the regression of the active flow front began. Information on flow front position were also obtained from the daily INGV Sezione di Catania reports and

utilized as an additional check. Figure 4.6 shows the temporal evolution of the LFS1 lava flow between 18 July and 09 August. On the basis of the daily maps the flow emplacement can be divided in three phases. The 1st phase (18 – 26 July) involved lava flow lengthening. The 2nd phase (28 July – 2 August) and 3rd phase (4 – 9 August) respectively revealed slow and then fast regression of the active flow fronts, accompanied by development of minor branches.

4.5.2 Daily volume evaluation

The planimetric approach was utilized to evaluate the daily volumes of the LFS1 flow. Active flow areas were measured on the daily maps (Figure 4.6) while the daily average thicknesses were derived from a combined analysis of syn- and post-eruption data. Syn-eruption thicknesses were mainly measured on the flow front whereas final flow thicknesses, extracted from the 2001 DEM, were available for the whole lava flow.

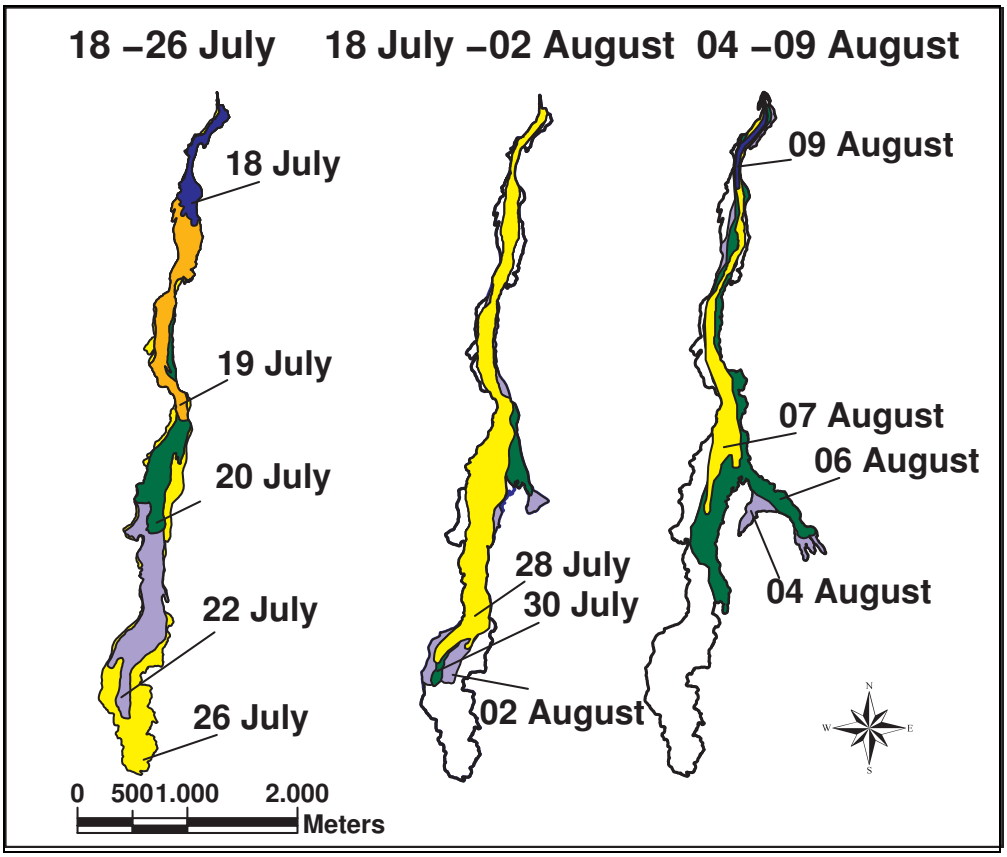

Figure 4.6: LFS1 lava flow temporal evolution. Colored areas are active while, after the 26 July, white areas inside flow limits are not active.

On the basis of both the lava flow emplacement history (see paragraph 4.1) and the analysis of the flow final morphology, the LFS1 flow was divided into seven homogeneous zones (Figure 4.7a). The quantitative analysis of the flow evolution was then performed separately for each zone, providing the results (daily active areas and average thicknesses) listed in Table 4.5 and Table 4.6 respectively.

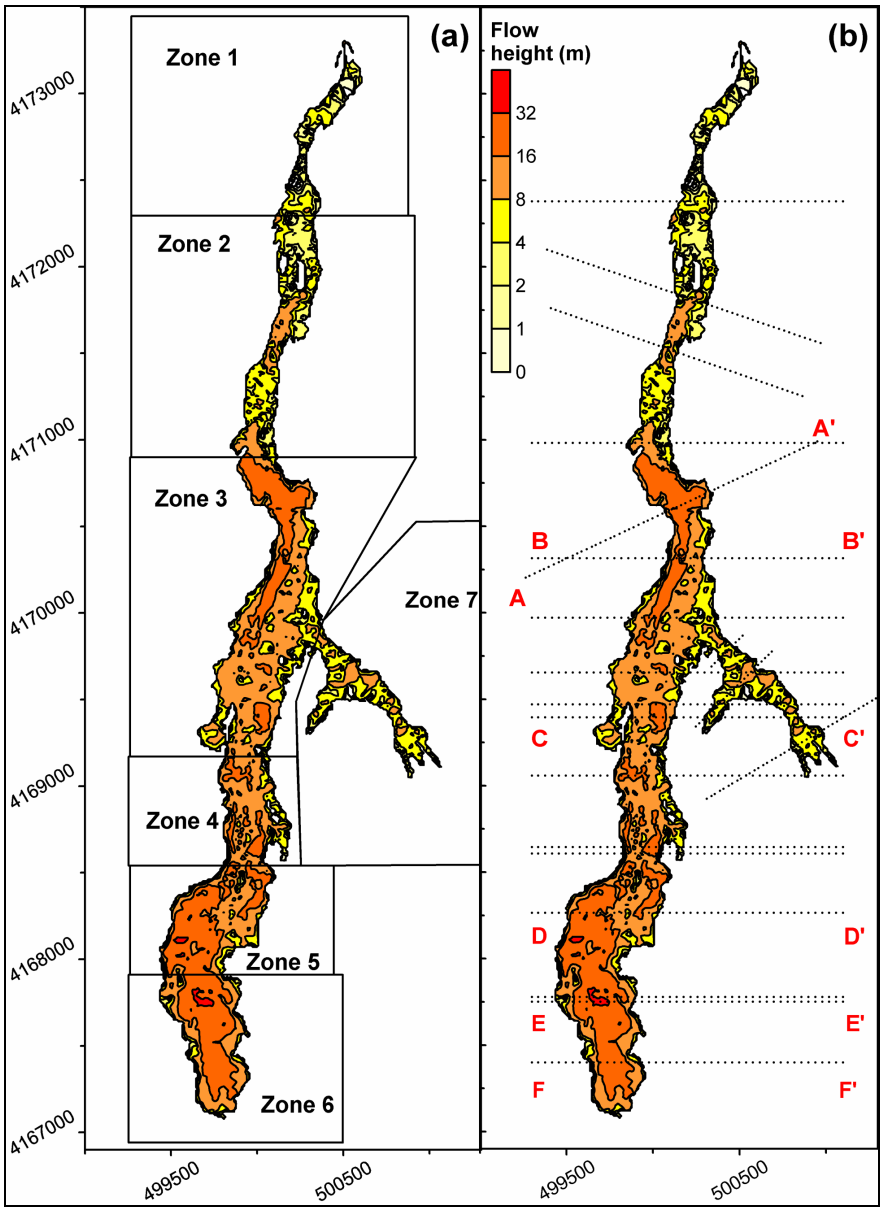

Figure 4.7: LFS1 lava flow final thickness; (a) black boxes limit the seven zones (defined on the basis of both the lava flow emplacement history and the analysis of the flow final morphology) in which the flow was divided; (b) dotted lines are the twenty cross sections tracked along the flow; cross sections on the eastern branch are shorter than those on the main flow in order to limit the thickness evaluation to the secondary flow.

Date	Active area (10^6 m^2)							Total Active Area (10^6 m^2)
	Zone 1	Zone 2	Zone 3	Zone 4	Zone 5	Zone 6	Zone 7	
18/07/01	0.10	0.02	0.00	0.00	0.00	0.00	0.00	0.12
19/07/01	0.10	0.24	0.07	0.00	0.00	0.00	0.00	0.40
20/07/01	0.10	0.25	0.29	0.00	0.00	0.00	0.00	0.54
22/07/01	0.10	0.25	0.36	0.13	0.16	0.03	0.00	1.02
26/07/01	0.11	0.27	0.43	0.14	0.26	0.28	0.00	1.54
28/07/01	0.07	0.18	0.41	0.15	0.08	0.00	0.00	0.88
30/07/01	0.07	0.18	0.47	0.14	0.06	0.00	0.01	0.94
02/08/01	0.06	0.15	0.36	0.15	0.18	0.00	0.03	0.93
04/08/01	0.10	0.18	0.42	0.08	0.00	0.00	0.17	0.95
06/08/01	0.08	0.15	0.42	0.08	0.00	0.00	0.10	0.84
07/08/01	0.06	0.10	0.22	0.00	0.00	0.00	0.00	0.38
09/08/01	0.08	0.00	0.00	0.00	0.00	0.00	0.00	0.08

Table 4.5: Daily evaluation of active areas on the seven zones composing the LFS1 flow. Last column shows the daily total active area, i.e. the sum of the seven active areas.

	Thickness (m)						
Date	Zone 1	Zone 2	Zone 3	Zone 4	Zone 5	Zone 6	Zone 7
18/07/01	3.0	3.5	0.0	0.0	0.0	0.0	0.0
19/07/01	3.0	3.5	8.0	0.0	0.0	0.0	0.0
20/07/01	3.0	3.5	8.0	0.0	0.0	0.0	0.0
22/07/01	3.0	3.5	10.0	10.0	13.0	14.0	0.0
26/07/01	3.0	3.5	10.0	10.0	13.0	16.5	0.0
	Additional thickness (m)						
28/07/01	0.0	0.5	3.0	3.0	3.0	0.0	0.0
30/07/01	0.0	1.0	1.5	1.5	4.0	0.0	3.0
02/08/01	0.0	1.0	1.0	1.0	4.0	0.0	3.0
04/08/01	0.0	0.0	0.5	1.0	0.0	0.0	3.0
06/08/01	0.0	0.0	0.5	1.0	0.0	0.0	3.0
07/08/01	0.0	0.0	0.5	0.0	0.0	0.0	0.0
09/08/01	1.0	0.0	0.0	0.0	0.0	0.0	0.0

Table 4.6: Daily values of thickness evaluated on the seven zones composing the LFS1 flow.

Daily thicknesses were evaluated by examining twenty cross sections distributed along the flow (Figure 4.7b). Some of these sections (Figure 4.8) allowed to extract the thickness of the first emplacement unit, corresponding to the flow maximum planimetric expansion reached on 26 July. On the cross sections in Figure 4.8 the widest zones, having a thickness of 10-15 m, correspond to the first emplacement phase (18 – 26 July). Overlapping layers and localized accumulation peaks are related to the piling up of flow units during the active front regression (28 July - 9 August). During this period the active areas were restricted to the central portion of the channel zone (Figure

4.6), thus the flow thickening is limited to this part as evidenced by the reduced width of the overlapping layers (Figure 4.8).

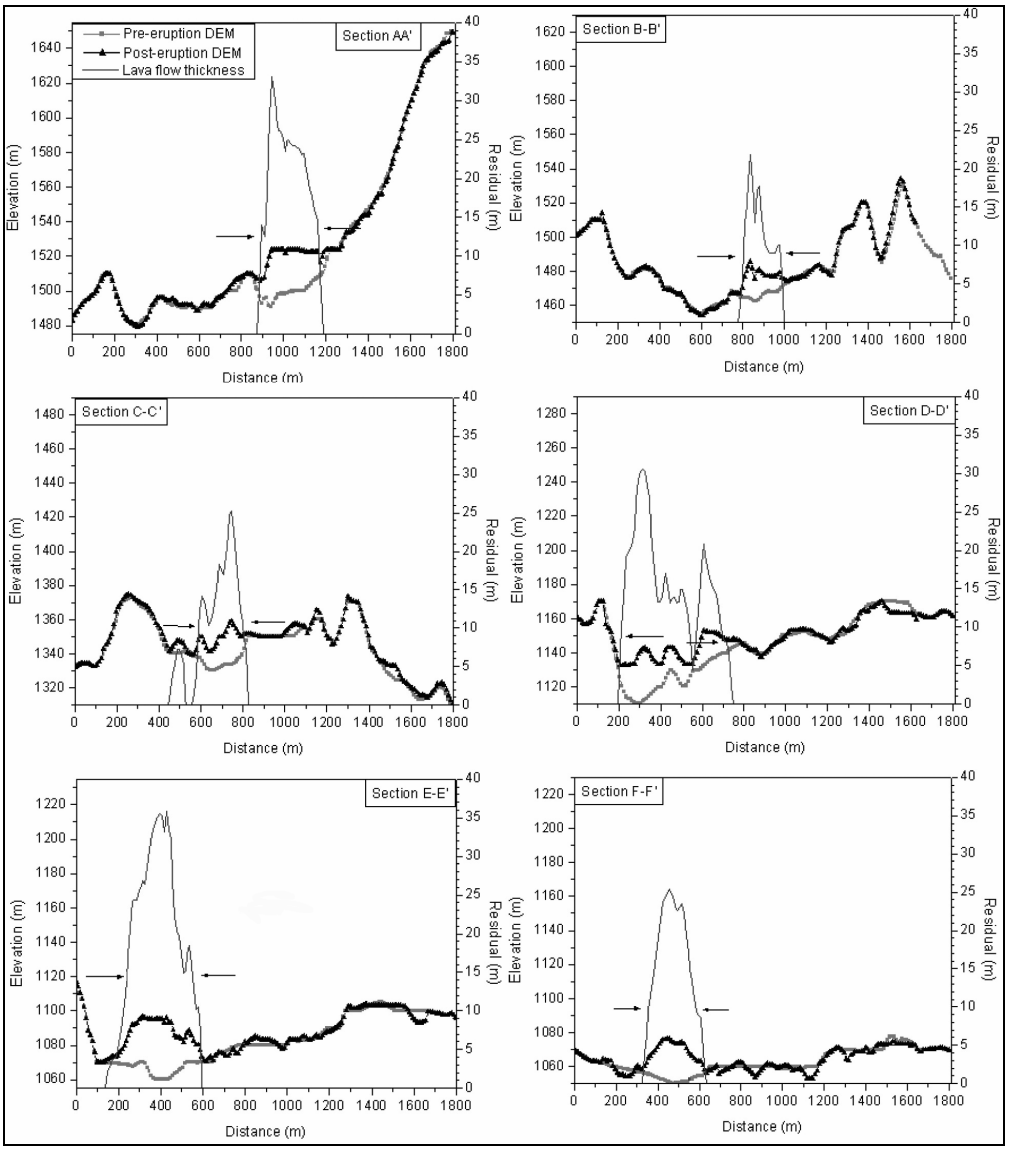

Figure 4.8: Selected cross sections across the LFS1 lava flow. See Figure 4.7 for locations. The left axes shows the elevation of the 1999 and 2001 DEMs, and the right axes shows the elevation differences between them, representing the lava flow thicknesses. Black arrows mark the thickness of the first emplacement phase; accumulation peaks above the black arrows belong to the second and third phases.

Considering that the lava flow undergone a continuous expansion between 18 and 26 July, the daily thicknesses, in every zone, were supposed to be equal to those observed at 26 July (Table 4.6). After 26 July the lava began to pile up on the older flow, thus the additional thickness values were simply added to those of 26 July. The seven zones

experienced very different emplacement histories (Table 4.6). Zone 6 was not active after 26 July and so underwent no additional thickness change. Zones 3 to 5 show a progressive decrease in additional deposition as a consequence of the active front regression. Zone 7 corresponds to the eastern branch of the flow that formed between 30 July and 6 August, and records only a single flow event. Finally, zone 1 did not experience additional emplacement until 9 August, when two lateral branches overflowed near the vent.

Daily volumes, evaluated in the seven zones, are shown in Table 4.7; the first five rows (cumulative volumes) correspond to the lava accumulated from the beginning of the eruption, while the last seven rows (additional volumes) quantify the lava added between two consecutive periods on the top of the older flow.

Date	Volume (10^6 m^3)							Total volume (10^6 m^3)
	Zone 1	Zone 2	Zone 3	Zone 4	Zone 5	Zone 6	Zone 7	
	Cumulative volumes (10^6 m^3)							
18/07/01	0.30	0.07	0.00	0.00	0.00	0.00	0.00	0.37
19/07/01	0. 30	0.84	0.56	0.00	0.00	0.00	0.00	1.70
20/07/01	0. 30	0.88	2.32	0.00	0.00	0.00	0.00	3.50
22/07/01	0. 30	0.88	3.60	1.30	2.08	0.42	0.00	8.58
26/07/01	0.33	0.95	4.30	1.40	3.38	4.62	0.00	14.98
	Additional volumes (10^6 m^3)							
28/07/01	0.00	0.09	1.23	0.45	0.24	0.00	0.00	2.01
30/07/01	0.00	0.18	0.71	0.21	0.24	0.00	0.03	1.37
02/08/01	0.00	0.15	0.36	0.15	0.72	0.00	0.09	1.47
04/08/01	0.00	0.00	0.21	0.08	0.00	0.00	0.51	0.80
06/08/01	0.00	0.00	0.21	0.08	0.00	0.00	0.30	0.59
07/08/01	0.00	0.00	0.11	0.00	0.00	0.00	0.00	0.11
09/08/01	0.08	0.00	0.00	0.00	0.00	0.00	0.00	0.08

Table 4.7: Daily volumes (active areas multiplied per evaluated thicknesses) of the seven zones composing the LFS1 flow. Volumes until 26 July 2001 are cumulative while subsequent volumes are partial. Last column shows the daily volumes of the whole flow.

In order to verify the correctness of the performed reconstruction, reconstructed versus DEM evaluated average thicknesses were compared in Table 4.8. Reconstructed thicknesses are those derived from the analysis of daily thicknesses and active areas. For each zone an average thickness was computed by dividing the final volume, derived from Table 4.7, by the corresponding area. These reconstructed thicknesses, as well as

the final volumes, are in a good agreement with those obtained from DEM comparison (observed thicknesses and volumes).

Values at 09 August 2001	Zone 1	Zone 2	Zone 3	Zone 4	Zone 5	Zone 6	Zone 7
Total area (10^6 m^2)	0.13	0.28	0.63	0.20	0.29	0.28	0.17
Observed volume (10^6 m^3)	0.38	1.49	7.25	2.26	4.62	4.46	0.95
Reconstructed volume (10^6 m^3)	0.40	1.36	7.11	2.37	4.63	4.54	0.97
Observed average thickness (m)	3.0	5.5	11.7	11.4	15.8	16.2	5.5
Reconstructed average thickness (m)	3.2	4.9	11.4	11.8	16.0	16.5	5.6

Table 4.8: Total area, measured from the 2001 DEM; observed volume measured from the comparison of the 1999 and the 2001 DEMs; reconstructed volume, evaluated from Table 4.7 by adding partial volumes after 26 July 2001 to the volumes at 26 July 2001; observed average thicknesses measured from the comparison of the 1999 and the 2001 DEMs; reconstructed average thickness evaluated by dividing the reconstructed volume by the total area. Every measure characterizes the LFS1 flow at the end of the eruption (9 August 2001) and it is evaluated inside the seven zones composing the LSF1 flow.

4.5.3 Effusion rate estimation

Finally the lava flow emplacement reconstruction was utilized to estimate the temporal evolution of the lava discharge from the LFS1 vent and to derive daily effusion rates, that is the average effusion rate during an observation period, obtained by dividing the emitted volume by the corresponding time interval.

Table 4.9 summarizes the main results of the analysis described above which allowed to compute daily effusion rate for the whole LFS1 flow. Figure 4.9 shows the temporal evolution of cumulative volumes and "daily effusion rate", as well as some instantaneous "effusion rate" measurements collected during the eruption by INGV staff which are in good agreement with our estimates. The daily effusion rate trend shows a rapid increase from an initial rate of 10 m^3/s to a peak value of about 30 m^3/s between 20 and 22 July 2001 (three days after the beginning). This was followed by slow decline over the next 16 days, leading to an effusion rate value lower than 1 m^3/s on 7 August.

Acquisition date and time	Eruption day	Acquisition time (s)	Cumulative volume (10^6 m^3)	Time span (s)	Partial volume (10^6 m^3)	Daily effusion rate (m^3/s)
18/07/2001, 03:00	0	0	0.00	0	0.00	0.00
18/07/2001, 13:00	1	36000	0.37	36000	0.37	10.28
19/07/2001, 16:00	2	133200	1.70	97200	1.33	13.68
20/07/2001, 13:00	3	208800	3.50	75600	1.80	23.81
22/07/2001, 11:00	5	374400	8.58	165600	5.08	30.68
26/07/2001, 12:00	9	723600	14.98	349200	6.40	18.33
28/07/2001, 16:00	11	910800	16.99	187200	2.01	10.74
30/07/2001, 11:00	13	1065600	18.35	154800	1.37	8.85
02/08/2001, 10:00	16	1321200	19.82	255600	1.47	5.75
04/08/2001, 07:00	18	1483200	20.62	162000	0.80	4.94
06/08/2001, 11:00	20	1670400	21.21	187200	0.59	3.15
07/08/2001, 07:00	21	1742400	21.32	72000	0.11	1.53
09/08/2001, 10:00	23	1926000	21.40	183600	0.08	0.44

Table 4.9: Partial and cumulative volumes of the whole LFS1 lava flow for each acquisition date. Partial volume is the volume emitted between two subsequent acquisition times (time span). Daily effusion rates were evaluated by dividing partial volumes by time spans.

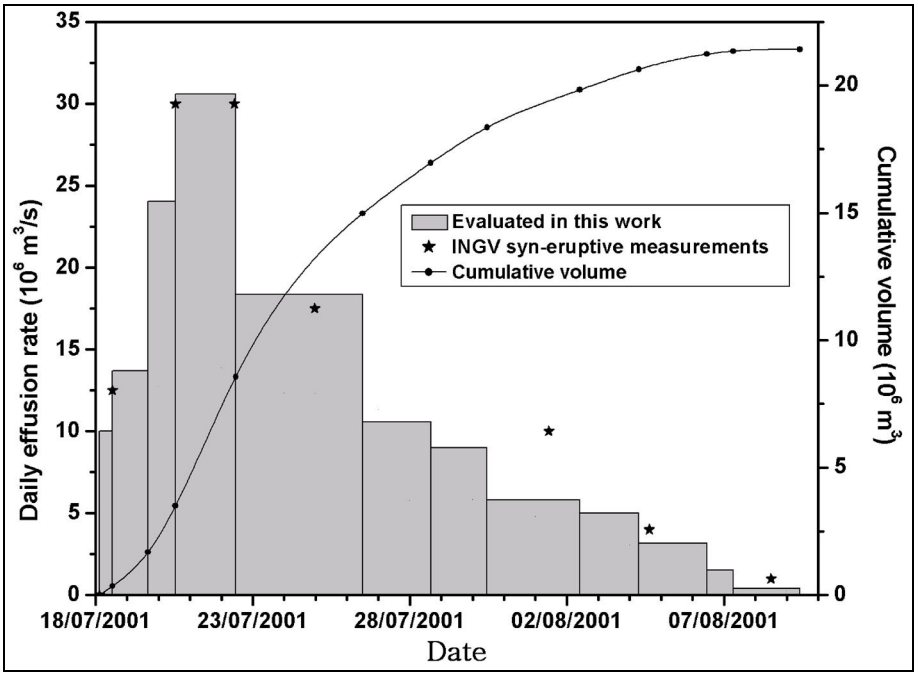

Figure 4.9: The left axes shows the temporal evolution of daily effusion rates evaluated in this work (gray bars), as well as field measurement of the instantaneous effusion rate (stars) made during the eruption by INGV staff. The right axis shows the cumulative volumes of the LFS1 lava flow evaluated in this work.

5. The LavaSIM simulation code applied to the 2001 Etna lava flow

5.1 The LavaSIM simulation code

LavaSIM is a three dimensional simulation code, able to describe the behavior of both liquid lava and crust. The lava flow is modeled as single-phase flow with solidification and the liquid part is assumed to be a Newtonian fluid [*Hidaka et al.*, 2005].

The analysis region (Figure 5.1) is represented by 3D cells placed above the topographic surface. The cells interested by the lava flow are distinguished in convection or free surface cells and they are treated separately. A convection cell is full of liquid lava or crust while a free surface cell is partially filled and it is located at the ground surface, at the lava top and at any place under the crust.

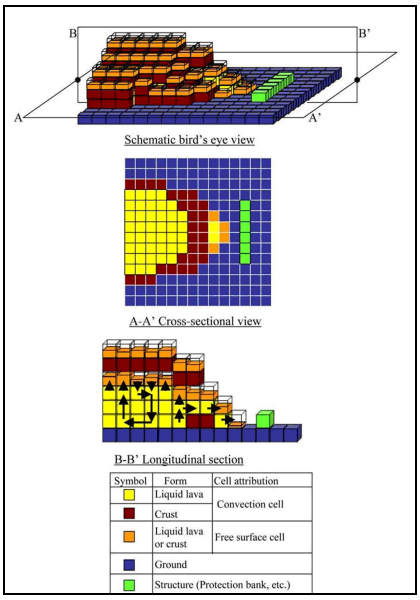

Figure 5.1: schematic description of the analysis region [after *Hidaka et al.*, 2005]

Lava flow is evaluated from the Navier-Stokes equations with the terms of inertia, pressure, pressure derived from lava level (liquid head), ground inclination and elevation.

The heat transfer between liquid lava and: ground, air, water and crust is evaluated from the energy conservation equation.

Two types of flow stop conditions are considered: one is related to a minimum lava flow thickness and one to the lava solidification, a solidified cell can move only in the z direction.

5.1.1 Lava physical properties

LavaSIM considers four lava physical properties: density, enthalpy, thermal conductivity and viscosity.

Density

In LavaSIM density is fixed on the basis of literature data. Lava density varies with increasing silica content and temperature. However changes with temperature remain within 10% and may not be noticeable when compared with the effect of bubbles and cracks in lava flows, for which it is not possible to predict their volume fraction.

Viscosity

Viscosity is the most variable between the four parameters, it changes by several orders of magnitude whit composition at constant temperature, and ten or more orders of magnitude with temperature at constant composition. In LavaSIM viscosity can be set as constant or evaluated from the equation [*Goto et al.*, 1997]:

$$\log \mu = \log \mu_{Tg} - \frac{A(T - T_g)}{B + T - T_g} \tag{5.1}$$

where μ_{Tg} is the viscosity (in Pa s) at the glass transition temperature (T_g), T is the absolute temperature, A and B are constant whose compositional dependency was experimentally determined by *Goto et al.* [1997]:

$$\log \mu_{Tg} = 13.0,\ A = 17.5,\ B = 64S^2 - 202S + 446,\ T_g = 57S^2 - 306S + 1341 \tag{5.2}$$

where S is the parameters defined by *Shaw* [1972] and it depends on the lava chemical composition without taking into account water content.

If an empirical equation is available for a specific volcano it is better to apply it for more accurate evaluation of viscosity.

Two viscosity models are available for Etna lava, one for hydrous [*Giordano and Dingwell*, 2003a] and one for anhydrous [*Giordano and Dingwell*, 2003b] lavas. The hydrous viscosity was parameterized in terms of temperature and water content on the

basis of the fitting with experimental data utilizing a 1992 Etna lava sample. The anhydrous viscosity was parameterized in terms of temperature and chemical composition. Chemical composition is described by the "network modifier" parameter that is sum of the molar oxide of Na, K, Ca, Mg, Mn and Fe. Samples from various lava flow eruption, among which the 1992 Etna, were utilized to derive the law. The temperature range to be considered is 700 - 1600°C because only a few dataset were available outside this interval.

Figure 5.2 compares the two Etna viscosity models with *Goto et al.* [1997] model. Anhydrous and Goto's viscosities were evaluated considering the chemical composition of the 2001 Etna lava [*Taddeucci et al.*, 2004]. Figure 5.2 shows that *Goto et al.* [1997] model gives viscosity values about one order lower than those obtained from *Giordano and Dingwell* [2003b] and a little higher then those obtained from *Giordano and Dingwell* [2003a] model with low (0,02%) water content.

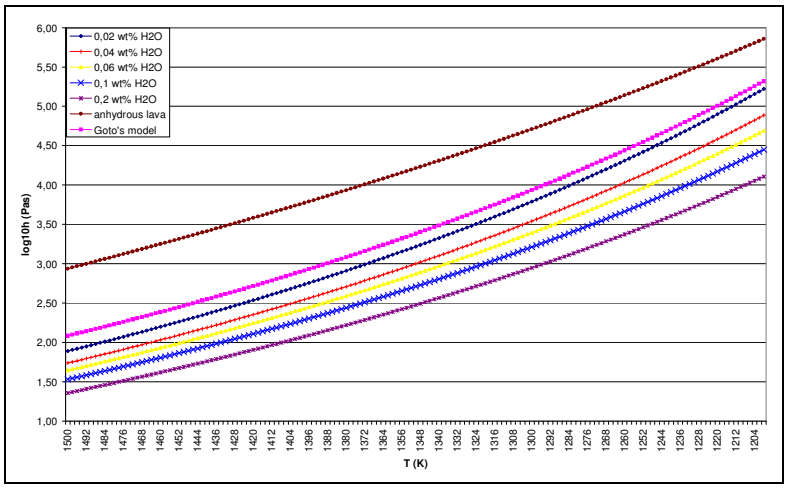

Figure 5.2: Comparison between the Etna viscosity models for hydrous lavas, with different water contents [Giordano and Dingwell, 2003a] and for anhydrous lavas [Giordano and Dingwell, 2003b] and Goto et al. [1997] model.

Specific enthalpy

Specific enthalpy, below the solidus and above the liquidus temperatures, is given as the product of specific heat and temperature, while the latent heat of crystallization is taken into account between the solidus and liquidus temperatures. Two different relations (Figure 5.3) are implemented in the code, their selection is related to the use of a

constant or temperature-depending viscosity. Figure 5.3 reports also the same law (not implemented in the code) evaluated by using literature values for Etna lavas.

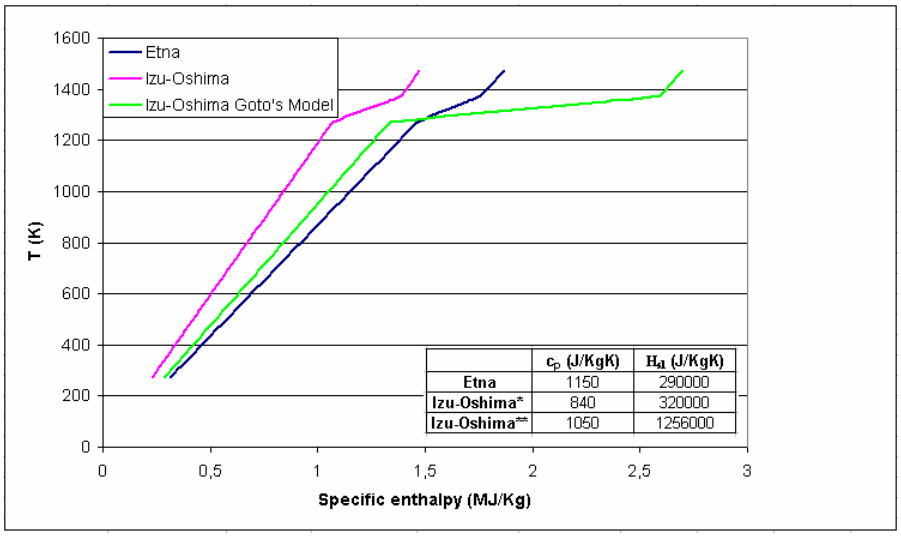

Figure 5.3: relation between specific enthalpy and temperature. Specific heat (C_P) and latent heat of crystallization (Hsl) are set from literature *values for simulations with constant viscosity, **values for simulations with Goto's viscosity model.

Thermal conductivity

The behavior of thermal conductivity with temperature differs among samples, but when the samples are restricted to basalt and andesite, their trends is similar. LavaSIM adopts two empirical parabolic equations to give thermal conductivity without considering compositional dependency:

$$\lambda = \begin{cases} 1.15 + 5.9 \cdot 10^{-7} (T - 1200)^2 & T < 1200°C \\ 1.15 + 9.7 \cdot 10^{-6} (T - 1200)^2 & T > 1200°C \end{cases} \quad (5.3)$$

5.1.2 Code structure

The code starts by inputting lava properties, pre-eruption topography and boundary conditions for lava extrusion and atmosphere. The analytical results (three-dimensional distributions of cell state, lava temperature and velocity and two-dimensional distribution of lava thickness) are written to output files at times defined in the input data.

Figure 5.4 reports the main processes of the LavaSIM code, they can be described as:

- Lava emission from the cells, set as vents, and evaluation of lava mass and enthalpy inside these cells;
- Evaluation of the minimum thickness related to: a constant value, based on observation at the specific volcano, and to a constant yield strength, based on the equation [*Hulme*, 1974]:

$$H_t = \frac{S_y}{\rho g \sin\theta} \tag{5.4}$$

where H_t is the lava thickness, S_y is the yield strength (fixed in the input parameters), ρ is the density and θ is the ground slope;

- Flow analysis and evaluation of the inflow and outflow at the boundary between convection and free surface cells:
  - Assignment of an approximate velocity;
  - Evaluation of the pressure distribution from the mass conservation equation and the approximate velocity;
  - Evaluation of the true velocity from the Navier-Stokes equation, the pressure distribution and the approximate velocity;

$$\frac{d\vec{V}}{dt} = \frac{1}{\rho}\left[-\nabla P + \sum_i \frac{\partial}{\partial x_i}\left(\mu \frac{\partial \vec{V}}{\partial x_i}\right)\right] - \vec{G} + \vec{K} \tag{5.5}$$

  where $\vec{V} = (u, v, w)$ is the flow velocity, μ and ρ are the lava viscosity and density, P is the pressure, $\vec{G} = \left(g\sin^2\theta\cos^2\phi\frac{\partial H}{\partial x}, g\sin^2\theta\sin^2\phi\frac{\partial H}{\partial y}, g\cos^2\theta\frac{\partial H}{\partial z}\right)$ with H sum of liquid head and ground elevation, θ ground inclination angle and ϕ azimuthal direction of the maximum ground inclination and $\vec{K} = (0,0,K)$ is the external force of Boussinesq's approximation which simulates the buoyancy.
- Heat transfer calculation:
  - Evaluation of the heat fluxes, due to convection and radiation, at the interface between liquid lava and: crust, atmospheric fluids (air and water), structure and ground;

– Evaluation of the enthalpy decrease from the energy conservation equation with: the true velocity, the heat fluxes and the enthalpy and temperature values at the previous time step;

– Evaluation of the cell temperature from the enthalpy-temperature relation (Figure 5.3);

- Evaluation of mass and enthalpy (h) inside every cell and resetting of cell attribution (convection or free surface cells) on the basis of the lava volume;
- Evaluation of the solidification fraction (b) inside every cell:

$$b = \begin{cases} 1 & h \le h_s \\ \dfrac{h_l - h}{h_{sl}} & h_s < h < h_l \\ 0 & h > h_l \end{cases} \qquad (5.6)$$

where h_s and h_l are the specific enthalpies at the solidifying and at the melting points respectively and h_{sl} is the latent heat;

- Resetting of lava state (liquid or crust) on the base of the b value: a cell is considered solid when its b value is higher than the solidification fraction of the liquidity loss (set in the input parameters).

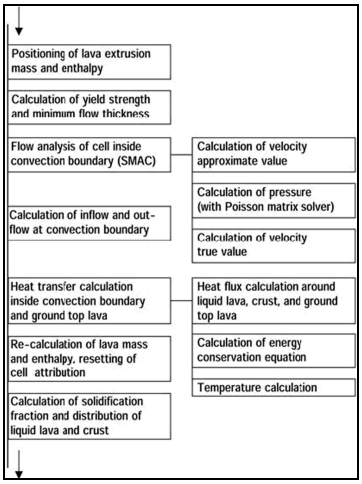

Figure 5.4: Primary analytical processes in LavaSIM [after Hidaka et al., 2005].

5.1.3 Heat transfer

LavaSIM evaluates the heat flux at liquid-solid, atmospheric fluid (air or water) and ground surface interfaces (Table 5.1) using a general heat transfer correlation or thermal conductivity equation (5.7).

	liquid lava	crust	structure
liquid lava	transport	natural convection	natural convection
	thermal conductivity		
crust	natural convection	thermal conductivity	thermal conductivity
structure	natural convection	thermal conductivity	thermal conductivity
ground	natural convection	thermal conductivity	thermal conductivity
atmospheric fluid	natural convection	natural convection	natural convection
	radiation	radiation	radiation

Table 5.1: Heat transfer models between lava, structure ground and atmospheric fluid.

Heat transfer models between lava and atmospheric fluid, lava and ground, lava and structures, liquid lava and crust are shown in Figure 5.5a and evaluated by means of empirical relations. Simplified correlations for ideal conditions, such as the thermal radiation and natural convection of a flat plane, are used in the heat transfer models, although they may possibly underestimate the heat transfer rate.

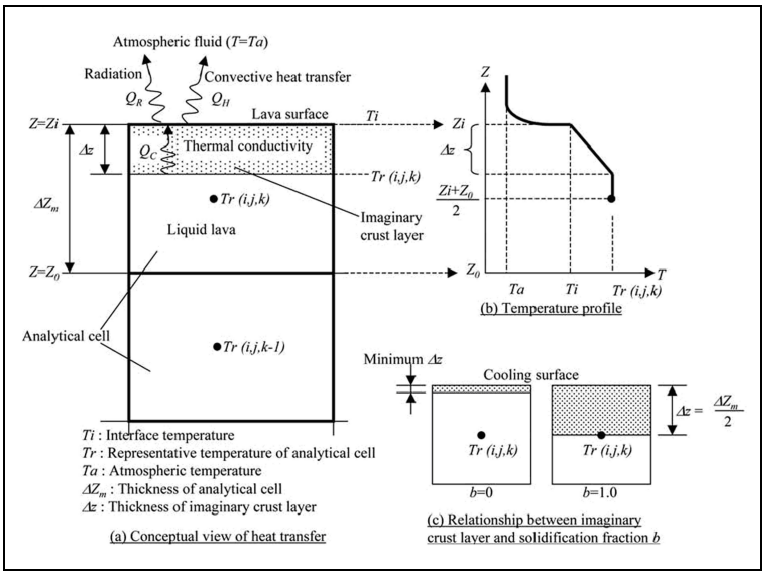

Figure 5.5: a) conceptual view of heat transfer between lava and atmospheric fluid. b) Surface temperature decreasing and formation of an imaginary crust layer simulating the surface cooling [after Hidaka et al., 2005].

Thermal conductivity between solids (crust-crust, crust-structure), energy transport and thermal conductivity between liquid lava are calculated in the energy conservation equation:

$$\frac{\partial h}{\partial t}+u\frac{\delta h}{\delta x}+v\frac{\partial h}{\partial y}+w\frac{\partial h}{\partial z}=\frac{1}{\rho}\left[\frac{\partial}{\partial x}\left(\lambda\frac{\partial T}{\partial x}\right)+\frac{\partial}{\partial y}\left(\lambda\frac{\partial T}{\partial y}\right)+\frac{\partial}{\partial z}\left(\lambda\frac{\partial T}{\partial z}\right)\right]+Q \qquad (5.7)$$

where h is the specific enthalpy, λ is the thermal conductivity and Q is the heat transfer due to cooling at the upper surface, at the ground, and between solid and liquid lava.

The cells are considered filled by isothermal lava with the exception of those located at the interface between lava and atmospheric fluid. Such cells are supposed partially filled by an imaginary crust layer, representative of the real surface cooling, corresponding to a local transient region with a temperature gradient. The imaginary crust layer grows from the cooling surface and its thickness Δz is proportional to the solidification fraction b and to the cell thickness Δz_m:

$$\Delta z = 0{,}5b\Delta z_m \qquad (5.8)$$

A minimum thickness of the imaginary crust layer is given when the solidification fraction b is equal to zero, that is when the lava temperature is at the melting point or higher (Figure 5.5b). Moreover the imaginary crust layer is characterized by a temperature linearly decreasing from T_r (representative temperature of the cell) to T_i (interface temperature) (Figure 5.5b). The interface temperature T_i is obtained from heat balance in which the heat flux of thermal conductivity Q_c, from a wall with temperature T_r, is equal to the sum of the radiation heat flux Q_R and heat flux of convective heat transfer Q_H, evaluated by an iterative calculation:

$$Q_c = Q_R + Q_H \qquad (5.9)$$

Natural convection heat transfer is evaluated by using five different empirical correlations for uniform wall temperature relating the Nusselt and the Rayleight numbers:

- Two [*Fujii and Imura*, 1972] for a horizontal wall with upward heating or downward cooling (i.e. the flow base)

$$Nu = \begin{cases} 0.54Ra^{0.25} & 2.0 \cdot 10^4 < Ra < 8.0 \cdot 10^6 \\ 0.15Ra^{1/3} & 8.0 \cdot 10^6 < Ra < 1.0 \cdot 10^{11} \end{cases} \quad (5.10)$$

- One [*Fujii and Imura*, 1972] for a horizontal wall with upward cooling or downward heating (i.e. the flow top)

$$Nu = 0.58Ra^{0.2} \quad 1.0 \cdot 10^5 < Ra < 1.0 \cdot 10^{11} \quad (5.11)$$

- Two [*McAdams*, 1954; *Bayley*, 1955) for a vertical wall (i.e. the flow levees and front)

$$Nu = \begin{cases} 0.59Ra^{0.25} & 1.0 \cdot 10^4 < Ra < 1.0 \cdot 10^9 \\ 0.10Ra^{1/3} & 1.0 \cdot 10^9 < Ra < 1.0 \cdot 10^{13} \end{cases} \quad (5.12)$$

The forced convection due to the effect of wind on lava is not considered in the model.

Heat flux by radiation, from lava and structures to the atmospheric fluid, is evaluated by means of a simplified equation, neglecting the radiation shape factor, for a wall located at infinity having the same temperature as the atmospheric fluid:

$$Q_R = \sigma\varepsilon(T_i^4 - T_a^4) \quad (5.13)$$

where σ is the Stefan-Boltzmann constant, ε is the lava emissivity and T_a is the ambient temperature.

5.2 Simulation of the emplacement of an Etna lava flow

The LavaSIM code was applied to simulate the 2001 Etna lava flow emitted from the 2100 m a.s.l. vent, previously named LFS1flow [*Coltelli et al.*, 2007], whose temporal evolution and effusion rate trend has been described in paragraph 4.4.

This work shows, in particular, the quantitative comparison between the simulated and observed 2D lava distribution and the 3D distribution of liquid lava and crust. Though LavaSIM is a 3D simulation code, the comparison between simulated and observed flow geometries was limited to the planimetric lava distribution because information about daily thicknesses were available only for their mean values, while final thicknesses (at 9 August 2001) can be assessed for the whole flow.

The availability of a time series of flow field emplacement maps (Figure 4.6) allowed to check LavaSIM performance not only at the end of the flow emplacement but also, step by step, during its temporal evolution.

5.2.1 Summary of the performed simulation

Different test cases (Table 5.4, end of the chapter) were carried out in order to evaluate the influence, on the lava distribution and cooling, of the input parameters (viscosity, solidification fraction of liquidity loss, eruptive enthalpy and lava emissivity). A simulation (Test E115) with a constant lava discharge, equal to the average effusion rate (i.e. the total volume divided by the eruption duration), was also carried out in order to check the influence, on the flow spreading and cooling, of the lava feeding.

As regard to the viscosity the tests can be divided in two groups:

- Low viscosity (Test C1, C2, C4)
- High viscosity (Test F2, F3, V3, V4, V111, V112, V114, V125, B115, B116, E115 and EP114).

The utilized constant values were evaluated by using viscosity models for Etna lavas (Figure 5.2): low values were derived from the *Giordano and Dingwell* [2003 a] model for hydrous lavas (0.02 and 0.06 wt% of water), while high values are related to the *Giordano and Dingwell* [2003 b] model for anhydrous lavas. Test C4, utilizing the viscosity law of *Goto et al.* [1997] (Figure 5.2) implemented in LavaSIM, and having a viscosity of about 2200 Pa s at the eruption temperature, was included in the low viscosity cases.

The solidification fraction of liquidity loss, depending on the specific enthalpy [*Hidaka et al.*, 2005], ranged between 0.5 and 1, corresponding to a solidification temperature of 1323 and 1273 K respectively.

The eruptive enthalpy, product of specific heat and temperature [*Hidaka et al.*, 2005], ranged between 1.23 and 1.33 MJ/Kg for simulations with constant viscosities, the highest value matches the eruptive temperature of 1355 K evaluated for the 2001 eruption [*Taddeucci et al.*, 2004]. Test C4, utilizing a different enthalpy law, had an eruptive enthalpy of 2.34 MJ/Kg corresponding to the same eruptive temperature.

Lava emissivity, set from literature values [*Dragoni*, 1988; *Crisp et al.*, 1990], ranged between 0.7 and 0.95.

Pre-eruption surface was represented by the slope, aspect and elevation of the 1999 DEM (paragraph 4.4). The planimetric cell size was as high as 25 m in order to reduce the computation time and the z cell dimension was 1 m. The study area was represented by 80 X 180 X 20 cells, covering an area of 2 X 8 Km, while the height of the simulation space is 20 m.

The comparison between observed and simulated flows was performed until 208800 s (20 July), or a little further, for all the simulations. Test E115, which lasted until 446400 s (23 July), was compared with the real flow until 22 July.

Tests C1, C2, C4, B115, V3 and V111 were stopped (at times corresponding to the 20 or 21 July) because the simulated flows were longer than the final observed flow. Tests F2, V125, B115, B116 and EP114 were stopped because they were longer than the real flow at the 20 July and they were approaching the final flow length. Tests V112 and V114 were stopped (at times corresponding to the 20 July) because mass and energy were not conserved after 208800 s, owing to a too strong solidification at the lava flow top causing a thickness increase up to 20 m (height of the simulation space). Finally Test E115 was stopped (at times corresponding to the 23 July) because its front was no further moving and it was much thicker than the final flow in the same area.

5.2.2 Analyses of the temporal evolution of the lava flow spreading and cooling

Lava spreading was analysed by comparing the planimetric expansion of real and simulated flows, permitting to directly check their correspondence and to evaluate the underestimated, overlapping and overestimated areas. Figure 5.6 shows an example of the qualitative planimetric comparison (test V112), Figure 5.7 quantifies this comparison as well as that between simulated and observed length, while Figure 5.8 shows the matching between simulated and observed areas for all the tests.

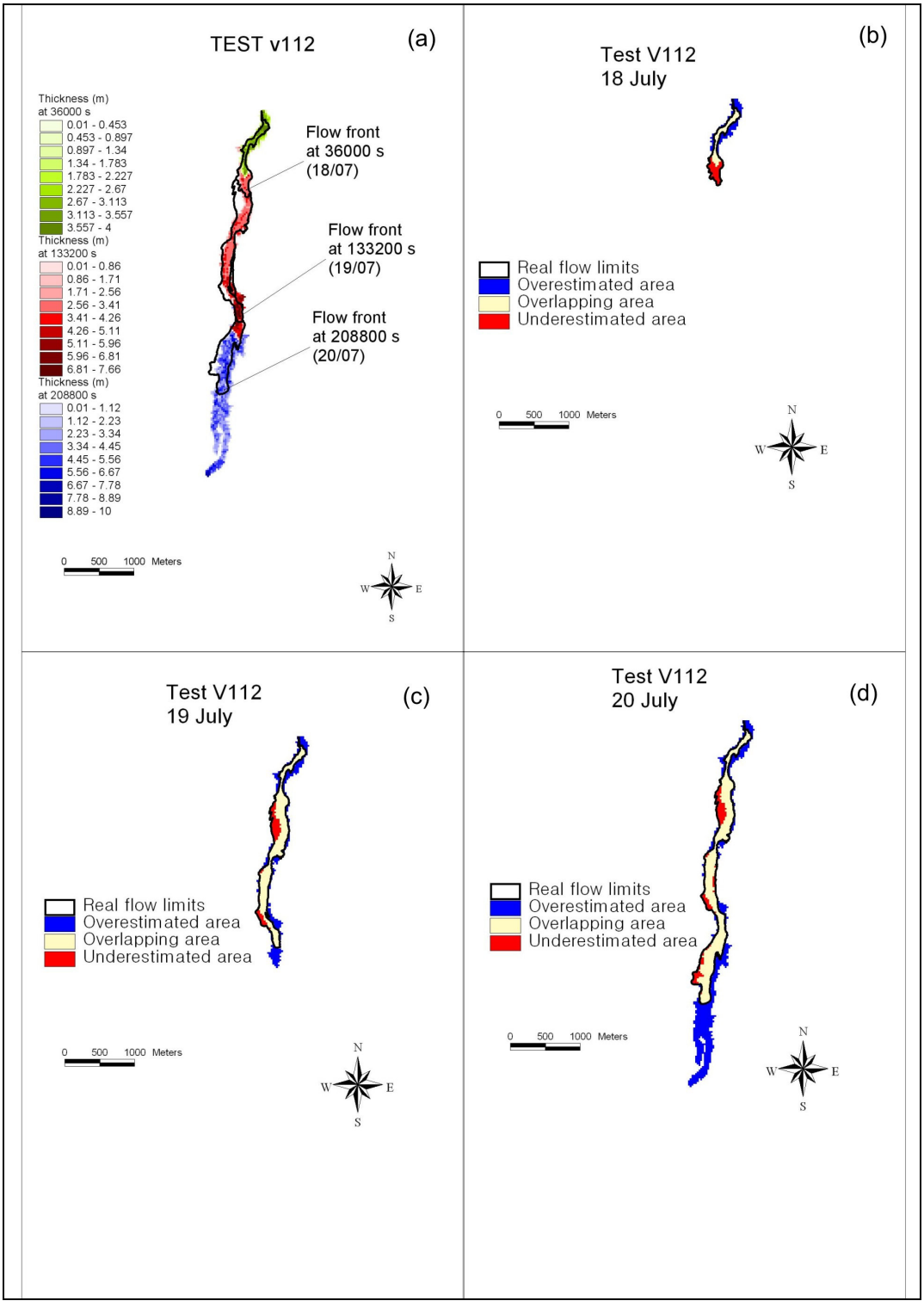

Figure 5.6: (a) Test V112 temporal evolution, black lines are the observed flow limits. Differences between observed and simulated (Test V112) lava flow area at: (b) 18 July; (c) 19 July; (d) 20 July. In red underestimated area, in yellow overlapping area, in blue overestimated area.

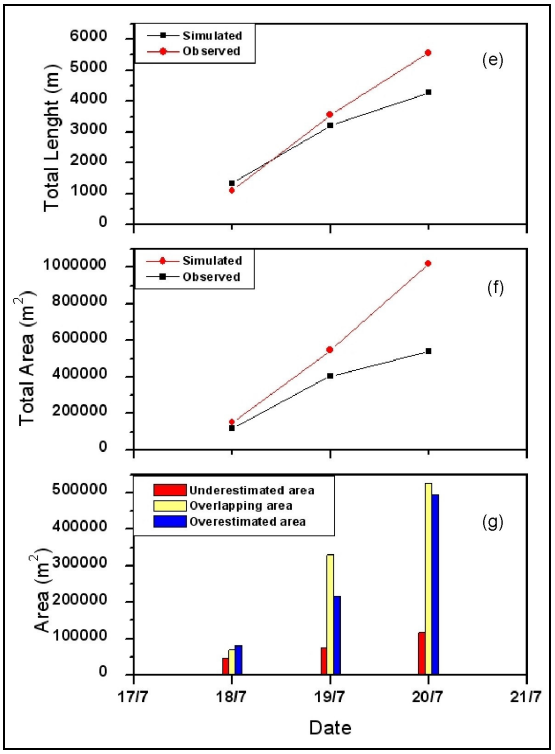

Figure 5.7: Quantitative comparison between simulated (Test V112) and observed flow geometry at the three selected dates: (e) length computed along the flow direction; (f) total area; (g) differences between lava spreading.

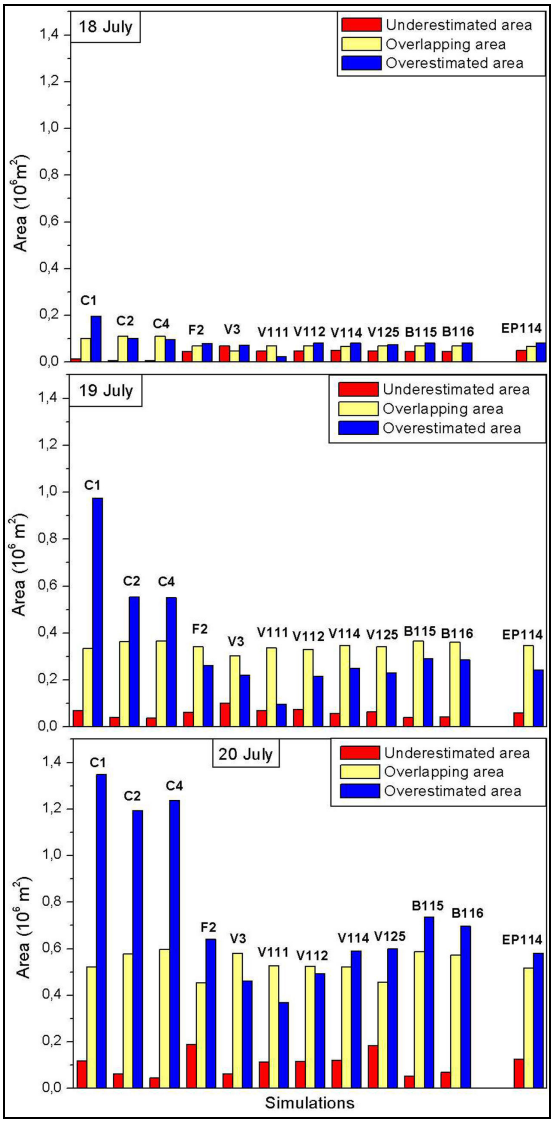

Figure 5.8: histogram of underestimated, overlapping and overestimated area at 18, 19 and 20 July for all the tests.

The matching between simulated and observed areas can be quantified by the fitness function e_1 [*Spataro et al.*, 2004] defined as:

$$e_1 = \sqrt{\frac{m(R \cap S)}{m(R \cup S)}} \tag{5.14}$$

were m(A) denotes the measure of the region A, while R and S are the areas affected by the real (observed) and simulated event. $R \cup S$ is, here, the sum of underestimated, overlapping and overestimated areas while $R \cap S$ is the overlapping area.

The fitness function, evaluated at every simulated date, is reported in Table 5.2; this function wasn't evaluated for test E115 because its daily volumes are lower than the corresponding observed volumes. As a matter of fact this test was not based on the effusion rate trend defined in Table 4.9 and figure 4.9 but the lava emission was kept constant (equal to the average effusion rate) during the whole simulation. Consequently, it is not possible to compare the simulated and observed emplacement histories.

Simulations	**Fitness function (e_1)**		
	18 July	**19 July**	**20 July**
Test C1	0.57	0.49	0.51
Test C2	0.71	0.62	0.56
Test C4	0.72	0.62	0.56
Test V3	0.50	0.70	0.72
Test F2	0.60	0.72	0.59
Test V111	0.70	0.82	0.72
Test V112	0.59	0.73	0.68
Test V114	0.58	0.73	0.65
Test V125	0.60	0.73	0.71
Test B115	0.60	0.72	0.65
Test B116	0.60	0.72	0.65
Test EP114	0.58	0.73	0.65

Table 5.2: fitness function for all the simulations but Test E115

Flow length, and particularly the Percent Length Ratio ($PLR=L_{simulated}/L_{observed}*100$), was considered the most useful control factor for evaluating the reliability of the different tests. The histogram of Figure 5.9 reports the PLR values attained by the 13 tests at times corresponding to the surveying dates while Figure 5.10 - Figure 5.13

report (separately for the 18, 19 and 20 July) PLR as a function of viscosity, solidification fraction of liquidity loss, eruptive enthalpy and lava emissivity.

Lava cooling was analyzed by studying the 3D liquid lava and crust distribution, here reported only for two tests, V112 and E115 (Figure 5.14 - Figure 5.18 and Figure 5.19 - Figure 5.24, respectively) in order to highlight the influence of the lava feeding on the flow cooling. Test E115, having a constant effusion rate, is compared with a simulation (V112) having similar input parameters (Table 5.4). The 3D flows were divided in overlapped layers: the first corresponding to the cells directly above the topographic surface, while the last corresponding to the highest cells filled by lava. It is important to note that only significant layers (i.e. those containing more than two filled cells) were represented.

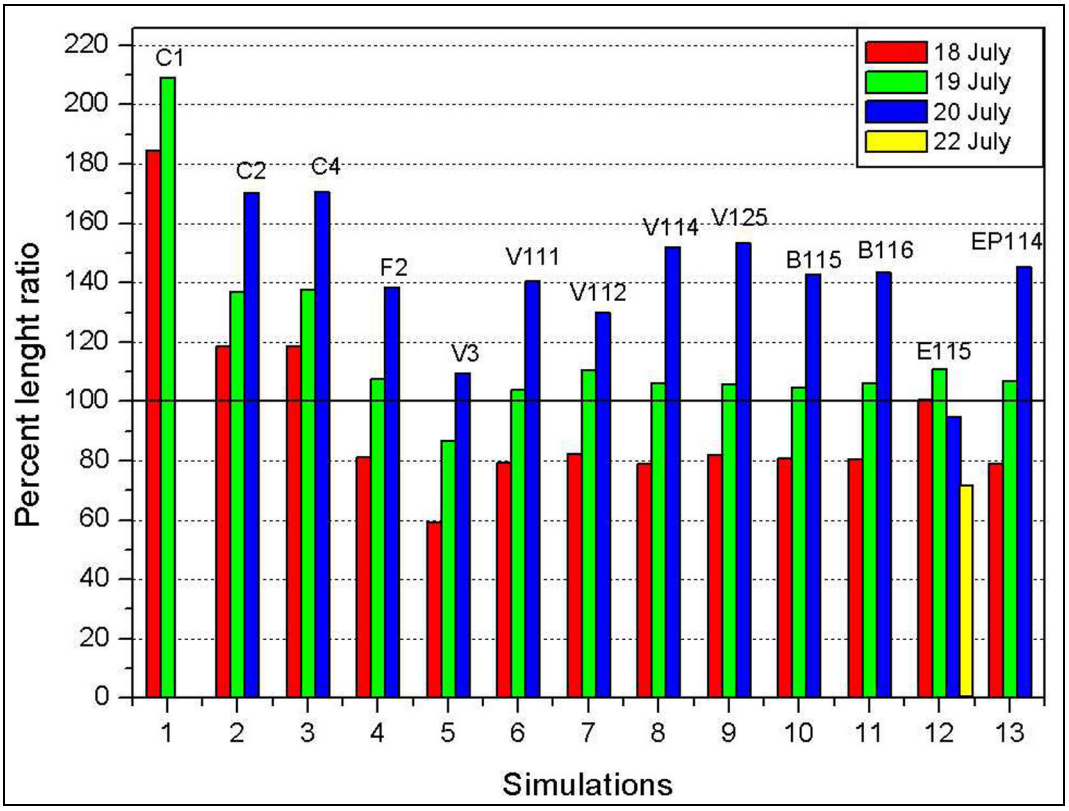

Figure 5.9: histogram of the Percent Length Ratio (Lsimulated/Lreal*100) at 18, 19 and 20 July for all the carried out tests.

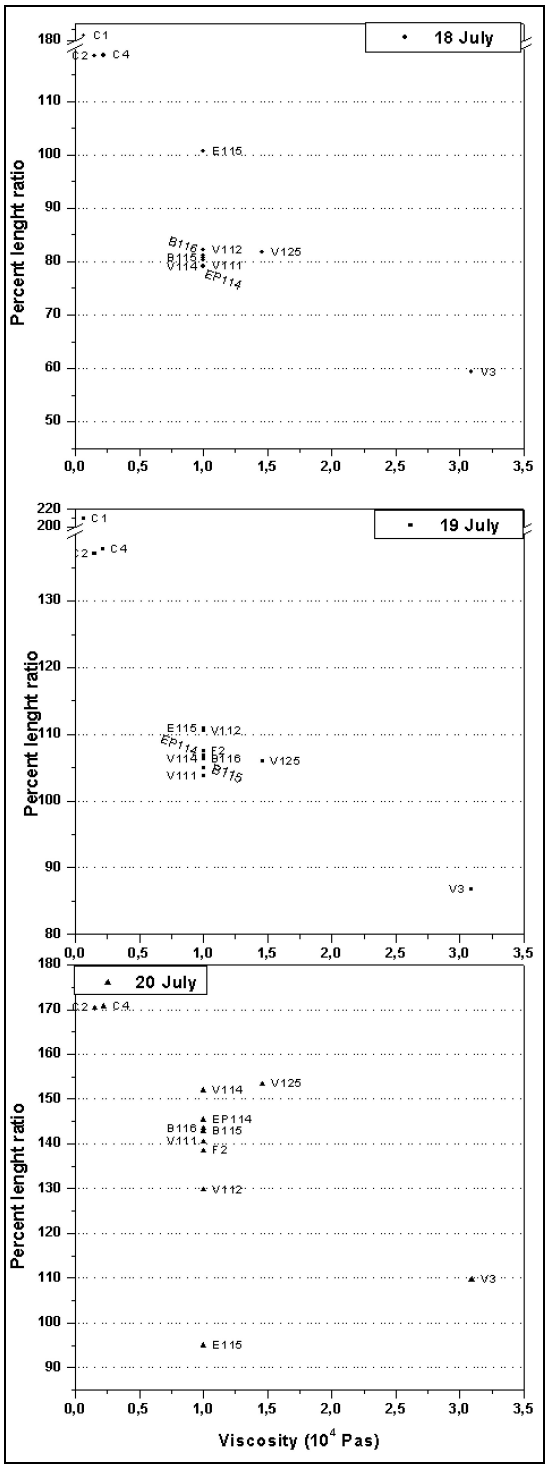

Figure 5.10: Percent Length Ratio (Lsimulated/Lreal*100) at 18, 19 and 20 July for all the tests as function of the viscosity.

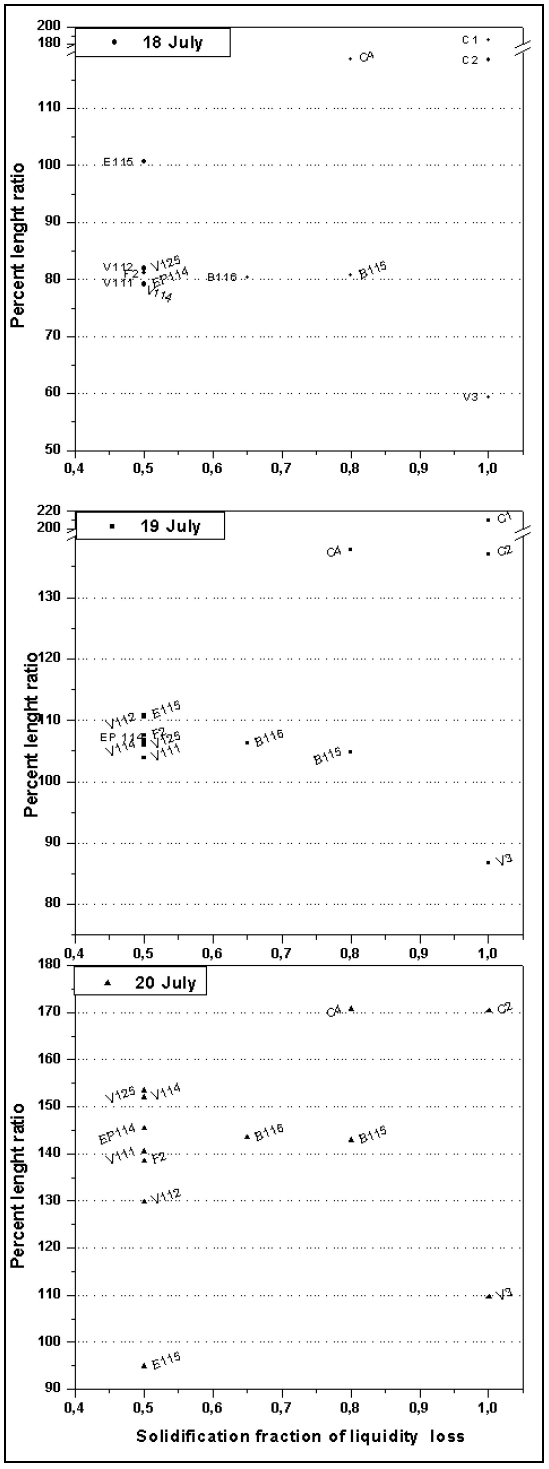

Figure 5.11: Percent Length Ratio (Lsimulated/Lreal*100) at 18, 19 and 20 July for all the tests as function of the solidification fraction of liquidity loss.

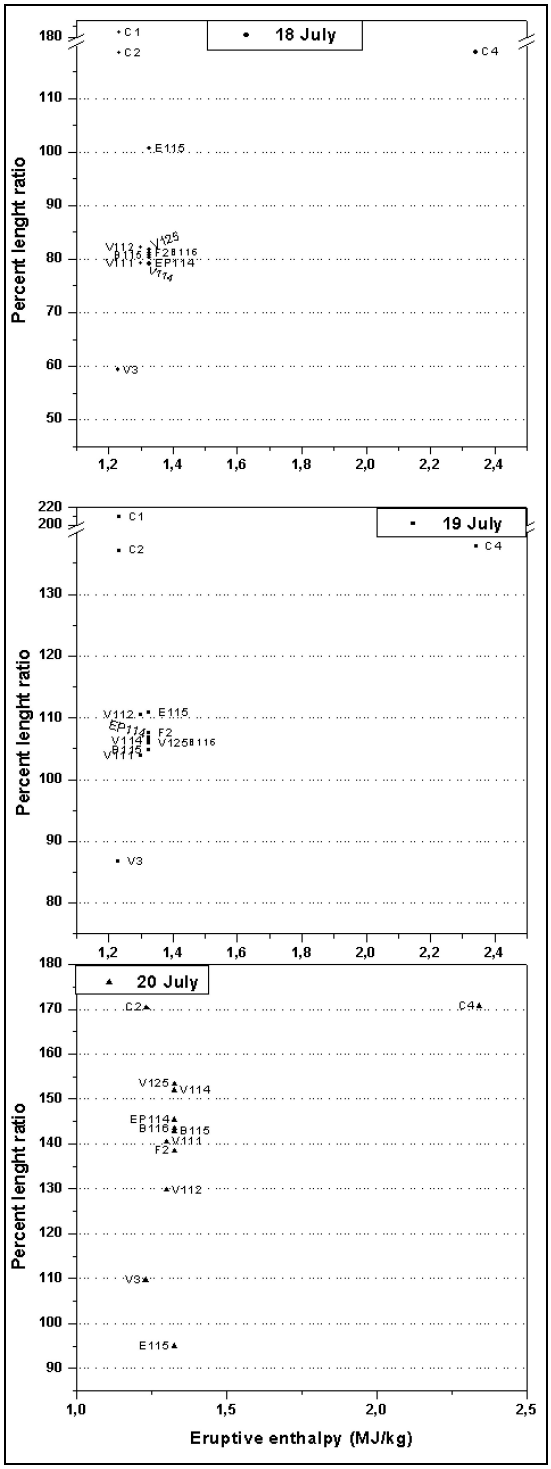

Figure 5.12: Percent Length Ratio (Lsimulated/Lreal*100) at 18, 19 and 20 July for all the tests as function of the eruptive enthalpy.

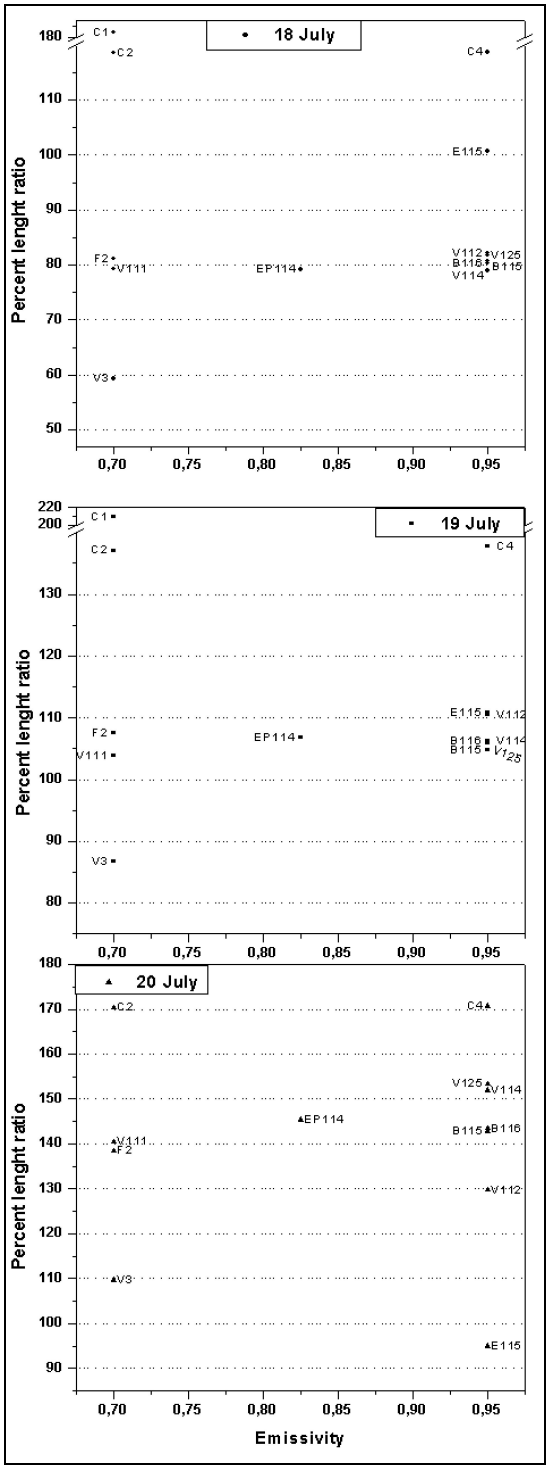

Figure 5.13: Percent Length Ratio (Lsimulated/Lreal*100) at 18, 19 and 20 July for all the tests as function of the lava emissivity.

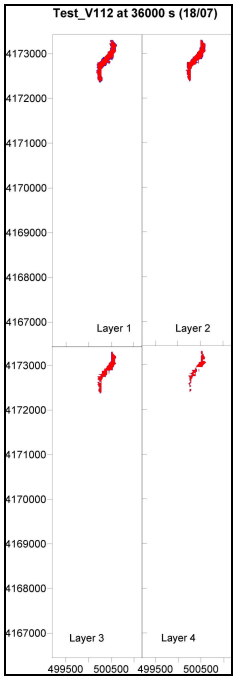

Figure 5.14: Liquid lava/crust distribution for test V112 at 36000 s (18/07); liquid lava is represented in red while crust is in blue.

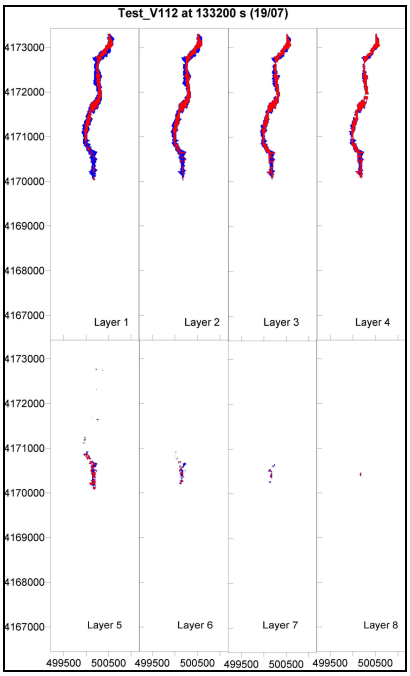

Figure 5.15: Liquid lava/crust distribution for test V112 at 133200 s (19/07); liquid lava is represented in red while crust is in blue.

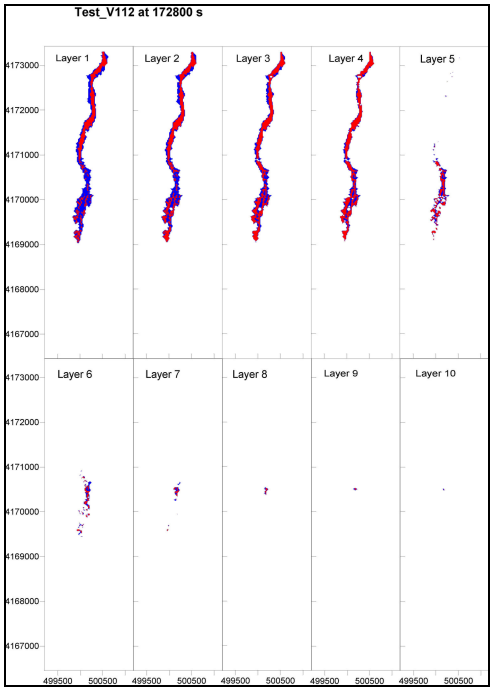

Figure 5.16: Liquid lava/crust distribution for test V112 at 172800 s; liquid lava is represented in red while crust is in blue.

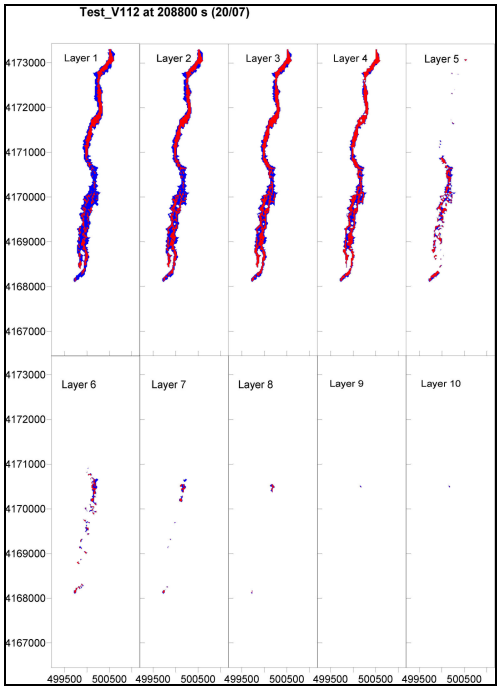

Figure 5.17: Liquid lava/crust distribution for test V112 at 208800 s (20/07); liquid lava is represented in red while crust is in blue.

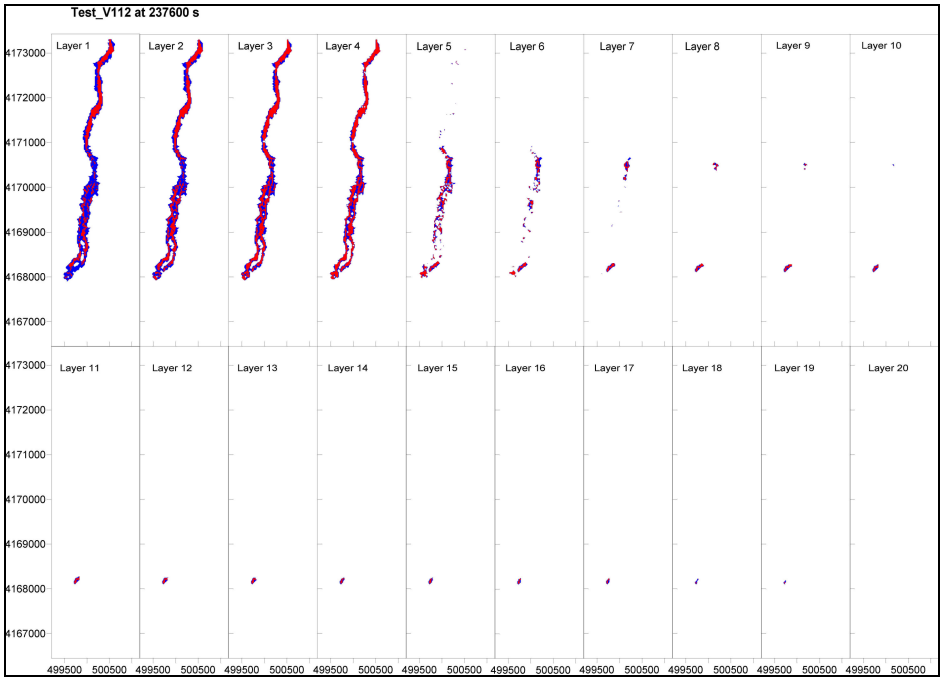

Figure 5.18: Liquid lava/crust distribution for test V112 at 237600 s (simulation end); liquid lava is represented in red while crust is in blue

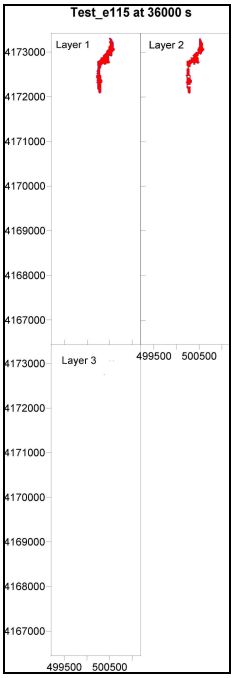

Figure 5.19: Liquid lava/crust distribution for test E115 at 36000 s (18/07); liquid lava is represented in red while crust is in blue.

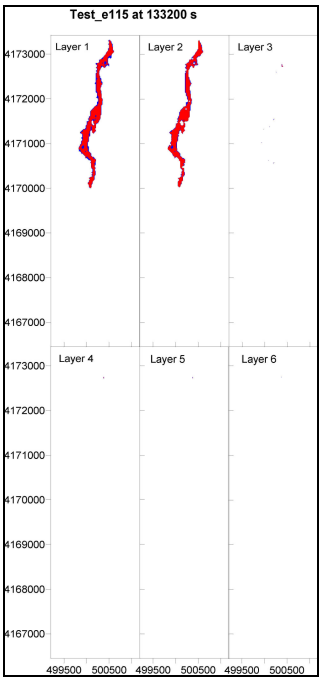

Figure 5.20: Liquid lava/crust distribution for test E115 at 133200 s (19/07); liquid lava is represented in red while crust is in blue.

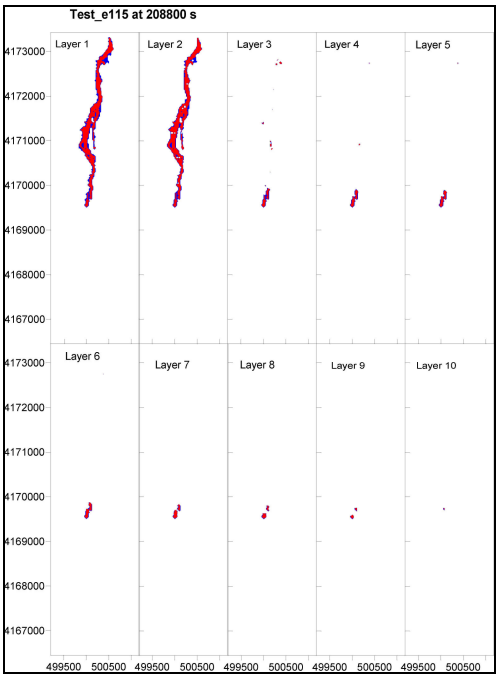

Figure 5.21: Liquid lava/crust distribution for test E115 at 208800 s (20/07); liquid lava is represented in red while crust is in blue.

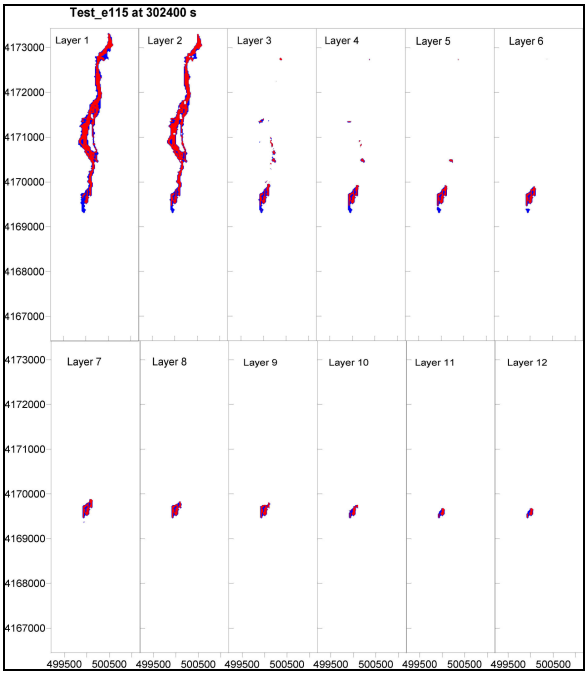

Figure 5.22: Liquid lava/crust distribution for test E115 at 302400 s; liquid lava is represented in red while crust is in blue.

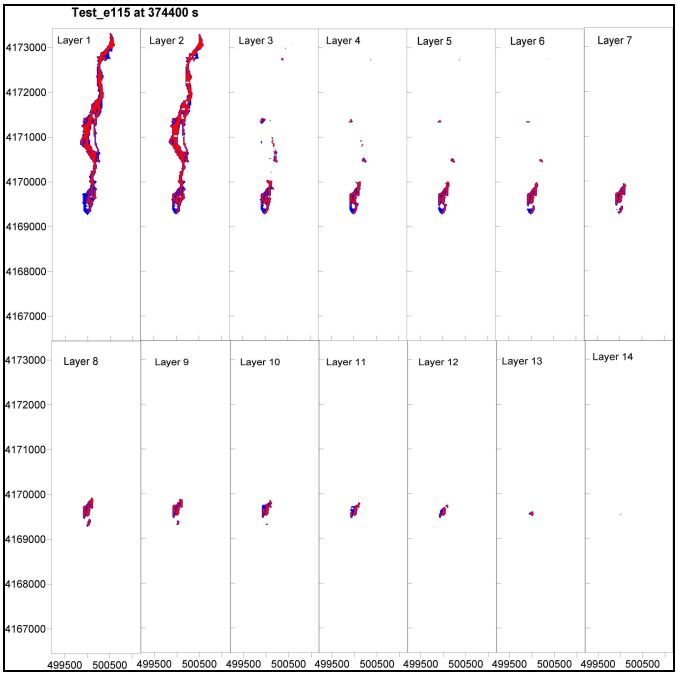

Figure 5.23: Liquid lava/crust distribution for test E115 at 374400 s (22/07); liquid lava is represented in red while crust is in blue.

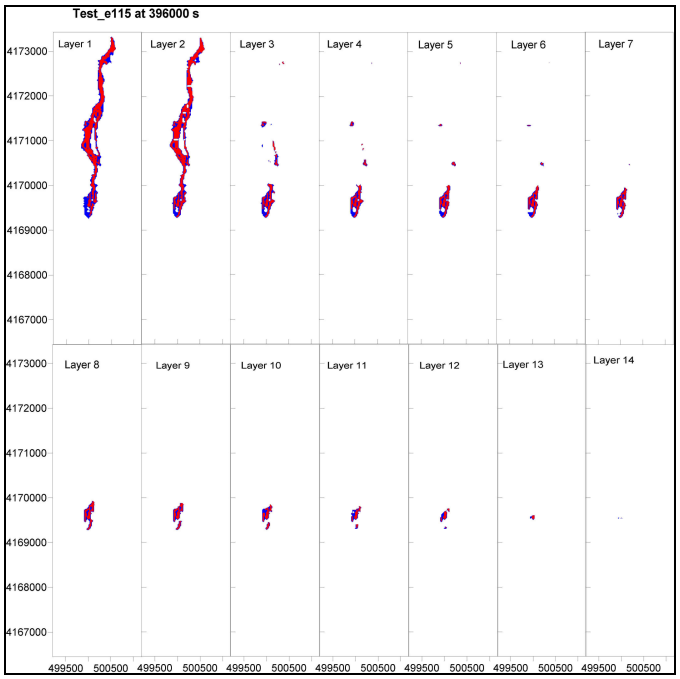

Figure 5.24: Liquid lava/crust distribution for test E115 at 396000 s (simulation end); liquid lava is represented in red while crust is in blue.

5.2.3 Comparison between simulated and observed data

As highlight from Figure 5.6 the path of the simulated and observed flows are quite similar, thought the simulated flows, with the exception of test E115 are, after the first day, normally longer and thinner, indeed the simulated flows seem to elongate much more than to thick. Moreover all the tests show some localized discrepancies in the 2D lava distribution, probably related to a not complete matching between the pre-eruption DEM and the real topographic surface.

The excessive lengthening, taking place after the 19 July, is emphasized by the PLR values. Figure 5.9 outlines that low viscosity simulations (C1, C2 and C4) are longer than the real flow (PLR>100) for all the considered dates, in particular the simulated flows arrived at the DEM bottom at the 20 July so these tests were not run further. High viscosity simulations (F2, V3, V111, V112, V114, V125, B115, B116 and EP114) are shorter than the real flow at the 18 July and, normally, longer at the 19 and 20 July with the exception of the V3 simulation, being shorter than the real flow at the 19 July. By considering test V112 (constant viscosity of 10^4 Pas) as an example, it is possible to

stress that the utilized viscosity value seems too high at the beginning and too low at the 20 July; the simulated flow is in fact shorter than the real one at the 18 July (PLR about 80%), it is quite similar at the 19 July (PLR about 110%) and it is longer at the 20 July (PLR about 130%). These results demonstrate that a constant viscosity is no good to simulate a lava flow temporal evolution, thought it could be possible to find a viscosity value to be used to reconstruct the final flow geometry but not useful to reproduce the flow emplacement, and thus to be used for real-time prediction. Nevertheless test C4, taking into account the viscosity-temperature law implemented in LavaSIM [*Goto et al.*, 1997], led to a simulated flow much longer than the real one. As a matter of fact Goto's law was not defined on the basis of Etna lava sample and its values, at the eruption temperature, resulted one order lower than those utilized in the high viscosity simulations (Figure 5.2) derived from *Giordano and Dingwell* [2003 b] law for hydrous lavas.

Test E115 does not show the excessive lengthening displayed by the other simulations between 19 and 20 July. On the contrary, it fits quite well with the observed flow until the 20 July and it is shorter at the 22 July. This behaviour is not related to a higher lava cooling, as discussed further, but it is due to the constant effusion rate which resulted in an emitted volume about 50% lower than the observed volume at the 22 July.

Figure 5.10 shows the Percent Length Ratio as a function of viscosity. It points out that PLR values generally decrease with higher viscosity, moreover the PLR values obtained, for the same day, from simulations with similar viscosities tend to group suggesting that viscosity is one of the main parameters governing the simulated lava spreading.

Figure 5.11, showing the Percent Length Ratio as a function of the solidification fraction of liquidity loss (b_{th}), does not highlight a precise trend, suggesting that b_{th} does not greatly influence the lava spreading.

The comparison between tests V114 and B115, differing only for b_{th} with B115 having the higher value and thus a later solidification, shows that the two simulations have comparable PLR at 18 and 19 July and that the B115 PLR, at 20 July, is lower than the V114 PLR. This behavior is related to the formation, in test V114, of well

developed lateral levees that prevented the lava lateral spreading and helped, at the same time, the flow lengthening. On the contrary the later solidification of B115 gave thinner levees, making still possible the lateral spreading and thus limiting the flow lengthening. This comparison suggests that a higher b_{th} influences the levees formation more than those of a solid front and thus it limits the lateral spreading more than the flow lengthening. Test B116 (same parameters as V114 and B115; b_{th} value intermediate between those of V114 and B115) confirmed that the influence of the solidification fraction of liquidity loss threshold is more relevant on the levees formation than on the front solidification. As a matter of fact B116 (having an intermediate solidification), at 20 July, is shorter than V114 and a little longer than B115; at the same time B116 presents a lateral spreading larger than V114 and very similar to that of B115. Nevertheless the three simulations show very similar lengths and lateral spreading at 18 and 19 July, This suggest that the solidification and thus the lava cooling becomes important only after the first two days of emplacement. Moreover the similarity between B115 and B116 suggests the augmentation of b_{th} from 0.65 (B116) to 0.8 (B115) had not a great influence on the lava spreading.

Figure 5.11 shows also that simulations with b_{th}=0.5 tend to group and that simulations with b_{th}=1 tend to spread along the entire graph length. This behavior is probably related to the viscosity, as a matter of fact all the simulation with b=0.5 have the same value while those with b_{th}=1 have different viscosities. It is important to note that simulations with b_{th}=0.5 are more dispersed at 20 July that in the previous days, confirming that the solidification and thus the lava cooling become important only after the first two days of emplacement.

The range of the utilized eruptive enthalpy is very small (Figure 5.12) so it is not possible to define a trend, though the PLR seems to increase for increasing eruptive enthalpies at low values, as confirmed by tests V114 and V112, differing only for eruptive enthalpy (V112 lowest entalpy). Moreover the PLR increases for test C4, having the highest enthalpy. Nevertheless this simulation, having a not constant viscosity evaluated from Goto's model, is based on a different enthalpy-temperature law (Figure 5.3). As a consequence it differs from the remaining simulations not only for the

not constant viscosity but also for the lava cooling. Tests C1 and C2 show a different trend (high PLR versus low eruptive enthalpy) though their behaviour is probably related to their low viscosities.

As regard to lava emissivity (Figure 5.13) most of the simulations have only two different values making not possible to individuate a trend for the PLR, though tests with different emissivity seems to have comparable PLR values. It is possible to compare three simulations (tests F2, V114 end EP114) differing only for lava emissivity with F2 and V114 having the lowest and highest values respectively. The three tests have similar PLR values at 18 and 19 July whereas they have different paths at 20 July resulting in different PLR: F2 and V114 have the lowest and highest values respectively. As a matter of fact F2 presents two overflows not shown by the other simulations while EP114 propagated (in its distal part) on a path differing from those of the other simulations (Figure 5.25).

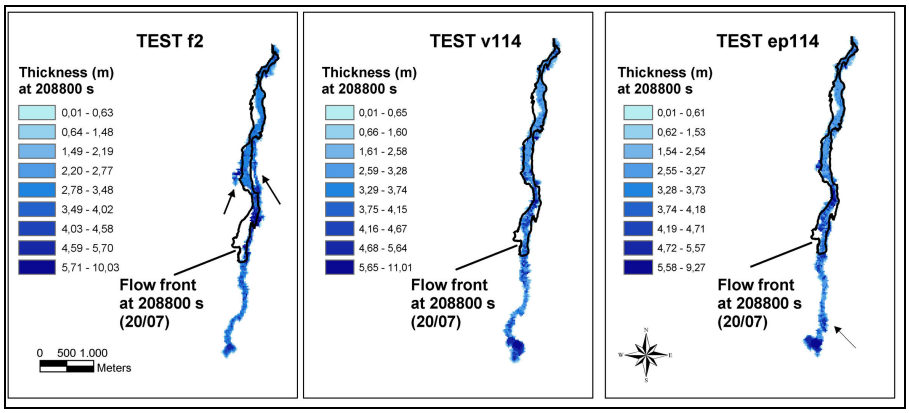

Figure 5.25: comparison between tests f2, v114 and ep114 at 20 July. Black contour define the observed flow limits at the same date. The arrows on test F2 individuate the overflows, while the arrow on test EP114 indicates the zone where it follows a path different from the other simulation.

The excessive lengthening, generally observed after the 19 July, is also responsible for the low values of e_1 (Table 5.2) generally lower than 0.8, where 1 testifies a complete comparability while 0 a complete discrepancy between simulated and observed lava spreading. Table 5.2 highlights also that better results were obtained for the low viscosity simulations (C2 and C4) at the beginning of the eruption while the high viscosity simulations seems better at the 19 July, confirming the problems related

to a constant viscosity. Moreover test V3, having the highest viscosity, and V111, being the high viscosity simulation with the lowest eruptive temperature, gave the best results at the 20 July.

Spataro et al. [2004] simulated a lava flow emplaced during 2002 on the NE Etna flank, obtaining a relatively low value (0.65) of the fitness function (e_1), though associated to a quite good qualitative agreement between the simulated and observed final flow geometries. In particular the simulated and observed length were very similar while the simulated flow presented a minor lateral spreading, resulting in the relative low value of e_1.

Similar or higher values of the fitness function (Table 5.2) were generally obtained (at the 19 and 20 July) for the LavaSIM simulations of the 2001 Etna main lava flow. However the qualitative comparison between the observed and simulated flow temporal evolution does not show such a good agreement, still considering the temporal evolution of test V112 (Figure 5.6) as an example. Its fitness function at 18, 19 and 20 July is equivalent to 0.59, 0.73 and 0.68 respectively, thus the flow at the 19 July should present the best agreement between simulated and observed geometries, as confirmed by Figure 5.6. By taking into consideration *Spataro et al.* [2004] result, test V112 at 20 July should be considered as a "good" simulation of the lava spreading. However Figure 5.6 and the PLR value of test V112 (Figure 5.7) demonstrated that the simulated flow is much longer than the observed one whereas the simulated and observed lateral spreading are very similar, resulting in a fitness function comparable with that obtained in *Spataro et al.* [2004]. As regard to the lowest value of e_1 at 18 July, it is probably due to the slow motion of the flow front resulting in a too short simulated flow. Similar considerations can be addressed to all the simulations carried out with LavaSIM.

The considerations about the V112 fitness function demonstrated that this function is not sufficient to verify the reliability of a simulation code. A better evaluation can be done when combining the fitness function (e_1), defining the agreement between the simulated and observed lateral spreading, and the percent length ratio (PLR), defining the agreement between the simulated and observed flow lengthening. Figure 5.26 reports the fitness function (e_1) versus the percent length ratio (PLR) for all the

simulations (but test E115) at 18, 19 and 20 July. A linear regression fit was applied to the three datasets:

$$Y = A + BX \tag{5.15}$$

The relative parameters and their standard deviations are reported in Table 5.3, with R coefficient of linear correlation and σ standard deviation of the fits. Tests V111 and C1 were not included in the fit of the 18 July data because they diverge from the linear regression.

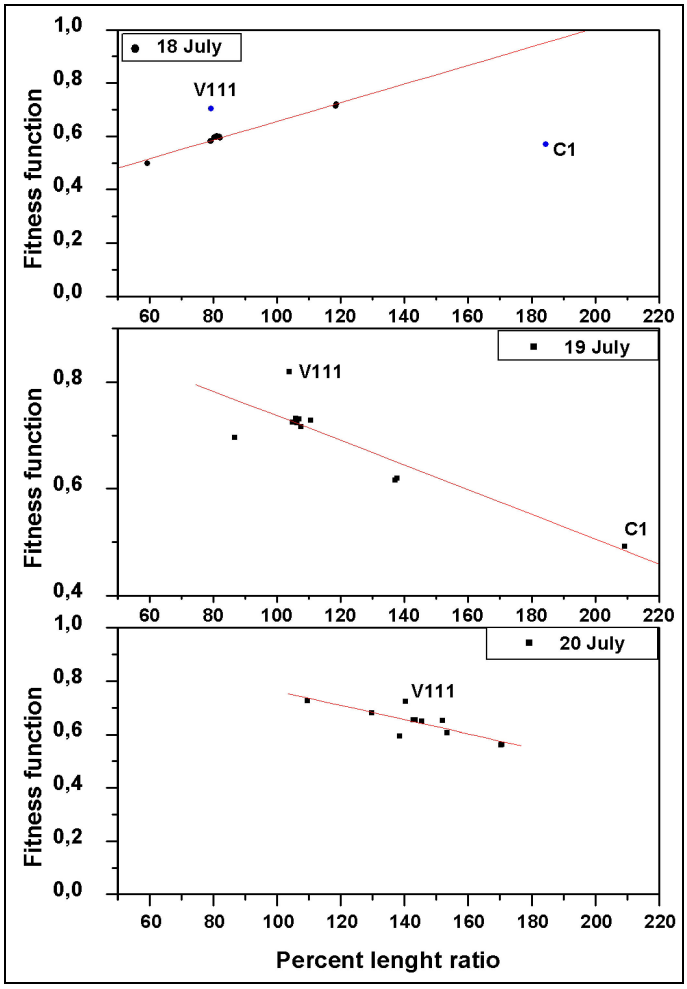

Figure 5.26: fitness function (e_1) as a function of the percent length ratio (PLR) for all the simulations but test E115, at 18, 19 and 20 July. Red lines represent the data linear fits. Blue dots at 18 July were not take into account in the corresponding linear fit.

The linear fits of Figure 5.26 shows the existence of a trend, for each date, suggesting that the percent length ratio (quantifying flow lengthening) and the fitness

function (quantifying flow lateral spreading) are related even if independent data, i.e. the results of different simulations, are taken into account. This can be explained by asserting that the flow volume, i.e. the unique parameters common to all the simulation, is the main factor controlling flow emplacement whereas the variation of the other parameters (viscosity, eruptive temperature and lava emissivity) has a limited influence in the relation between PLR and e_1. The linear fits of Figure 5.26 show that e_1 increases with increasing PLR values at 18 July, on the contrary it decrease at 19 and 20 July. However all the three trends demonstrated that better values of PLR correspond to better value of e_1, as a matter of fact PLR tending to 100 from both lower (18 July) and higher (19 and 20 July) values corresponds to e_1 which increases toward 1.

The V111 deviation from the fit can probably be related to its lowest emissivity, as a matter of fact it is the only high viscosity simulation having an emissivity as low as 0.7, which gives a lower cooling, and thus probably made lava spreading to predominate on flow thickening. A similar behavior can be observed also at 19 and 20 July, when its e_1 values are higher than those predicted by the linear fit, even if they can not be excluded.

	A	σ_A	B	σ_B (10^{-4})	R	σ
18 July	0,306	0,014	0,00350	1,6	0,992	0,008
19 July	0,968	0,046	-0,00231	3,8	-0,888	0,040
20 July	1,028	0,091	-0,00266	6,2	-0,819	0,033

Table 5.3: parameters obtained from the linear regression fits between e_1 and PLR at 18, 19 and 20 July (Figure 5.26).

As regard to the temporal evolution of the liquid lava and crust 3D distribution, test V112 (Figure 5.14 - Figure 5.18) shows the presence of lateral levees, appearing in the main layers after the first ten hours (18 July), and the lack of a well developed widening and cooling frontal area. This lack and, mostly, the liquid state of the furthest cells of the upper layers are probably responsible for the excessive lengthening, demonstrating that the code is, up to date, not completely able to reproduce the behavior of the lava flow front. Test E115 (Figure 5.19 - Figure 5.24) shows narrower lateral levees and it appears less cooled than V112 until 20 July, its front being still liquid while the corresponding area of test V112 was filled by crust. Test E115 undergone a front blockage after 20 July, resulting in the cooling and thickening of the frontal zone and

giving a maximum thickness of about 28 m on 23 July. The front thickness at 23 July was higher than that observed at the end of the eruption in the same area, thus this simulation was not run further. The best matching between E115 and the observed flow, for the 18 - 20 July, is therefore not related to an earlier cooling but to the lower emitted volume, this assertion is also supported by the low PLR value (Figure 5.9) obtained for the 22 July. After the 20 July the front cooling and the low effusion rate make not possible a further flow elongation. Therefore test E115 seems a volume limited flow and not a cooling limited flow until the 20 July, then both the processes concurred to front blocking and thickening.

5.3 Discussion on mismatch reason

The simulations of the 2001 Etna lava flow and, in particular, the 3D distributions of liquid lava and crust suggest that LavaSIM is, up to date, not completely able to simulate the flow cooling and, in particular, the front behavior. As a matter of fact all the simulations did not show the front widening typical of the lava flows.

The accurate reproduction of the flow front behavior is a crucial factor, indeed flow growth depends strongly on conditions at the flow front. Front velocity determines the rate of flow lengthening, moreover the front construct near-static lateral margins which concentrates the flow within a channel.

The channel transport the lava from the vent to the flow front; if continually fed a front grows during advance, owing to the supply of channel lava with higher velocity; front thickening will continue also when emission has ceased by channel drainage. Surface cooling will produce an outer crust at a rate limited by conduction. If lava accumulation in the front is too rapid, simple thickening cannot accommodate the extra lava and the front exterior is disrupted. Breaching is normally a local phenomenon, and it causes the opening of secondary (ephemeral) vents from which lava escapes from the flow interior.

The motion of an aa front is initially characterized by flow, then a thicker crust will develop around its snout and it will propagate by autobrecciation. An early aa front may roll forward as a caterpillar track, pulling its crust around the snout; when the upper

crust is slowed significantly by lateral resistance, the lava core may outwell through the snout, ahead of the surface layers. Then, at the beginning of autobrecciation, the frontal core oozes through and over lava fragments, dumped ahead of the snout (Figure 5.27). Finally in a very mature front, the snout autobrecciates completely to be bulldozed aside by the frontal core; it seems that, at this stage, lava comprising the snout interior had solidified during its transport from the vent [*Kilburn*, 1996].

Front motion is governed by an interaction between the rate of lava supply, controlling lava advance, and the solidification, controlling frontal resistance. Two different regimes are observed: the *core* regime, characterized by a single unit advance related to a persistent and widespread surface disruption; and the *crustal* regime, characterized by intermittent advance related to an episodic and localized surface disruption. In the core regime frontal conditions are limited by the rheology of the lava core, whereas in the crustal regime the escape of internal lava through the crust suggest that frontal conditions are limited by crustal restrain. Persistent disruption of new crust (core regime) is assured until the deforming forces (weight of the crust, pull from the core and bending forces around the snout) increase as quickly as the cooling induced tensile resistance of the crust [*Kilburn*, 1996].

Figure 5.27: front of an evolving lava flow (Etna 2006 eruption). It is possible to note the front autobrecciation, generating blocks of a few tens of centimetres and the core oozing.

Autobrecciations occurs because large enough strain rates are imposed by the rate of supply of new lava from upstream. Such failure transforms continuous lava into a collection of fragments that fall away from the front. Aa flows require a core pull to

persistently break their chilling crusts and can advance until their cores have solidified. Immediately before they solidify, fronts maintain continuous advance only by autobrecciating at least their snout [*Kilburn*, 2004].

Crust fracturing makes the front cooling more efficient than that from channel zone by two simultaneous processes: it exposes fresh lava (the flow core, having an higher temperature than the superficial lava) to the atmosphere, making possible radiation from the front snout, otherwise limited from the cool crusted surface; and it disrupts the flow surface into blocks, thus increasing strongly the surface of lava to be cooled by radiation and convection. On the contrary the heat loss from the channel zone is limited by the presence of static levees, already solidified and by the development of a plug zone, on the flow top, having a lower temperature than the core. In channelized lava flows a surface crust is carried freely down the central part of the channel, separated from the channel walls by well-defined crust-free shear zones due to lateral variations in flow velocity. Crustal extension and breakage are common in non-uniform channels where local flow conditions accelerate the flow surface. The increased fraction of incandescent lava exposed at the flow surface will generate more rapid cooling [*Cashman et al.*, 2006].

The LavaSIM simulations presented a well developed channel zone but did not show the radial spreading of the SFZ zone (Figure 2.1), moreover the width of the simulated channel zone is narrower than that of the observed flow. The narrowest channel is probably connected to the absence of the snout radial spreading. As a matter of fact the flow width is largely determined from that of the front, the flow normally undergoes a little enlargement after the lava front had passed ahead.

The observed behavior can probably be related to a too low cooling of the furthest cell of the frontal zone that did not prevent the flow lengthening, and thus did not facilitate the front widening and thickening. In the simulation solidified cells can move only in the z direction, so their presence in front of the lava flow should cause a front blocking and a thickening immediately behind the front, making possible overflow from the levees and thus the front widening. The simulated flows at 36000 s (Figure 5.14) did not yet have a solidified and widened front but they already presented the channel

structure, which had fixed the width of the proximal zone. This width remained almost constant during the simulations because flow widening is allowed only by means of overflows from the lateral levees (owing to the vertical motion of the crusted cells).

The code considers isothermal cells with the exception of those on the flow surface, which have an external layer characterized by a decreasing temperature. This assumption implies that the whole cell surface undergoes the same cooling processes, making no possible to take into account the frontal crust fracturing, which exposes fresh lava and makes more efficient the thermal radiation from the front. This peculiarity in addition to the great cell dimension (25 X 25 m) is probably responsible for the low cooling observed for the simulated flow fronts. The problems connected to the great cell dimension mostly arises on the front, because phenomena involving the lava front have lower scale than those characterizing the channel zone. It is therefore possible to average the lava cooling and motion of the proximal zone on such great cells but this bring to a not correct modeling of the front behavior. However the great cell dimension probably caused also an underestimation of the radiation from the flow top, as a matter of fact the simulated flow top are mostly composed of cells containing liquid lava.

A possible solution to avoid the underestimation of the frontal cooling, owing to the great cell dimension, is to apply an extra-cooling factor only to the furthest cells of the front. This factor should simulate the increase of the radiating surface and of its temperature owing to the exposure of fresh lava by the front disrupting. As a matter of fact most of the frontal cells in LavaSIM simulations are still liquid, though they have a surface temperature lower than that of the interior lava (the core) which in a real flow is exposed to the atmosphere by crust fracturing.

The excessive flow lengthening can also be addressed, as previously stated, to the neglecting of the temperature dependence of the viscosity. The utilized constant values seems too high for representing the eruption viscosity, as suggested by the low PLR values at 18 July, but too low a few days after the eruption beginning. A test, utilizing the viscosity law implemented in LavaSIM [*Goto et al.*, 1997], was run but it gave worse results. The eruption viscosity obtained from this law is one order of magnitude lower than those utilized in most of the test with constant viscosity (evaluated from

Giordano and Dingwell [2003b] viscosity law applicable to Etna lava). No good results were obtained also when using constant viscosities evaluated from *Giordano and Dingwell* [2003a] viscosity law for hydrous Etna lava. Better results could be probably obtained if the *Giordano and Dingwell* [2003b] viscosity law for multicomponent melt will be implemented in LavaSIM, allowing to adequately parameterize the viscosity of Etna lava.

All the simulations run using the two enthalpy-temperature laws implemented in LavaSIM based on literature data for the Izu-Oshima 1986 eruption [*Hidaka et al.,* 2005]. Different results should be obtained by using a different law considering Etna parameters (Figure 5.3). The Etna curve has the highest slope angle between the melting and solidifying temperatures, giving the highest lava temperature decreasing as a results of the same enthalpy variation. Nevertheless it is not possible to infer the influence of modified parameters of the enthalpy law, indeed such parameters are also necessary to evaluate the heat loss.

Simulation	Viscosity (Pa s)	Solidification fraction of liquidity loss	Lava Emissivity	Eruptive Enthalpy (MJ/Kg)	Eruptive Temperature (K)	End Time (s)	Notes
Test C1	670	1	0.7	1.2328	~ 1324	208800 20/07	Viscosity of Etna hydrous lava [*Giordano and Dingwell*, 2003a], water content 0.06% T=1082°C
Test C2	1500	1	0.7	1.2328	~ 1324	208800 20/07	Viscosity of Etna hydrous lava [*Giordano and Dingwell*, 2003a], water content 0.02% T=1082°C
Test C4	Goto's Model	0.8	0.95	2.3414	~ 1353	208800 20/07	
Test V3	$3.09 \cdot 10^4$	1	0.7	1.2293	1323	288800 21/07	Highest viscosity
Test F2	10^4	0.5	0.7	1.3253	1353	208800 20/07	Effusion rate linearly increasing versus time
Test V111	10^4	0.5	0.7	1.2989	~ 1345	237600 20/07, 21:00	
Test V112	10^4	0.5	0.95	1.2989	~ 1345	244800 20/07	Same test V111, higher lava emissivity Mass and energy not conserved after 208800 s owing to a too strong solidification at lava flow top
Test V114	10^4	0.5	0.95	1.3253	1353	244800 20/07, 23:00	Same as test V112, higher eruption temperature
Test V125	$1.46 \cdot 10^4$	0.5	0.95	1.3253	1353	208800 20/07	Same as test V114, higher viscosity
Test B115	10^4	0.8	0.95	1.3253	1353	208800 20/07	Same as test V114, higher solidification fraction of liquidity loss
Test B116	10^4	0.65	0.95	1.3253	1353	208800 20/07	Same as V114 and B115 tests, solidification fraction of liquidity loss between the V144 and B115 values
Test E115	10^4	0.5	0.95	1.3253	1353	446400 23/07	Same as test V114, constant lava emission z cell dimension 2 m
Test EP114	10^4	0.5	0.825	1.3253	1353	208800 20/07	Same as test V114, lower lava emissivity

Table 5.4: : simulation parameters for the 13 tests

6. The MAGFLOW simulation code applied to the 2001 Etna lava flow

6.1 The MAGFLOW simulation code

MAGFLOW [*Del Negro et al.*, 2007; *Vicari et al.*, 2006] is an algorithm based on the Cellular Automata approach for simulating, in two dimension, the emplacement of a lava flow.

Cellular Automata are discrete dynamic system (cells), which have a finite number of possible states. The state of all the cells is updated, at every step, by means of local rules (evolution function) depending on the state of the cell and of its neighboring. In MAGFLOW the state of the cells is defined by the lava thickness and the heat quantity.

6.1.1 The evolution function

The evolution function is the steady state solution of the Navier-Stokes equation for a Bingham fluid with constant thickness (h) flowing on an inclined plane [*Dragoni et al.,*1986]. In this way the flux between two adjacent cells is evaluated as:

$$q = \frac{S_y h_{cr}^2 \Delta x}{3\eta}\left(a^3 - \frac{3}{2}a^2 + \frac{1}{2}\right) \tag{6.1}$$

where S_y is the yield strength Δx is the distance between two adjacent cells, η is the viscosity and $a = h/h_{cr}$, with h_{cr} (critical thickness i.e. the minimum thickness having the possibility to flow) defined as:

$$h_{cr} = \frac{S_y}{\rho g\left(\sin\alpha - \frac{\partial h}{\partial x}\cos\alpha\right)} \approx \frac{S_y\sqrt{\Delta x^2 + \Delta z^2}}{\rho g(\Delta z - \Delta h)} \tag{6.2}$$

where ρ is the lava viscosity, α is the slope angle, Δz is the difference in height between the two cells and Δh is the difference in lava thickness.

Lava moves on when its thickness attain the critical values, thus the basal stress exceeds the yield strength.

This kind of evolution function induces a strong dependence on the cell geometry and position of the flux , with respect to the symmetry axis of the cells: flows on a flat plane tend to assume a rectangular shape instead to spread asymmetrically. A Monte

Carlo approach was adopted to solve this problem. A cellular automaton with randomized neighbors was considered: neighbor cells have their centers within a circle with radius R, centered on the central cell.

Lava flow morphology is strongly related to viscosity and yield strength both depending on lava temperature and composition. MAGFLOW defined the viscosity temperature relationship by means of the *Giordano and Dingwell* [2003a] model (Figure 5.2) relating the viscosity of hydrous Etna lavas to the temperature and the water content. Finally, yield strength is defined as a function of lava temperature by means of the *Ishihara et al.* [1989] relationship (S_y is a logarithmic function of T).

6.1.2 The heat model

MAGFLOW considers the lava as an isothermal fluid, this means that the temperature is homogeneous inside every cell. Lava cooling is supposed due to two different contributions: the radiative heat loss from the flow surface and the heat exchange due to lava mixture between adjacent cells. The heat quantity at the time t+Δt is thus defined as the sum of the heat quantity at t (Q_t), the heat exchange ($\Delta Q_{t,m}$) and the radiative heat ($\Delta Q_{t,r}$):

$$Q_{t+\Delta t} = Q_t + \Delta Q_{t,m} - \Delta Q_{t,r} \tag{6.3}$$

$$\Delta Q_{t,m} = \left(\sum_{q_i>0} q_i T_i + \sum_{q_i<0} q_i T_i \right) c_v \Delta t \tag{6.4}$$

$$\Delta Q_{t,r} = \varepsilon \sigma T^4 \Delta t \tag{6.5}$$

were T is the temperature of the central cell, T_i is the temperature of the neighboring cells, q is the flux between the central cell and its i-th neighboring, c_v and ε are the lava specific heat and emissivity and σ is the Stefan-Boltzmann's constant ($5.68 \cdot 10^8$ J/m^{2}sK). Then the temperature at the time t+Δt is:

$$T_{t+\Delta t} = \frac{Q_{t+\Delta t}}{\rho c_v h_{t+\Delta t} A} \tag{6.6}$$

were ρ is the lava density $h_{t+\Delta t}$ is the thickness and A is the area of the cell.

6.1.3 Input data

The input data, necessary to run MAGFLOW are the digital elevation model of pre-eruption surface, the physical and rheological lava properties, defined in Table 6.1 for Etna lava flows, the vents position and the effusion rate trend.

Parameter	Symbol	Value	Unit
Density of lava	ρ	2700	kg m^{-3}
Specific heat	c_p	840	J kg^{-1} K^{-1}
Emissivity of lava	ε	1	-
Temperature of solidification	T_s	1143	K
Temperature of extrusion	T_e	1360	K

Table 6.1: typical parameters of Etna lava flows [*Kilburn and Guest*, 1993]

At the initial state the thickness of all the cells is set to zero, then lava begin to be emitted from the cells set as vents according to the effusion rate trend and the thickness is calculated in the vent cells at every time step. The lava spreading begin when the thickness in the vent cells is higher than the critical thickness h_{cr} (6.2). Then lava will be distributed to the neighboring cells in accordance with the evolution function. Lava distribution in a cell will continue until its thickness is higher than the critical thickness and its temperature is higher than the solidification temperature. The thickness of the solidified cells is added to the cell elevation updating, at every time step, the topographic surface.

6.2 Simulation of the emplacement of an Etna lava flow

The MAGFLOW code was utilized, in addition to the LavaSIM code, to simulate the 2001 Etna lava flow emitted from the 2100 m a.s.l. vent [*Vicari et al.*, 2006].

The input data were represented by the 1999 DEM (cell dimension 10 m) and the LFS1 effusion rate trend described in paragraphs 4.4 and 4.5 and by the physical properties reported in Table 6.1. The flow emplacement history and the final lava distribution (Figures 4.6 and 4.7) were utilized to evaluated the reliability of the simulation code by comparing the daily planimetric distribution and the final thicknesses of the observed and simulated flows.

6.2.1 Analyses of the simulation results

The analysis of the MAGFLOW results is very similar to that performed for the LavaSIM results. The result analysis was not performed between the 26 July and the

end of the eruption (9 August). As a matter of fact the simulated flows did not show a planimetric expansion after the 26 July and the lava feeding resulted only in the flow thickening. On the contrary, the observed flow was still interested by lateral spreading, mostly in its frontal area, coupled with flow thickening and with the development of a lateral minor branch (30 July - 9 August) but not with a flow lengthening.

A qualitative judgment is based on the comparison of the simulated and observed emplacement histories (Figure 6.1 and Figure 6.2). Figure 6.1 is just describing the temporal evolution of the simulated lava spreading and thickening as well as the observed planimetric flow expansion. Figure 6.2 shows the differences between observed and simulated lava flow areas and highlights that MAGFLOW reproduced fairly well the temporal evolution and the lateral spreading of the 2001 lava flow. However the model tends to overestimate the area covered by the lava flow, probably due to some problems in the modeling of the lava rheological behavior and/or cooling process. Local discrepancies between simulated and observed areas can also be related to topographic artifacts. Largest discrepancies are observed at the 18 July and after the 22 July. In particular the simulated flow results longer than the observed one at the 18 July. The excessive lengthening in the first day of the eruption can probably be addressed to a not accurate evaluation (overestimation) of the effusion rate. Then the simulated and observed flow are in a good agreement until the 22 July when the flow lengths are quite the same though the simulated flow presents a higher front widening. After the 22 July the simulated length remained almost constant whereas the observed flow lengthened until the 26 July. This different behavior can be probably related to an underestimation of the effusion rate between 22 and 26 July or to the difficulty to simulate the flow behavior on a gentle slope. As a matter of fact the simulated flow attained, at the 22 July, an area characterized by a more gentle slope. Moreover the gentle slope on this area resulted in the creation of a quite flat zone, when interpolating the pre-eruption surface from contour maps. The arrival of the flow on a quite flat area was also coupled with the decreasing of the effusion rate, which slowed down the front, and thus promoted lava cooling. Finally the most remarkable incongruity is the lack of the lateral minor branch, in the simulated flow at the 9 August, due to the fact that the opening of the ephemeral vents, which fed this branch, was not taken into account in the presented simulation.

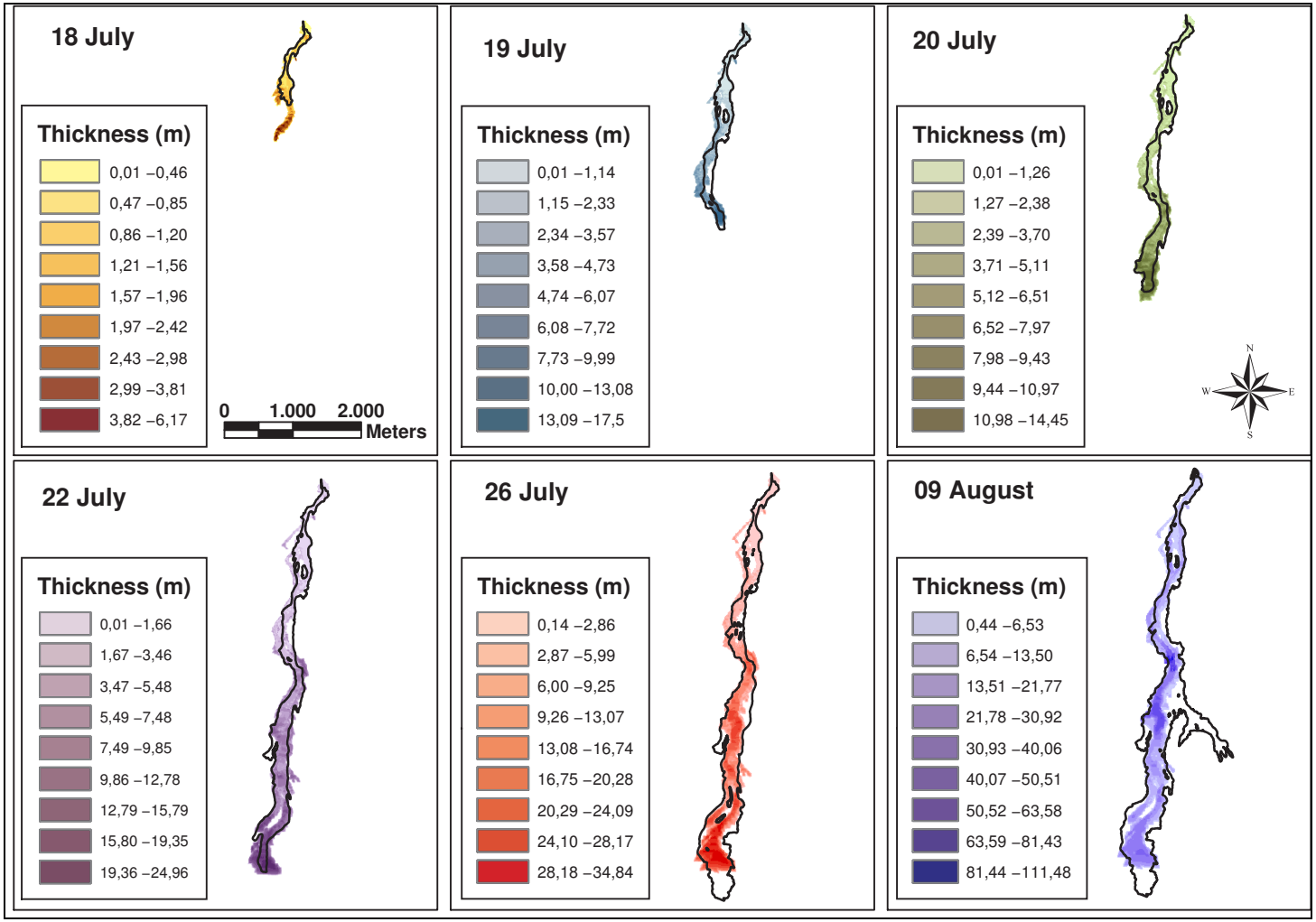

Figure 6.1: temporal evolution of the simulated and observed flows at the 18, 19, 20, 22, 26 July and 9 August. Black lines show the observed flow limits whereas the colors indicate the thickness of the simulated flow. The map scale is the same for the six maps.

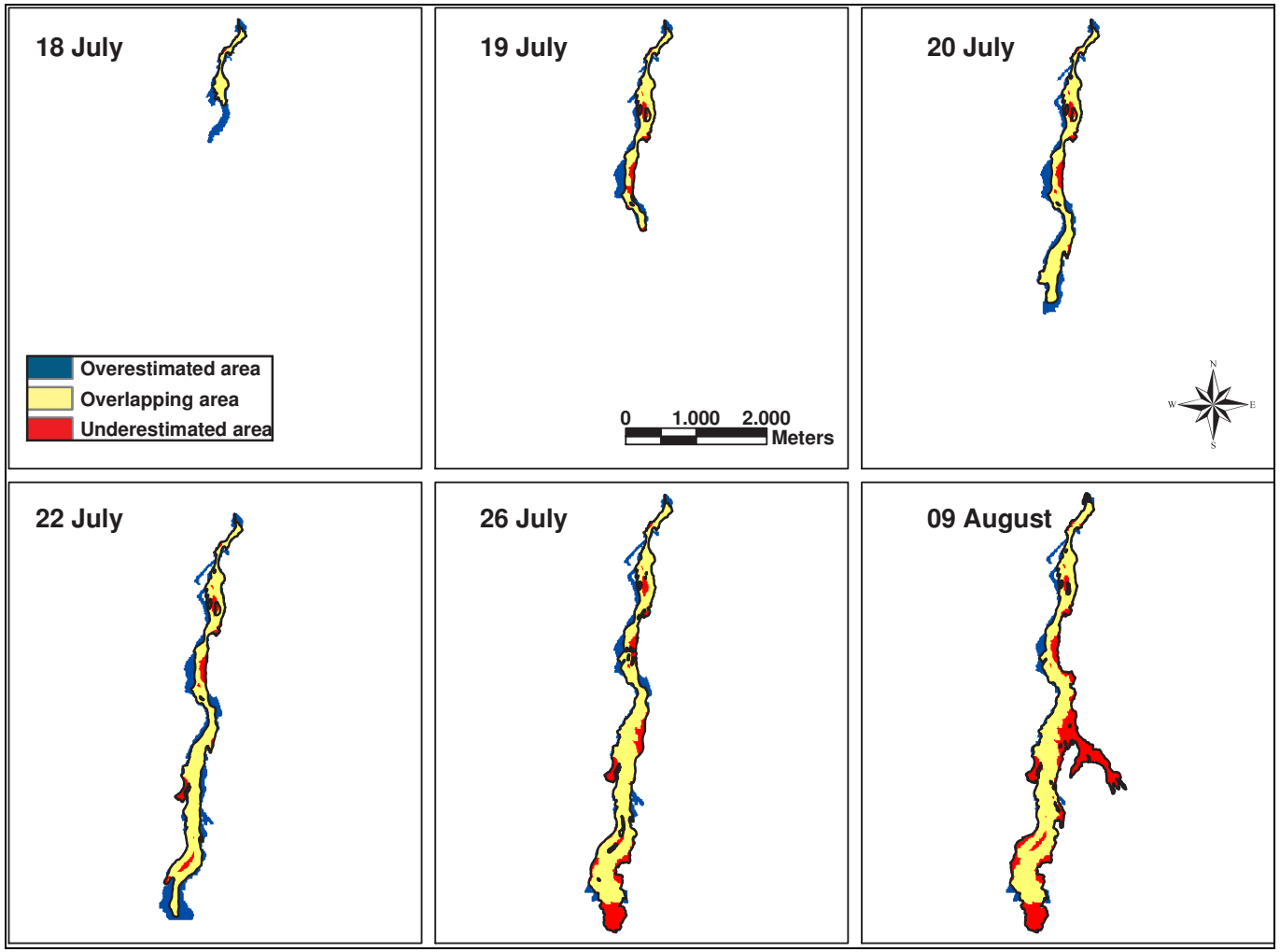

Figure 6.2: . Differences between observed and simulated lava flow areas at 18, 19, 20, 22, 26 July and 9 August. In red underestimated area, in yellow overlapping area, in blue overestimated area. The map scale is the same for the six maps.

The quantitative analysis of MAGFLOW results was not limited to the planimetric lava distribution but was completed by the comparison of the observed and simulated final thicknesses (Figure 6.3).

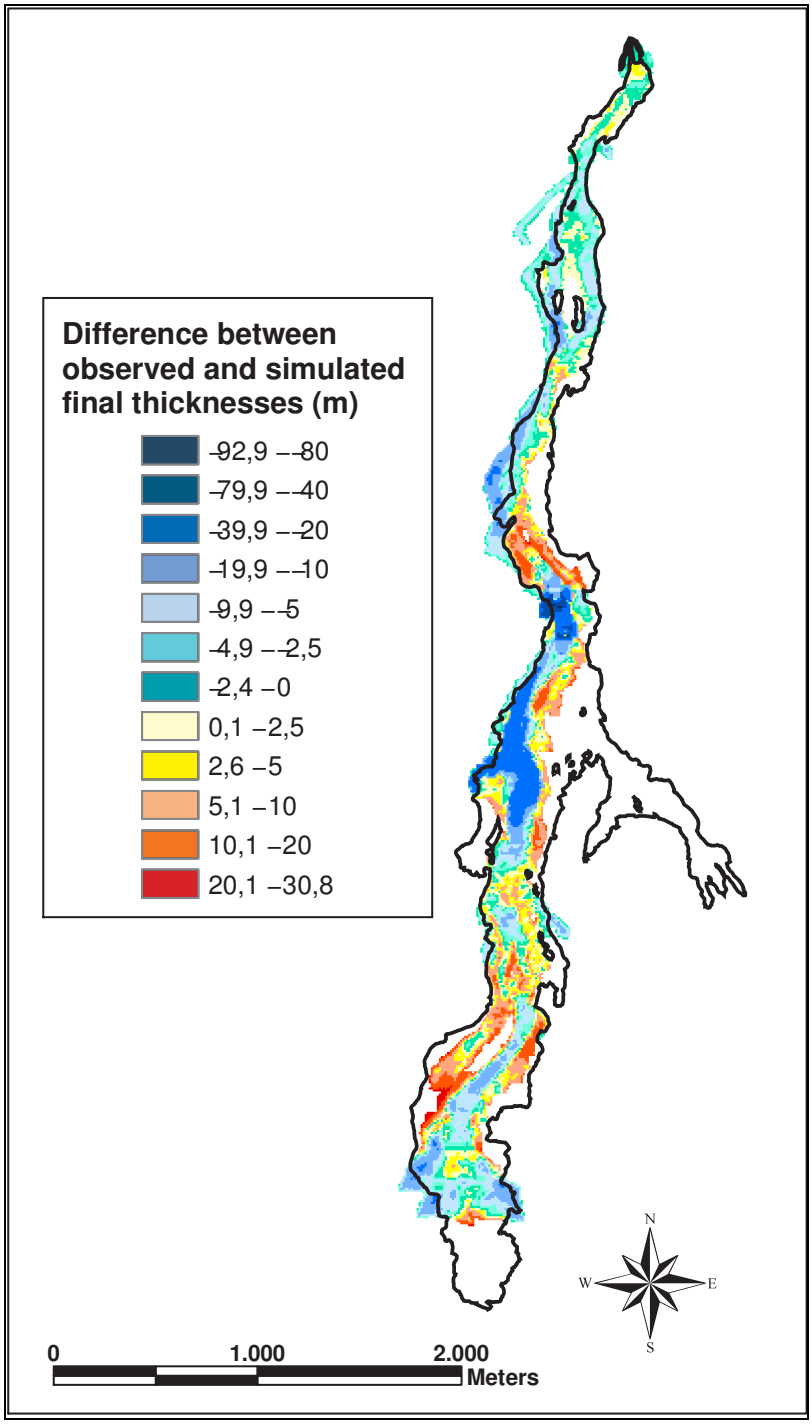

Figure 6.3: Difference between observed and simulated final thicknesses (at 09 August) evaluated only in the area covered by the simulated flow.

The simulated flow is normally thicker that the observed one, though it is possible to observe underestimation of the final thickness mostly on the levees of the simulated flow and where the flow changes direction. A relevant thickening of the simulated flow can be observed starting near the lateral branch and propagating upward. Its shape suggests that it was caused by a regression of the simulated active front, occurred between the 26 July and the 9 August and its location can be connected to the neglecting of the ephemeral vents, feeding the lateral branch between the 30 July and the 9 August. The neglecting of the ephemeral vents, implied that the lava volume which fed the lateral branch was accumulated behind it instead of being released towards Mt. Grosso (Figure 4.2). In MAGFLOW an ephemeral vent can be simulated only as a new vent having its own effusive history.

The assertions about the planimetric comparison between simulated and observed flow can be quantitatively supported by the length and area comparisons (Figure 6.4), as well as by the evaluations of the percent length ratio (PLR) (Figure 6.5) and of the fitness function (e_1), reported together with the PLR value (Figure 6.6).

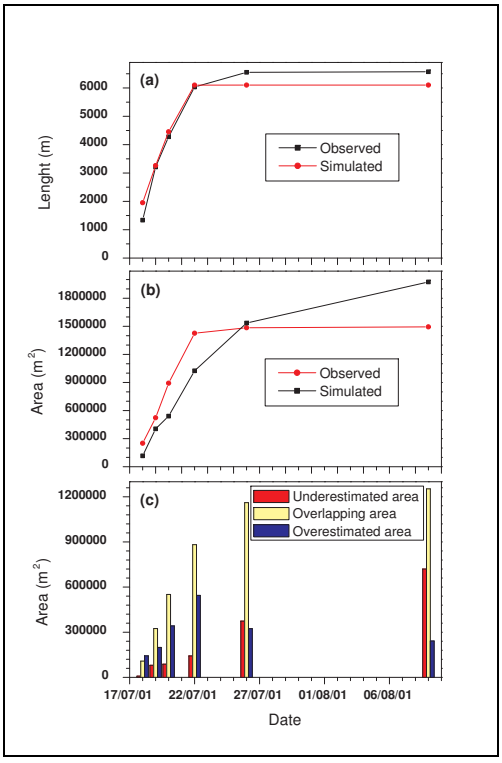

Figure 6.4: Quantitative comparison between simulated and observed flow geometries at 18, 19, 20, 22, 26 July and 9 August: (a) length computed along the flow direction; (b) total area; (c) differences between lava spreading.

Figure 6.5 indicates that the simulated and observed lengths are comparable between the 19 and 22 July, resulting in a PLR value close to 100%, whereas a PLR of about 93% was obtained both at the 26 July and 9 August. By looking at Figure 6.4a, it is possible to stress out that this lower value is due to an earlier stop of the simulated flow, as a matter of fact it did not elongate after the 22 July whereas the observed flow was still moving until the 26 July. On the contrary, a higher PLR value (about 146%) was obtained at the 18 July, probably owing to an overestimation of the effusion rate, as already stated. This analysis suggests that MAGFLOW is able to reproduce quite accurately the temporal evolution of the flow elongation given the availability of a suitable effusive history.

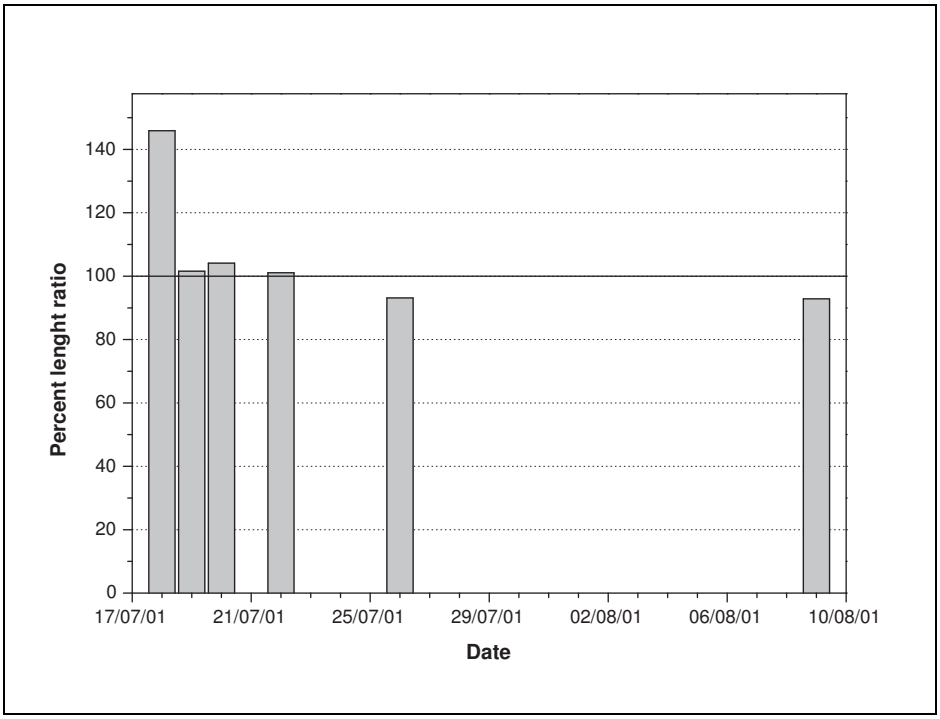

Figure 6.5: comparison between simulated and observed length described by means of the percent length ratio at 18, 19, 20, 22, 26 July and 9 August.

As already discussed in the analysis of LavaSIM results, the PLR value is not sufficient to evaluate the reliability of a lava flow emplacement simulation. Thus the fitness function (e_1), that is the ratio between the intersection and the union of simulated and observed areas, was evaluated for the six selected dates (Table 6.2) and reported in Figure 6.6, together with the corresponding PLR values.

Date	Fitness function (e_1)
18 July	0.65
19 July	0.73
20 July	0.75
22 July	0.75
26 July	0.79
9 August	0.75

Table 6.2: fitness function of the MAGFLOW simulation at the six selected dates.

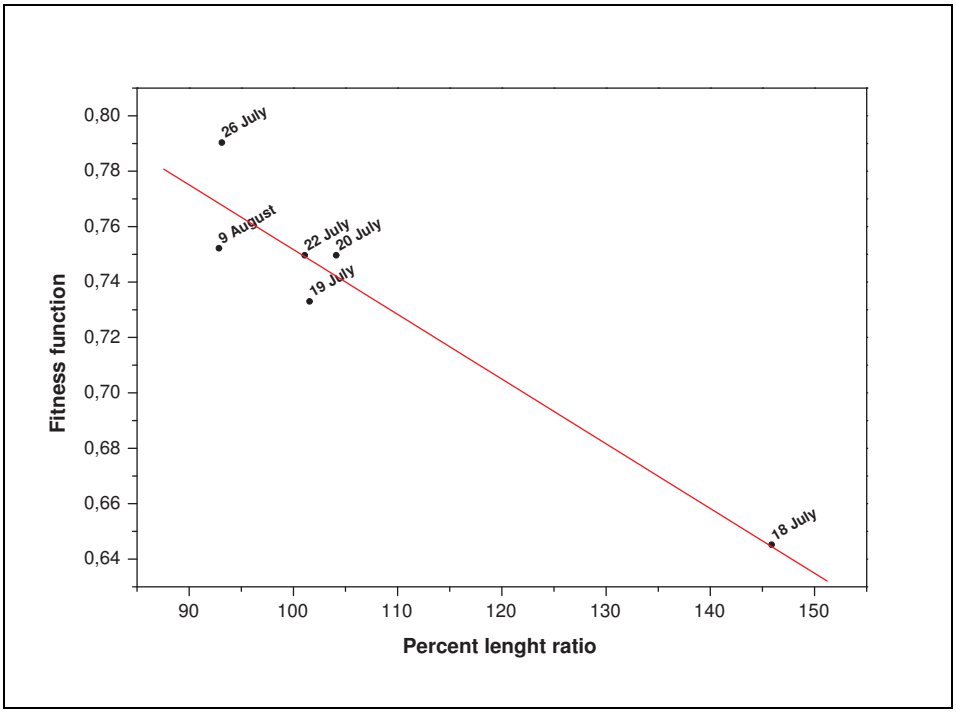

Figure 6.6: fitness function (e_1) as a function of the percent length ratio (PLR). Red line represents the data linear fit.

The values of the fitness function obtained by the MAGFLOW simulation are higher than those of the LavaSIM simulations and of the *Spataro et al.* [2004] case. The analysis of the fitness function (Table 6.2) indicates that the best matching between simulated and observed flow spreading was obtained at the 26 July. This highest value of e_1 should be addressed to the balancing of underestimated and overestimated area (Figure 6.4c), which resulted in very similar simulated and observed total areas (Figure 6.4b). Nevertheless the simulation at 26 July gave a relatively low (about 93%) PLR value owing to an earlier stop of the simulated flow front. Thus the flow at the 22 July can be considered as the best matching between simulated and observed flow. As a

matter of fact it reproduces quite well both the lava lengthening (PLR~101 %) and the lava spreading (e_1~0.75) (Figure 6.6).

Figure 6.6 shows also that it is possible to define a linear relationship (5.15) between the fitness function and the percent length ratio, not only when considering the results of different simulation at the same date, as for LavaSIM results (figure 5.26) but also when considering the same simulation at different dates, as for MAGFLOW results. The parameters obtained by the linear regression fit of the MAGFLOW results (Figure 6.6) are reported in Table 6.3 showing that a negative linear correlation exists between the two variables.

A	**σ_A**	**B**	**σ_B (10^{-4})**	**R**	**σ**
0,985	0,034	-0,00234	3,7	-0,954	0,016

Table 6.3: parameters of the linear regression fit (Figure 6.6) between the e_1 and PLR values

7. Conclusions

Many numerical codes have been developed to simulate the emplacement of lava flows for evaluating their possible evolutions and for defining, by a statistical approach, hazard maps useful for land planning.

This work presents a revue of the existing simulation codes, distinguishing deterministic from probabilistic models. Deterministic models generally adopt a simplified description of the phenomena involved in the lava flow emplacement, though a code (LavaSIM) was developed to completely solve the problem. Probabilistic models utilize a quite simplistic distribution method, based only on the underlying topography.

Most of the considered deterministic codes adopt the 2D simplifications (the unique exceptions are LavaSIM, 3D, and FLOWGO, 1D): they consider cells filled by an isothermal lava, and their thickness is determined on the base of flow between adjacent cells. This approach also implies that the whole lava layer, contained inside every cell has the same physical properties. However this simplification is practically imposed by the long computation times of a 3D evaluation. As a matter of fact LavaSIM presents a quite long computational time even if it runs on a parallel computer. The 2D simplification results very useful when adopting the codes for real-time application, though a complete 3D solution is necessary when trying to understand the phenomena governing the lava flow emplacement and the influence of the adopted parameters.

A limiting factor of all the 2D codes is that they do not take into account the crust formation, a factor greatly influencing the flow emplacement: the crust on the flow top limits the lava cooling, thus increases its capability to propagate far from the vent. Moreover the formation of a lava tube inhibits the cooling, making possible the transportation of a quite unmodified lava (same temperature, chemical composition, rheology and physical parameters) from the emission point to ephemeral vents, thus obtaining a flow much longer than if it would flow on a open channel. This behavior, characteristic of long lasting lava flow having a low effusion rate [*Kilburn and Lopes*, 1991], is not reproducible by the actual 2D codes. The 2D codes generally discriminate solidified lava on the base of its temperature, adding the corresponding thickness to the underlying topography, while resetting to zero the quantity of lava to be distributed to the adjacent cells. On the contrary LavaSIM takes into account crust formation by

evaluating the enthalpy of every cell. Solidified cells are still considered in the subsequent computations, though their motion is limited to the vertical direction. The FLOWGO [*Harris and Rowland*, 2001] code also attempted to consider the crust formation when evaluating the radiative heat loss by introducing an empiric *f* factor, defining the fraction of not-crusted flow surface as a function of the flow velocity. The greatest limitation of this code is its 1-dimensional solution, though it results except LavaSIM, the most complete code for describing the mechanisms involved in the emplacement of a lava flow.

The probabilistic models did not describe the flow emplacement and the related phenomena but they only evaluate the path a fluid will follow on a defined topography, rarely taking into account factors for limiting the maximum allowed path [*Favalli et al.*, 2005; *Damiani et al.*, 2006]. Such codes can therefore evaluate only the maximum area to be invaded, to the utmost relating emplacement times to probabilities of invasion: less probable areas will be covered later.

Deterministic models were tested on actual lava flows to evaluate their reliability. Generally these tests were limited to the final geometry of the lava flow owing to the lack of data describing its temporal evolution, thus no example exist of a code validate throughout the whole lava flow. Finally, all the literature examples gave quite qualitative analysis of the carried out simulations, whereas only a few of them tried to quantify the correspondence between simulated and actual flows.

When investigating on the literature examples of lava flow simulations it is also important to discuss about the utilized input (chemical and physical lava properties, as well as pre-eruption surface and effusion rate) and checking data (flow field planimetry), whose accuracy was commonly quite low.

As regard to chemical and physical lava properties, when utilized, they were derived from literature. Field data are scarce due to logistical difficulties in taking measurements from active lava, while laboratory studies do not recreate actual emplacement conditions and so their results are purely indicative [*Kilburn*, 1996]. There are significant differences between, for example measurements on the rheological properties of lavas in the laboratory and in similar measurements in the field. Realistic three-dimensional models of lava flows require, as input data, accurate measurements of

the rheological, thermal and related physical properties of the margins and isothermal interiors at different stages in the development of a flow.

Recent studies of active lava, have becoming increasingly more sophisticated with advances in monitoring equipment, measurement of flow parameters, theoretical and experimental investigations. Field observations, however, are critical to guide and to integrate all forms of instrumental monitoring, for furnishing realistic boundary conditions and constraints in computer modeling of flow dynamics and other eruptive phenomena, and to provide the ground truth [*Tilling and Peterson*, 1993].

As regard to pre-eruption surfaces, they were interpolated from contour maps, without considering their accuracy, which sometimes resulted lower than the flow thicknesses. Moreover some of the utilized topography were not updated in certain areas [*Ishihara et al.*, 1989]. Finally, effusion or eruption rates were generally derived from previous works, devoted to the eruption description rather than to quantitatively reconstruct the flow emplacement. Thus the utilized data were probably derived from syn-eruptive measurement of area and thicknesses. Such data may give volume and effusion rate values very different from those obtained from an accurate post-eruption analysis of the flow emplacement [*Coltelli et al.*, 2007]. The use of unverified checking data also limits the reliability of data comparison: in all the test cases final flow area was derived from qualitative maps and rarely from aerial photo.

Finally, many of the analyzed simulation codes use, as test cases, short-lived lava flows. Such flows are characterized by simple emplacement mechanisms, mostly governed by flow thickening, and are volume limited flows. Their propagation generally stops when the vent is no more fed, with the exception of a brief further lengthening, connected to channel drainage. They thus have a more simple emplacement mechanism than the cooling limited flows, whose lengthening is generally impeded by front cooling, and is associated with flow thickening and/or bifurcation. LavaSIM is a clear example of such a problem: it gave good results on its previous application [*Hidaka et al.*, 2005] and on the first days of the Etna lava flow (chapter 5), though worse results were obtained for the Etna flow when the thickening became important, and consequently limited the lengthening of the actual flow.

This work demonstrated the need to define a methodology to asses the reliability of numerical models for lava flow simulating. An ideal test case (the 2001 Etna main lava

flow) was selected to define and carry out an appropriate analysis. The final flow geometry, as well as the temporal evolution of its spreading and of its daily effusion rate were accurately evaluated. The pre and post-eruption topography were interpolated from contour maps, permitting to evaluate the final 3D geometry of the flow. A semi-quantitative method, based on the analysis of daily maps and flow thicknesses, was adopted to reconstruct the flow evolution, from which daily effusion rates were evaluated. Finally an error analysis was conducted to estimate volume accuracy [*Coltelli et al.*, 2007].

The Etna flow was then simulated by the LavaSIM and MAGFLOW codes, and the simulated and actual flows were quantitatively compared. Planimetric correspondence (on covered area and flow length) was daily checked by defining a fitness function for the area and a percent length ratio, whereas final thickness distribution, from the MAGFLOW simulation, was also controlled. The fitness function on the simulated and actual areas, already defined by *Spataro et al.* [2004], resulted not sufficient to evaluate the goodness of a simulation test, thus the percent length ratio was defined to evaluate the correspondence between the simulated and observed lengths. The simultaneous adoption of these two parameters permitted to check both the simulated lava spreading and lengthening. Otherwise simulations presenting a too high flow lengthening but a fitness function comparable with *Spataro et al.* [2004] would have been considered as acceptable results. Moreover the simultaneous adoption of these two parameters completely constrained the flow emplacement, the third dimension, i.e. the thickness, is strictly related to flow length and width by the volume, fixed by the effusion rate trend.

The analysis of the 2001 Etna flow provided a dataset having a higher accuracy than that utilized in previous simulation of the same lava flow, based on syn-eruptive data [*Crisci et al.*, 2004]. Moreover the availability of a quasi-daily temporal evolution permitted to check the code capability not only at the end of the simulation but also step by step during its emplacement. Such check results very useful if the code have to be applied for real time hazard evaluation, that is for forecasting the possible evolutions of an ongoing eruption.

A limitation of the carried out simulations is still the adoption of literature data for some of the physical parameters involved in the simulations (lava density and thermal parameters). Literature data are normally referred to a generic Etna lava flow and

measurements for a specific eruption are rarely carried out, however the chemical composition of the 2001 flow is available [*Taddeucci et al.*, 2004].

The analysis of the LavaSIM results demonstrated the great capability of this model. As a matter of fact LavaSIM is the only full 3D model, thus able to account for the vertical variation of lava properties, such as temperature, viscosity, velocity and liquidus or solidus state. Moreover it present the most complete description of the lava cooling, accounting for radiation, convection and conduction whereas most of the simulation codes consider only heat radiation and lava mixing. It also considers viscosity, thermal conductivity (empirical relation) and enthalpy as functions of temperature, though it adopts a few simplifications (constant density and yield strength) to not further increase the computation time. Unfortunately it should be further tested to evaluate the parameters to be adopted and to tune the model for better reproducing frontal behavior. As a matter of fact, the carried out simulations demonstrated that the modeling of the lava cooling should be improved, mostly owing to the great cell dimension which causes an underestimation of the heat loss at the surface top and from the flow front.

The greatest peculiarity of LavaSIM is its potential to discriminate between cells filled by liquid or solid lava, thus allowing to simulate the channel formation and the development of a crust at the flow top, giving rise to lava tube development. However the capability of the code to solve the Navier-Stokes and the energy conservation equations requires a very long computation time. This implies that a quite great cell dimension should be selected to not have very long lasting simulations. The great cell dimension makes not possible to completely reproduce little scale phenomena, such as the crust fragmentation at the flow front, responsible for the greatest cooling of such flow area, as observed in actual flows. Crust fragmentation increases the area to be cooled and its temperature, owing to the oozing through and over lava fragments of the hotter core. The neglecting of such phenomena is probably one cause of the too high lengthening presented by the LavaSIM simulations of the 2001 Etna flow. Further studies should be conducted to evaluate a parameter to be applied, solely to the frontal cells, in order to simulate the most efficient cooling of the front. The importance of the frontal behavior was already recognized [*Kilburn*, 1996] though existing models are limited to its motion and did not try to evaluate its cooling.

Up to date LavaSIM is the best code to be applied for understanding the mechanisms controlling the lava flow emplacement, though it cannot be adopted for real-time application owing to its long computation time and to the not good description of the front behavior and cooling.

The analysis of the MAGFLOW results demonstrated that this code was quite able to reproduce the emplacement time of the 2001 Etna flow, though some problems arose when the lava was flowing on a gentle slope of the underlying surface. As a matter of fact the final simulated flow was shortest than the actual one and the underestimated area in the flow front (figure 6.2 after 26 July) corresponds to a more gentle slope. The code was wrote for taking into account the flow driven by the pressure gradient related to thickness variation, thus it should be able to simulate the lava motion also on a less steep slope. However the arrival of the flow on a quite flat area corresponded also to the decline of the effusion rate. The stop of the simulated flow should be attributed to the concomitance of two different phenomena: the propagation on a minor slope, and the declining of the effusion rate. The latter slowed down the front, making possible the flow stop owing to lava cooling. The reliability of parameters derived from the analysis and interpretation of field and post-eruption data, such as those useful for the estimation of the flow rate, allowed to verify the capability and performance of the modeling implemented in MAGFLOW. The good performance obtained for the 2001 Etna flow makes the model an efficient and robust tool for estimating the areas that will be affected by potentially destructive lava flows. Consequently, this tool could be a key extension of an efficient monitoring system of the lava flow eruption, like that operating at Etna volcano.

This work also demonstrated that data collected on site during the eruption evolution are necessary in order to simulate realistic scenarios, in particular the quasi-daily geometry of the 2001 Etna lava flow resulted very important for code validating. As a matter of fact geometrical and topographical data were adopted both as input data, to evaluate the effusion rate trend, and as check data, for assessing the reliability of the results.

Data to be used for code validating should therefore be evaluated by means of techniques having a well known accuracy, easily to be estimated. Flow volume, area and thickness can be evaluated with high accuracy when sufficiently detailed

topographic data are available before, during, and after an eruption. Moreover volumes based solely on field data, such as those evaluated from a planimetric approach (product between covered area and average thickness), can be affected by large errors and are not adequate to reconstruct a lava flow evolution. In order to apply a completely quantitative approach for the reconstruction of a lava flow evolution, data for generating DEMs should be daily collected (ideally) for example by means of photogrammetric or LIDAR surveys.

Appendix A

The volumes (V) computed from the DEM subtraction (Table 4.1) were calculated from:

$$V = \sum_{ij} \Delta x^2 \cdot \Delta z_{ij} \tag{1}$$

where $\Delta x = 10m$ is the linear dimension of the square cells and Δz_{ij} is the height variation between the 1999 and the 2001 DEM. The sum is limited to cells inside lava flow limits. The standard deviation associated with this volume is calculated from the variance propagation law:

$$\sigma_V = \sqrt{\sum_{ij} \left(\left(\frac{\partial V}{\partial z_{ij}} \right)^2 \sigma_{\Delta z}^2 + \left(\frac{\partial V}{\partial x} \right)^2 \sigma_{\Delta x}^2 \right)} = \sqrt{\sum_{ij} (\Delta x^4 \cdot \sigma_{\Delta z}^2 + 4 \cdot \Delta z_{ij}^2 \cdot \Delta x^2 \cdot \sigma_{\Delta x}^2)} \tag{2}$$

where $\sigma_{\Delta x} = 10m$ is the planimetric accuracy and $\sigma_{\Delta z} = 2.69m$ is the lava residual vertical accuracy.

The volumes obtained from the planimetric approach (Table 4.2) were calculated from:

$$V = A \cdot \overline{H} \tag{3}$$

where A is the area covered by lava, evaluated by means of a mass balance analysis, and $\overline{H}$ is the average flow thickness. The related standard deviation is:

$$\sigma_V = \sqrt{\left(\frac{\partial V}{\partial \overline{H}} \right)^2 \sigma_{\overline{H}}^2 + \left(\frac{\partial V}{\partial A} \right)^2 \sigma_A^2} = \sqrt{A^2 \cdot \sigma_{\overline{H}}^2 + \overline{H}^2 \cdot \sigma_A^2} \tag{4}$$

where $\sigma_{\overline{H}} = 1m$ is the accuracy of the thickness measurements, and $\sigma_A = n\Delta x^2$ is the area accuracy, with n being the number of cells forming the perimeter of the lava flow and of its dagala.

Total volumes for the LFS2, UFS1 and UFS2 flows (Table 5) were obtained by summing or subtracting DEM volumes (V1) and volumes evaluated by means of the planimetric approach (V2) so their final accuracy can be given as the square root of the sum of the calculated standard deviations:

$$\sigma_V = \sqrt{\sigma_{V1}^2 + \sigma_{V2}^2} \tag{5}$$

References

Baldi P., S. Bonvalot, P. Briole, M. Coltelli, K. Gwinner, M. Marsella, G. Puglisi, and D. Remy (2002), Validation and comparison of different techniques for the derivation of digital elevation models and volcanic monitoring (Vulcano Island, Italy), *International Journal of Remote Sensing,* 23, 22, 4783– 4800.

Baldi P., M. Fabris, M. Marsella, and R. Monticelli (2005), Monitoring the morphological evolution of the Sciara del Fuoco during the 2002-2003 Stromboli eruption using multi-temporal photogrammetry, *ISPRS Journal of Photogrammetry and Remote Sensing,* 59, 199-211.

Barberi F., M. L. Carapezza, M. Valenza, and L. Villari (1993), The control of lava flow during the 1991-1992 eruption of Mount Etna, *J. Volcanol. Geotherm. Res.*, 56, 1-34.

Barberi F., and M. L. Carapezza (2004), The Control of Lava Flows at Mt. Etna in *Mount Etna volcano laboratory*, pp 357-369, edited by A. Bonaccorso, S. Calvari, M. Coltelli, C. Del Negro, S. Falsaperla, Geophysical monograph series, 143, AGU, Washington.

Barca D., G. Crisci, S. Di Gregorio, and F. Nicoletta (1987), Lava flow simulation by cellular automata: Pantelleria's examples, in *Proceedings, International Applied Modelling and Simulation: Cairo, Egypt, International Association of Science and Technology for Development (IASTED)*, 4A, 9–15.

Barca D., G. Crisci, S. Di Gregorio, S. Marabini, and F. Nicoletta (1988), Nuovo modello cellulare per flussi lavici: Colate di Pantelleria, *Bollettino del Gruppo Nazionale per la Vulcanologia: Roma, Italy, Consiglio Nazionale delle Ricerche*, 41–51.

Barca D., G. Crisci, S. Di Gregorio, and F. Nicoletta (1993), Cellular automata methods for modelling lava flows: simulation of the 1986-1987 eruption, Mount Etna, Sicily, in *Active lavas: monitoring and modelling*, UCL Press, London, Kilburn C.R.J., Luongo G, Ed., 291-303.

Barca D., G. Crisci, R. Rongo, S. Di Gregorio, and W. Spataro (2004), Application of the Cellular Automata Model SCIARA to the 2001 Mount Etna Crisis, in *Mount Etna volcano laboratory*, pp 343-356, edited by A. Bonaccorso, S. Calvari, M.

Coltelli, C. Del Negro, S. Falsaperla, Geophysical monograph series, 143, AGU, Washington.

Bayley F. J. (1955), An analysis of turbulent free convection heat transfer, *Proc. Inst. Mech. Ing.* 169, 20-361.

Behncke B., and M. Neri (2003), The July-August 2001 eruption of Mt. Etna (Sicily), *Bull. Volcanol.,* 65, 461-476, doi: 10.1007/s00445-003-0274-1.

Boschi E, and E. Guidoboni (2001), Catania terremoti e lave dal mondo antico alla fine del Novecento, *INGV- GA, Compositori editore*, pp 414.

Branca S., and P. Del Carlo (2004), Eruptions of Mt Etna during the past 3,200 Years: a revised compilation integrating the historical and stratigraphic records, in *Mount Etna volcano laboratory*, pp 1-27, edited by A. Bonaccorso, S. Calvari, M. Coltelli, C. Del Negro, S. Falsaperla, Geophysical monograph series, 143, AGU, Washington.

Branca S., and P. Del Carlo (2005), Types of eruptions of Etna volcano AD 1670–2003: implications for short-term eruptive behaviour, *Bull. Volcanol.,* 67, 732-742.

Calvari S., M. Coltelli, M. Neri, M. Pompilio, and V. Scrivano (1994), The 1991-1993 Etna eruption: chronology and lava flow-field evolution, *Acta Vulcanologica*, 4, 1-14.

Calvari S., and the whole scientific staff of INGV – Sezione di Catania (2001), Multidisciplinary approach yields insight into Mt. Etna 2001 eruption, *EOS Transactions*, AGU 82:653–656.

Calvari S., M. Neri, and H. Pinkerton (2002), Effusion rate estimations during the 1999 summit eruption on Mount Etna, and growth of two distinct lava flow fields, *J. Volcanol. Geotherm. Res.*, 119, 107-123.

Cashman K. V., R. C. Kerr, and R. W. Griffiths (2006), A laboratory model of surface crust formation and disruption on lava flows through non-uniform channels, *Bulletin* of Volcanology, 68, 753-770.

Coltelli M., C. Proietti, S. Branca, M. Marsella, D. Andronico, L. and Lodato (2007), Analysis of the 2001 lava flow eruption of Mt. Etna from 3D mapping, accepted by J. Geoph. Res.

Corsaro R. A., L. Miraglia, and M. Pompilio (2006), Petrologic evidence of a complex plumbing system feeding the July-August 2001 eruption of Mt. Etna, Sicily, Italy, *Bulletin of Volcanology*, in press.

Costa A., and G. Macedonio (2005a), Computetional modeling of lava flows: A review, *Geological society of America Special Paper 396-14*, 207-216.

Costa A., and G. Macedonio (2005b), Numerical simulation of lava flows based on depth-averaged equations, *Geophysical Research Letters*, 32, doi:10.1029/2004GL021817.

Crisp J., and S. Baloga (1990), A model for lava flows with two thermal components, *J. Geophys. Res.*, 95, 1255–1270.

Crisci G.M., S. Di Gregorio, O. Pindaro, and G. Ranieri (1986), Lava flow simulation by a discrete cellular model: first implementation, Int. *J. Model. Simul.,* 6, 137-140.

Crisci G.M., S. Di Gregorio, R. Rongo, M. Scarpelli, W. Spataro, and S. Calvari (2003), Revisiting the 1669 Etnean eruptive crisis using a cellular automata model and implications for volcanic hazard in the Catania area, *J. Volcanol. Geotherm. Res.*, 123, 211-230.

Crisci G.M., R. Rongo, S. Di Gregorio, and W. Spataro (2004a), The simulation model SCIARA: the 1991 and 2001 lava flows at Mount Etna, *J. Volcanol. Geotherm. Res.*, 132, 253-267.

Curlander J. C., and R.N. McDonough (1991), *Synthetic Aperture Radar: Systems and Signal Processing,* 647 pp., Wiley, New York.

Damiani M. L., G. Groppelli, G. Norini, E. Bertino, A. Gigliato, and A. Cucita (2006), A lava flow simulation model for the development of volcanic hazard maps for Mount Etna (Italy), *Computer & Geosciences*, 32, 4, 512-526.

Del Negro C., L. Fortuna, A. Herault, and A. Vicari (2007), Simulations of the 2004 lava flow at Etna volcano by the MAGFLOW cellular automata model, *Bulletin of Volcanology*, in press.

Dobran F., and G. Macedonio (1992), Lava modeling contributions of the Volcanic Simulation Group during the 1991–1992 eruption of Mt. Etna*, Giardini, Pisa, Italy, Volcanic Simulation Group Report*, 92-7, Gruppo Nazionale per la Vulcanologia (GNV) Consiglio Nazionale delle Ricerche (CNR), p. 28.

Dragoni M., M. Bonafede, and E. Boschi (1986), Dowslope flow models of a Bingham Liquid: implications for lava flows, J. *Volcanol. Geotherm. Res.*, 30, 305-325.

Dragoni M., and A. Tallarico (1994), The effect of crystallization on the rheology and dynamics of lava flows, *J. Volcanol. Geotherm. Res.*, 59, 241–252.

Dragoni M. (1993), Modelling the rheology and cooling of lava flows, in *Active lavas: monitoring and modeling*, edited by C.R.J. Kilburn and G. Luongo, pp. 235-258, UCL Press, London.

Dragoni M., I. Borsari, and A.Tallarico (2005), A model for the shape of lava flow fronts, J. Geoph. Res., VOL. 110, doi:10.1029/2004JB003523.

Favalli M., M. Pareschi, A. Neri, and I. Isola (2005), Forecasting lava flow paths by a stochastic approach, *Geophysical Research Letters*, v. 32, L03305, doi: 10.1029/2004GL021718.

Felpeto A., V. Araña, R. Ortiz, M. Astiz, and A. García (2001), Assessment and Modelling of Lava Flow Hazard on Lanzarote (Canary Islands), *Natural Hazards*, 23, 247-257.

Fouler R. (2001), Topographic Lidar Chapter 7, In *Digital Elevation Model Technologies and Applications: the DEM Users Manual,* Edited by David F. Maune, pp. 207-236, American Society for photogrammetry and Remote Sensing, Bethesda, Maryland.

Franceschetti G. and R. Lanari (1999), *Synthetic Aperture Radar Processing*, 307 pp., CRC Press LLC Boca Raton, Florida.

Frazzetta G., and R. Romano (1984), The 1983 Etna eruption: event chronology and morphological evolution of the lava flow, *Bull. Volcanol.,* 47, 1079-1096.

Fujii T., and H. Imura (1972), Natural convection heat transfer from a plate with arbitrary inclination, *Int. J. Heat Mass Transfer,* 15, 755.

Giordano D., and D.B. Dingwell (2003 a), Viscosity of hydrous Etna basalt: implications for Plinian-style basaltic eruptions, *Bull. Volcanol.*, 65, 8-14.

Giordano D., and D.B. Dingwell (2003 b), Non-Arrhenian multicomponent melt viscosity: a model, *Earth and Plan. Sci. Lett.*, 208, 337-349.

Goto A., I. Maeda, Y. Nishida, and H. Oshima (1997), Viscosity equation for magmatic silicate melts over a wide temperature range, *Paper presented at Unzen International Workshop: Decade Volcano and Scientific Drilling, Univ. of Tokyo, Shimabara, Japan*.

Guest, J. E. (1982), Styles of eruption and flow morphology on Mount Etna, in *Mt. Etna Volcano: A Review of the Recent Earth Science Studies*, Mem Soc. Geol. Ital., 23, 49– 73.

Guest J.E., C.R.J. Kilburn, H. Pinkerton, and A.M. Duncan (1987), The evolution of lava flow field: observation of 1981 and 1983 eruptions of Mount Etna, Sicily, *Bull. Volcanol.,* 49, 527-540.

Harris A. J. L., S. Blake, D. A. Rothery, and N. F. Stevens (1997), A chronology of the 1991 to 1993 Mount Etna eruption using advanced very high resolution radiometer data: Implications for real-time thermal volcano monitoring, *J. Geoph. Res.*, 102, B4, 7985-8003.

Harris A. J. L., L. P. Flynn, L. Keszthelyi, P. J. Mouginis-Mark, S. K. Rowland, and J. A. Resing (1998), Calculation of lava effusion rates from Landsat TM data, *Bull. Volcanol.*, 60, 52–71.

Harris A.J.L., J.B. Murray, S.E. Aries, M.A. Davies, L.P. Flynn, M.J. Wooster, R. Wright, and D.A. Rothery (2000), Effusion rate trends at Etna and Krafla and their implications for eruptive mechanisms. *J. Volcanol. Geotherm. Res.*, 102, 237-270.

Harris A. J. L., and S. K. Rowland (2001), FLOWGO a kinematic thermo-rheological model for lava flowing in a channel, *Bull. Volcanol.,* 63, 20-44.

Harris A. J. L., and Neri M. (2002), Volumetric observation during paroxysmal eruptions at Mount Etna: pressurized drainage of a shallow chamber or pulsed supply?, *J. Volcanol. Geotherm. Res.*, 116, 79-95.

Hidaka M., A. Goto, S. Umino, and E. Fujita (2005), VTFS project: Development of the lava flow simulation code LavaSIM with a model for three-dimensional convection, spreading, and solidification", *Geochemistry Geophysics and Geosystems (G3)*, 6, 7, doi:10.1029/2004GC000869

Honda K., and M. Nagai (2002), Real-time volcano activity mapping using ground-based digital imagery, *ISPRS Journal of Photogrammetry and Remote Sensing*, 57, 159-168.

Hughes J. W., Duncan A. M., 1990, Changing styles of effusive eruption on Mount Etna since AD 1600, in *Magma Transport and Storage*, pp. 386-406, edited by M.P. Ryan, John Wiley & Sons Ltd.

Hulme G. (1974), The interpretation of lava flow morphology, *Geophys. J. R. Astron. Soc.,* 39, 361-383.

Hulme G. (1982), A review of lava flow processes related to the formation of lunar sinuous rilles, *Geophysical Surveys*, 5, 245-279.

Ishihara, K., M. Iguchi, and K. Kamo (1989), Numerical Simulation of Lava Flows on Some Volcanoes in Japan, in *Lava Flows and Domes, IAVCEI Proc. Volcanol., vol. 2*, edited by J. Fink, pp. 174–207, Springer, New York.

Kerr R. C., R. W. Griffiths, and K. V. Cashman (2006), Formation of channelized lava flows on an unconfined slope, *J. Geoph. Res.*, 111, doi: 10.1029/2005JB004225.

Kilburn C.R.J., and R.M.C. Lopes (1991), General Patterns of Flow Field Growth: Aa and Blocky Lavas*, J. Geophys. Res.*, 96 (12) 19721-19732.

Kilburn C.R.J. (1993), Aa lavas of Mount Etna, Sicily, in *Active lavas: monitoring and modeling*, edited by C.R.J. Kilburn and G. Luongo, pp. 73-101, UCL Press, London.

Kilburn C.R.J., and G.E. Guest (1993), Lava crusts, aa flow lengthening and the pahoehoe-aa transition, in *Active lavas: monitoring and modeling*, edited by C.R.J. Kilburn and G. Luongo, pp. 73-101, UCL Press, London.

Kilburn C.R.J., K. Pinkerton, and L. Wilson (1995), Forecasting the behaviour of lava flow, in *Monitoring Active Volcanoes*, edited by W.J. McGuire, C.R.J. Kilburn, J.B. Murray, pp. 346-368, UCL Press, London.

Kilburn C.R.J. (1996), Patterns and predictability in the emplacement of subaerial lava flows and flow fields, in *Monitoring and Mitigation of Volcano Hazards*, edited by R. Scarpa, R.I. Tilling, pp. 491-537, Springer, Berlin.

Kilburn C.R.J. (2004), Fracturing as a quantitative indicator of lava flow dynamics, *J. Volcanol. Geoth. Res.*, 132, 209-224.

Lee D.T. , and B.J. Schachter (1980), Two Algorithms for Constructing a Delaunay Triangulation, *Int. J. Computer Information Sci.,* 9 219 – 242.

Macedonio G., and A. Longo (1999), Lava Flow in a Channel with a Bifurcation, *Physics and Chemistry of the Earth*, 24, 11, 953-956.

McAdams W. H., 1954, *Heat transmission*, 3rd ed., McGraw-Hill, New York.

Miyamoto H., and S. Sasaki (1997), Simulating lava flows by an improved cellular automata method: *Computers & Geosciences*, 23, 3, 283–292, doi: 10.1016/S0098-3004(96)00089-1.

Mouginis-Mark P. J., and H. Garbeil (2005), Quality of TOPSAR topographic data for volcanology studies at Kilauea Volcano, Hawaii: An assessment using airborne lidar data, *Remote Sensing of Environment,* 96, 149-164.

Murase T., and A. R. McBirney (1970), Viscosities of lunar lavas, *Science*, 167, 1491-1493.

Murase T., and A. R. McBirney (1973), Properties of some common igneous rocks and their melts at high temperature, *Geol. Soc. Am. Bull.*, 84, 3563-3592.

Murray J.B. (1990), High-level magma transport at Mount Etna volcano, as deduced from ground deformation measurements, in *Magma Transport and Storage*, edited by M.P. Ryan, pp. 357 – 383, Wiley, London.

Patrick M. R., J. Dehn, and K. Dean (2004), Numerical modeling of lava flow cooling applied to the 1997 Okmok eruption: Approach and analysis, *J. Geoph. Res*., 109, doi:10.1029/2003JB002537.

Pinkerton H., and R. S. J. Sparks (1976), The sub-terminal lavas, Mount Etna: a case history of the formation of compound lava field, *J. Volcanol. Geoth. Res.*, 1, 167-182.

Pinkerton H., and R. S. J. Sparks (1978), Field measurements of the rheology of lava, *Nature*, 276, 383-384.

Pinkerton H., and R. J. Stivenson (1992), Methods of determining the rheological properties of magma at sub-liquidus temperatures, *J. Volcanol. Geoth. Res.*, 53, 47-66.

Pinkerton H. (1993), Measuring the properties of flowing lavas, in *Active lavas: monitoring and modelling*, UCL Press, London, Kilburn C.R.J., Luongo G, Ed., 175-191.

Proietti C., M. Hidaka, A. Goto, S. Umino, E. Fujita, M. Coltelli, and M. Marsella (2006), Simulation of a lava flow emitted during the 2001 Etna eruption by means of LavaSIM code, Poster presentato alla General Assembly EGU (European Geosciences Union), Vien 2 -7 April 2006.

Riccò A. (1902), Rilevamento topografico della lava dell'eruzione Etnea del 1892, *Boll. Accad. Gioenia Sci. Nat. Catania*, 75 , 5-8.

Ridley, H. M., P. M. Atkinson, P. Aplin, J.-P. Muller, and I. Dowman (1997), Evaluating the Potential of the Forthcoming Commercial U.S. High-Resolution Satellite Sensor Imagery at the Ordnance Survey, *Photogrammetric Engineering and Remote Sensing*, 63, 8, 997-1005.

Romano R., and C. Sturiale (1982), The historical eruptions of Mt. Etna, In: *Mount Etna Volcano, Mem. Soc. Geol. It.*, 23, 75-97.

Rowland S. K., and G. P. L. Walker (1990), Pahoehoe and a'a in Hawaii: volumetric flow rate controls the lava structure, *Bull. Volc.,* 52, 615-628.

Rowland S. K., M. E. MacKay, H. Garbeil, and P. J. Mouginis-Mark (1999), Topographic analyses of Kilauea Volcano, Hawai'i, from interferometric airborne radar, *Bull. Volc.,* 61, 1-14.

Rowland S. K., A. J. L. Harris, M. J. Wooster, F. Amelung, H. Garbeil, L. Wilson, P. J. Mouginis-Mark (2003), Volumetric characteristics of lava flows from interferometric radar and multispectral satellite data: the 1995 Fernandina and 1998 Cerro Azul eruptions in the western Galapagos, *Bull. Volc.,* 65, 311-330.

Scollo S., P. Del Carlo, and M. Coltelli (2006), Tephra fallout of the July-August 2001 Etna eruption: deposit features and analysis of plume dispersion, *J. Volcanol. Geoth. Res.*, in press.

Shaw H. R., T. L. Wright, D. L. Peck, and R. Okamura (1968), The viscosity of basaltic magma: an analysis of field measurements in Makaopuhi lava lake, Hawaii, *Am. J. Sci.*, 261, 255-264.

Shaw H. R. (1972), Viscosities of magmatic silicate liquids: An empirical method of prediction, *Am. J. Sci.*, 272, 870-893.

Spataro W., D. D'Ambrosio, R. Rongo, and G. A. Tronfio, (2004), An Evolutionary Approach for Modelling Lava Flows Through Cellular Automata, *Lecture Notes in Computer Science,* 3305, 725-743.

Stevens N. F., J.B. Murray, and G. Wadge (1997), The volume and shape of the 1991–1993 lava flow field at Mount Etna, Sicily, *Bull. Volcanol*, 58, 449–454.

Stevens N.F., G. Wadge, and J.B. Murray (1999), Lava flow volume and morphology from digitised contour maps: a case study at Mount Etna, Sicily, *Geomorphology*, 28, 251-261.

Taddeucci J., M. Pompilio, and P. Scarlato (2004), Conduit processes during the July–August 2001 explosive activity of Mt. Etna (Italy): inferences from glass chemistry and crystal size distribution of ash particles, *J. Volcanol. Geoth. Res.*, 137, 33-54.

Tallarico A., and M. Dragoni (2000), A three-dimensional Bingham modelfor channeled lava flows, J. Geophys. Res., 105(B11), 25969-25980.

Tilling R. I., and D. W. Peterson (1993), Field observation of active lava in Hawaii: some practical consideration, in *Active lavas: monitoring and modelling*, UCL Press, London, Kilburn C.R.J., Luongo G, Ed., 147-174.

Vicari A., A. Herault, C. Del Negro, M. Coltelli, M. Marsella, and C. Proietti (2006), Modeling of the 2001 lava flow at Etna Volcano by a Cellular Automata approach, *Environ. Model. Softw.,* doi:10.1016/j.envsoft.2006.10.005.

Vinassa de Regny P. (1911), L'eruzione Etnea del 1910, Parte quinta. Osservazioni geologiche e morfologiche, *Atti Acc*., 5, 4–11.

Wadge G. (1978), Effusion rate and the shape of aa lava flow-fields on Mount Etna, *Geology*, 6, 503-506.

Wadge G. (1981), The variation of magma discharge during basaltic eruptions, *J. Volcanol. Geoth. Res.*, 11, 139-168.

Wadge G., P. A. V. Young, and I. J. McKendrick (1994), Mapping lava flow hazards using computer simulation, *J. Geoph. Res*., 99, 489-504.

Walker G. P. L. (1971), Compound and simple lava flows and flood basalts, *Bull. Volcanol.,* 35, 579–590.

Walker G. P. L. (1973), Lengths of lava flows, *Philos. Trans. R. Soc. London*, Ser. A, 274, 107– 118.

Waltershausen W. S. (1880), *Der Etna. Vol. 1 and 2*, 317 pp., Engelman, Leipzig.

Acknowledgements

I'd like to thank my tutors Maria Marsella and Mauro Coltelli for guiding me during my PhD. work. Maria, for giving me the background about the topography, necessary for preparing my dataset, and especially for showing me a starting point when I didn't know how to proceed and I was lost in my pessimistic considerations, I really liked to work with her and her group. Mauro, for helping me to improve my background on lava flows and for his suggestions on the result interpretation. I'd like to thank also my supervisor Paolo Baldi.

I'm indebted with the researchers of the VTS (Volcanic Thermal Fluiddynamics Simulations) project Eisuke Fujita, Akio Goto, Masataka Hidaka and Susumu Umino, the utilization of the LavaSIM simulation code they developed made possible my work. I'm particularly grateful to Eisuke Fujita for his suggestions and the discussions on the results I obtained, to Masataka Hidaka for patiently clearing up all my doubts about the code and to Akio Goto, who gave me hospitality in his university during my study period in Japan. I'm very grateful to all of them for their kindness, they facilitated very much my living and showed me very beautiful places of their country.

I also have to thank the researcher of the TECNOLAB of INGV-CT, Ciro Del Negro, Annamaria Vicari and Alexis Herault, which developed the MAGFLOW code and allowed me to apply it as a part of my PhD. work.

A great thank you to my friends and colleagues Alberico Sonnessa and Ernesto Bernardo. I can't forget Elisa Bongiorno, and I'd also like to mention Ulisse Fabiani, Francesca Giannone, Roberto Monticelli, Massimiliano Colafranceschi, Witold Wolski and Nicoletta Teti.

Finally I must remember my family: if I'm writing this acknowledgements is also thanks to them.